Ministry of Higher Education and Scientific Research
University of Baghdad
Institute of Laser for Postgraduate Studies

SINGLE MODE-CORELESS-SINGLE MODE REFRACTIVE INDEX FIBER SENSOR BASED ON MACHZENDER INTERFEROMETRY

A Thesis Submitted to the Institute of Laser for Postgraduate Studies, University of Baghdad in Partial Fulfillment of the Requirements for the Degree of Master of Science in Laser / Electronic and Communication Engineering

By
Noor Adnan Hamza

B.Sc. Laser and optoelectronic Engineering – 2013

Supervisor
Asst. Prof. Dr. Hanan J. Taher

2020 AD **1441 AH**

الأهداء

يا من أحمل اسمك بكل فخر
يا من أفتقدك منذ الصغر
يا من يرتعش قلبي لذكرك
يا من أودعتني لله أهديك هذا البحث............ أبي (رحمه الله)

إلى ملاكي في الحياة ...

إلى معنى الحب و الحنان والتفاني ...

إلى بسمة الحياة وسر الوجود...
إلى من كان دعائها سر نجاحي وحنانها بلسم جراحي إلى أغلى الحبايب .... أمي الحبيبة

إلى الروح التي ترافقني بكل خطوة ...

إلى من علمني فلسفة الحياة ورحل عني ....أخي (رحمه الله)

إلى توأم روحي ورفيقة دربي .. إلى صاحبة القلب الطيب والنوايا الصادقة

إلى من رافقتني منذ أن حملنا حقائب صغيرة ومعك سرت الدرب خطوة بخطوة وما تزال ترافقني حتى الآن .... أختي

إلى أخي ورفيق دربي وهذه الحياة بدونك لاشيء معك أكون أنا وبدونك أكون مثل أي شيء .. في نهاية مشواري أريد أن أشكر على مواقفك النبيلة إلى من تطلعت لنجاحي بنظرات الأمل .... أخي

إلى الشموع التي ذابت في كبرياء........
لتنير كل خطوة في دربنا........
لتذلل كل عائق أمامنا.......
فكانوا رسلاً للعلم والأخلاق.......
شكراً لكم جميعاً...... (أساتذتي الأعزاء وأصدقائي وزملائي)

بِسْمِ اللَّهِ الرَّحْمَنِ الرَّحِيمِ

اللَّهُ لَا إِلَهَ إِلَّا هُوَ الْحَيُّ الْقَيُّومُ لَا تَأْخُذُهُ
سِنَةٌ وَلَا نَوْمٌ لَهُ مَا فِي السَّمَوَاتِ وَمَا فِي
الْأَرْضِ مَنْ ذَا الَّذِي يَشْفَعُ عِنْدَهُ
إِلَّا بِإِذْنِهِ يَعْلَمُ مَا بَيْنَ أَيْدِيهِمْ وَمَا خَلْفَهُمْ
وَلَا يُحِيطُونَ بِشَيْءٍ مِنْ عِلْمِهِ إِلَّا بِمَا شَاءَ
وَسِعَ كُرْسِيُّهُ السَّمَوَاتِ وَالْأَرْضَ وَلَا
يَئُودُهُ حِفْظُهُمَا وَهُوَ الْعَلِيُّ الْعَظِيمُ

ACKNOWLEDGEMENT

First of all First, I would like to thank God for the gift of knowledge and for giving me strength, patience and wisdom to complete this thesis.

I would first like to thank my thesis supervisor Dr. Hanan.J.Taher. The door to her office was always open whenever I ran into a trouble spot or had a question about my research or writing. She steered me in the right the direction whenever he thought I needed it.

I would also like to thank the experts who were involved in this thesis: [prof. Hussein A. Jawad, Dr. Mohammed. K. Dhahir and Dr. Zainab Fadil who contributed. Without their passionate participation and input, this thesis could not have been successfully conducted.

I would like to acknowledge the great help he provided during the research, Eng. Saif. A. Mohammed and I am gratefully indebted to his for his very valuable comments on this thesis.

Finally, I must express my very profound gratitude to my family, friends and for lab colleagues (especially Dr.Ali, MS.c Ansam, Hussein and Hiba) for providing me with unfailing support and continuous encouragement throughout the process of researching and writing this thesis. This accomplishment would not have been possible without them.

Thank you.

ABSTRACT

All-optical fiber based-sensors, due to their intrinsic characteristic of simple, compact size, cost-effective, resistance to electromagnetic interference, good hostility to corrosion, durability, flexibility, accuracy and so on.

A high sensitivity refractive index (RI) sensor depends on the theory of multimode interference (MMI) has been fabricated and investigated. This effect was experimentally demonstrated. The performance of the RI sensor with different coreless fiber diameters (CF) was examined to acquire an appropriate dimension of extreme evanescent fields. This fabrication of the sensor has been done by reducing the coreless fiber (CF) with etching process for measuring the refractive index of Sodium Chloride solution and different fluids. The working principle of this RI sensor depends on the multimode interference (MMI) theory. In this work, the RI sensing structure comprises of single-mode fiber-coreless fiber-single mode fiber (SCS) configuration and the encirclement refractive index behaves as the cladding of the CF. RI sensor was studied for three different lengths with 20, 25 and 30 mm of CF which is represented the sensing area. Since the CF diameter is an essential factor in SCS fiber configuration to attain extreme sensitivity, the effect of CF diameter on the RI sensing sensitivity was investigated. Accordingly, various diameters of CF of 100, 75 and 50 μm were achieved for each length. The CF diameter was chemically etched using 40% hydrofluoric (HF) acid immersion. The construction method of SCS fiber configuration began with stripped-off the

acrylate coating from CF and SMF, then the CF fusion spliced from both ends with SMF. Then, the fabricated SCS construction was set in a V-shaped groove. This groove was utilized to include the etching liquid acid (HF 40%). The 100, 75 and 50 µm CF diameter was realized by controlling the etching time. The etching method was retained in CF section, and the splicing region was tested under the microscope in every etching process to make sure that this area did not effected by HF.

The experimental results of the SCS configuration encompassed of the etched CF at 50 µm diameter with a CF length of 25 mm exhibited a maximum wavelength shift is about 50.6 and the greatest sensitivity is about 1012 nm/RIU for NaCl solution when the concentration is 25%. While for the refractive index of 1.352, a maximum wavelength shift is 56 and the greatest sensitivity is 1058 nm/RIU for fluids. The length and diameter of CF would influence the output spectra and there is an optimum length for every diameter to preserve the self-imaging and reduction of the losses. The linear fitting coefficient (R^2) is 0.998 for SCS fiber configuration with 50 µm diameter and 25 mm length, which exhibits an excellent RI sensing features of the SCS-based sensor.

LIST OF CONTENTS

Chapter one

Introduction and basic concept

Chapter two

Experimental setup and Procedures

Chapter three

Results and discussion

LIST OF TABLES

LIST OF FIGURES

LIST OF SYMBOLS AND ABBREVIATONS

SMF	Single Mode Fiber
MMF	Multimode Fiber
PCF	Photonic Crystal Fiber
CF	Coreless fiber
RI	Refractive index
SCS	Single-mode fiber-coreless fiber-single mode fiber
MMI	Multimode Interference
n_1	Core refractive index
n_2	Cladding refractive index
V	Normalized frequency
K_o	The wavenumber
λ	The operated wavelength
Δ	Fractional index difference
M	The total mode number
b	The normalized propagation constant

β	Propagation constant
D	Core diameter of PCF
Λ	Pitch of PCF
d	Size of hole in PCF
TIR	Total Internal Reflection
φ	Angle of incidence
φ_c	The critical angle
θ_a	The acceptance angle
FPI	Fabry-Perot interferometer
FBGs	fiber Bragg gratings
R_1	First reflecting component
R_2	Second reflecting component
SIs	Sagnac Interferometers
MZIs	Mach-Zehnder Interferometers
OPD	Optical path difference
LPGs	Long period fiber gratings
MIs	Michelson interferometers
BBS	broadband Source
LM	Laser Mount
LDC	Laser Diode Controller
TED	Temperature controller
MFD	Mode Field Diameter
OSA	Optical Spectrum Analyzer
HF	hydrofluoric acid
mm	Millimeter
µm	Micrometer
NaCl	Sodium Chloride
SS	Single mode fiber structure
RIU	Refractive index unit
R^2	The linear fitting coefficient

Chapter One

Introduction and Basic Concept

1.1 Introduction:

Recently, there is more interest in the optical fiber sensors due to their potential in several applications such as biomedical, chemical, biological, environmental, military and medical applications [1-6]. These sensors that have been designed and developed making a lot of attention for measuring many parameters such as temperature, magnetic fields, humidity, acceleration, pressure, vibration, strain and refractive index [7]. Optical fiber for sensing devices offers many advantages such as, small size, immunity to electromagnetic, flexibility, accuracy, good corrosion resistance, durability, capability for remote operation and high sensitivity [8]. The sensors may have different structures that have been fabricated using many types of optical fiber such as: single mode fiber (SMF), multimode fiber (MMF), photonic crystal fiber (PCF), Brag Grating fiber (BGF) and coreless fiber (CF).

The refractive index sensors is the basis of the most of optical fiber sensing applications, such as biomolecule detection, medical diagnostics and chemical concentration sensing [9].

The major way to measure the sensitivity of the surrounding RI, is by using the coreless fiber (CF). The proposed refractive index (RI) sensing structure consists of SMF-CF-SMF (SCS) structure and the surrounding refractive index acts as the cladding of the coreless fiber (CF).

The SCS structure of the optical fiber sensor depends on the principle of the multimode interference (MMI) which occurs when the core mode of the lead in single mode fiber section, a number of high-order modes are excited and propagated along the coreless fiber, at the second splicing point, the high-order modes are coupled and back to the core fiber of the lead out single mode fiber.

The effective sensing section is presented by the coreless fiber (CF) with different lengths surrounded by a solution with variable concentrations (variable refractive index), where the sensing section spliced between two single mode fibers (SMF).

1.2 Optical Fibers

A thin flexible and transparent wire prepared for light propagation, its structure made of glass or silica. An optical fiber consists of three parts: the buffer coating, the cladding and the core as shown in figure 1.1 where the core represent the heart of the optical fiber while the cladding is the outer and surrounding by a layer of protective materials such as acrylate polymer or polyimide. The refractive index of the core (n_c) always is higher than the refractive index of the cladding (n_{cl}), this difference in refractive indices gives the light the ability to be guided and the phenomena of total internal reflection will appear [10]. The optical fiber can be used for many medical, communication and industrial applications for its advantages of low cost, small size, wide bandwidth, flexibility, minimum attenuation losses and secure to transfer different signals [11].

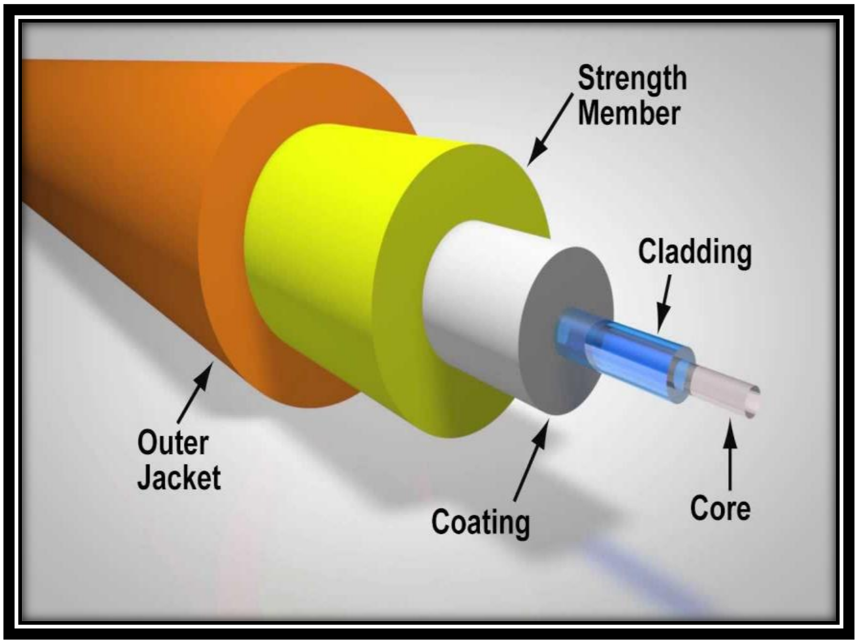

Figure (1.1): optical fiber structure [12].

1.3 Optical fiber types

There are different types of optical fiber that depends on the structure or the waveguide mode of the fiber such as:

1.3.1 Single Mode Optical Fiber (SMF)

The small diameter of SMF (a) about (8-10) µm allows one mode of light to transmit through it with a clad diameter (d) of about 125 µm.

This type of fiber consists of doped silica core with refractive index (n_1) and fused silica cladding with refractive index (n_2) where the n_1 is slightly higher than n_2 [13]. The normalized frequency or the V number plays an important rule on the cut-off condition as the equation: [14]

$$\mathbf{V= k_0a\,(n_1^2-n_2^2)^{1/2}= 2\pi/\,\lambda\; an_1\,(2\Delta)^{1/2} \ldots\ldots\ldots\ldots\ldots\ldots\; (1.1)}$$

Where k_0: the wavenumber and can be expressed as:

$$\mathbf{k_0 = 2\pi/\,\lambda \ldots\ldots\ldots\ldots\ldots\ldots\ldots\ldots\ldots\ldots\ldots\ldots\ldots\; (1.2)}$$

λ: is the operated wavelength,

Δ: fractional index difference and can be showed as:

$$\mathbf{\Delta= n_1\text{-}n_2/\,n_1 \ldots\ldots\ldots\ldots\ldots\ldots\ldots\ldots\ldots\ldots\ldots\ldots\ldots\; (1.3)}$$

For single mode operation the V number should be V< 2.405

For the total mode number (M) can be calculates as the followed equation:

$$\mathbf{M= V^2/2 \ldots\ldots\ldots\ldots\ldots\ldots\ldots\ldots\ldots\ldots\ldots\ldots\ldots\; (1.4)}$$

We can define the normalized propagation constant (b) as:

$$\mathbf{b= [(\beta/k_0)^2\text{-}\; n_2^2] \,/\, [n_1^2\text{-}n_2^2] = [\bar{n}\text{-}\; n_2^2] \,/\, [n_1^2\text{-}n_2^2] \ldots\ldots\ldots\; (1.5)}$$

Where β propagation constant, and $\bar{n}$: mode index

1.3.2 Multimode Optical Fiber (MMF)

The larger core diameter of (50-60) µm allows many modes of light to transmit through it with a clad diameter of 125 µm and the difference between the single mode fiber and the multimode fiber can be shown in figure (1.2) [15].

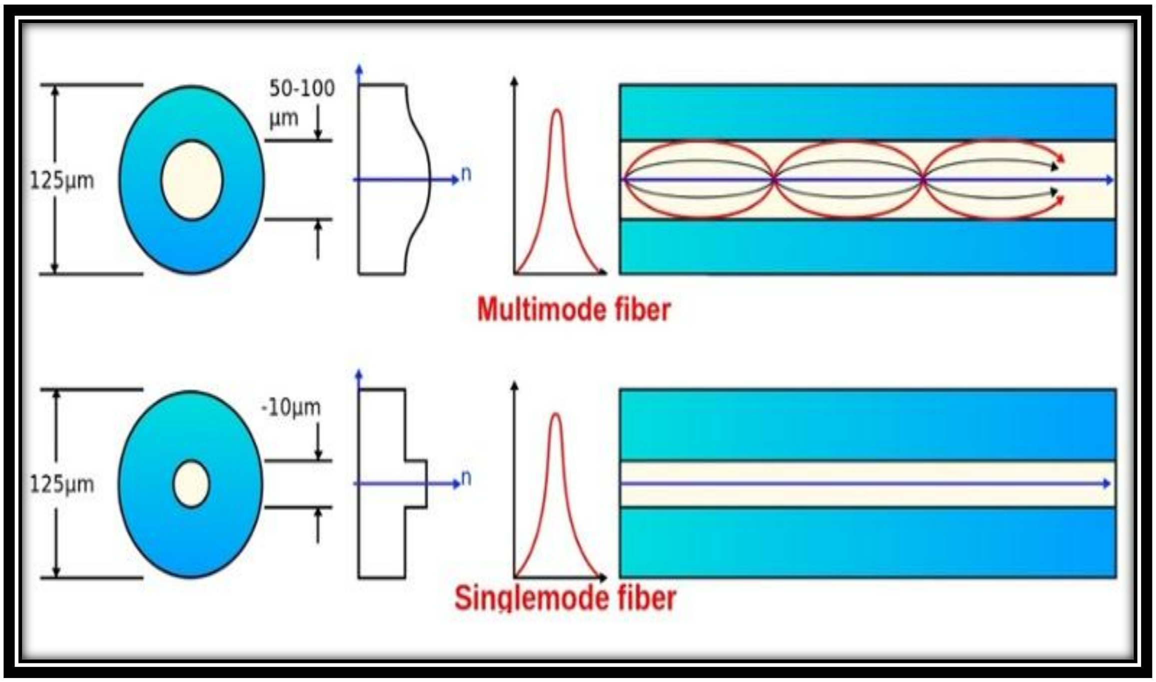

Figure 1.2: Single mode fiber vs. Multimode fiber [16].

The MMF can be classified based on the refractive index:

1.3.2.1 Step- Index Multimode Fiber

It has core with a refractive index higher in one step than the cladding refractive index and the light is transmitted in a single path. The light rays propagate through it in the shape of meridiognal rays which cross the fiber axis during every reflection at the core cladding boundary [17].

1.3.2.2 Graded- Index Multimode Fiber

This type of optical fiber core has a non-uniform refractive index that gradually decrease from the Centre towards the core cladding interface but with a uniform cladding refractive index. The light rays propagate through it in the form of skew rays or helical rays. They do not pass through the fiber axis at any time [18].

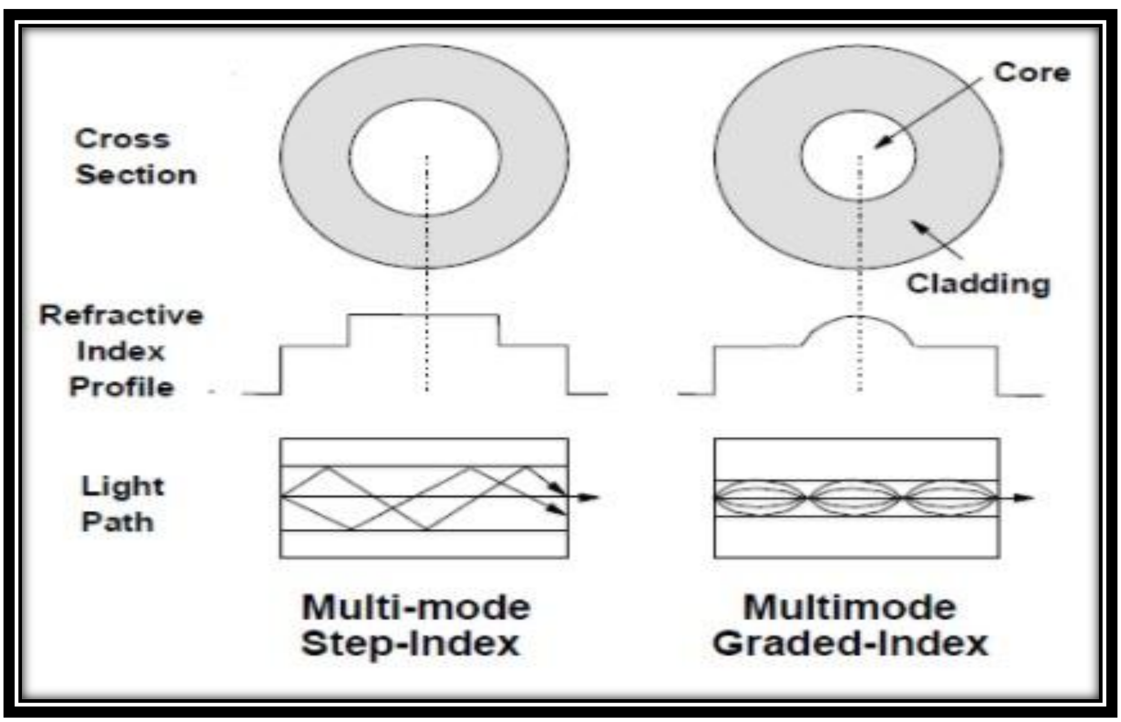

Figure 1.3: The multimode step-index fiber and the multimode graded-index fiber [19].

1.3.3 Photonic Crystal Fiber (PCF)

This type of fibers have a specific arrangement of air holes that run throughout the fiber length. Different materials are used such as silica, Teflon, PMMA, tellurite and topas for improving the performance of the PCF structures. The parameters of the photonic crystal structure are:

1. Core diameter (D): It is the diameter of the central solid part of the fiber.

2. Pitch (Λ): The distance between the centers of the air holes in the fiber.

3. Size of hole (d): It is the diameter of the air hole.

There are two guidance mechanisms depending on the PCF geometry. It includes (1) Index guided fiber or holey fiber, (2) Photonic band gap fiber. Index-guided fiber consists of the solid core where light is guided by the modified total internal reflection whereas photonic band gap fiber has a hollow core and follows photonic band gap mechanism [20].

1.3.3.1 Index-Guided Fiber

Index-guided fiber is also called holey fiber. It consists of a solid core and the pattern of holes surrounding that core. Here, the effective refractive index of the cladding is lower than the core due to the presence of holes in it. The light travels through the fiber by the mechanism of modified total internal reflection. Figure (1.4) shows the index-guided fiber. [21]

1.3.3.2 Photonic Band gap Fiber

It consists of the hollow core. In this type, the center air hole has a larger diameter as compared to the diameter of the surrounding hole. Due to this, the core refractive index becomes lower than the cladding and the principle of conventional fibers do not apply to these fibers.

Depending on the fiber geometry, the bandgap can be shifted to cover the entire optical domain. Figure (1.5), shows photonic band gap fiber or hollow fiber [22].

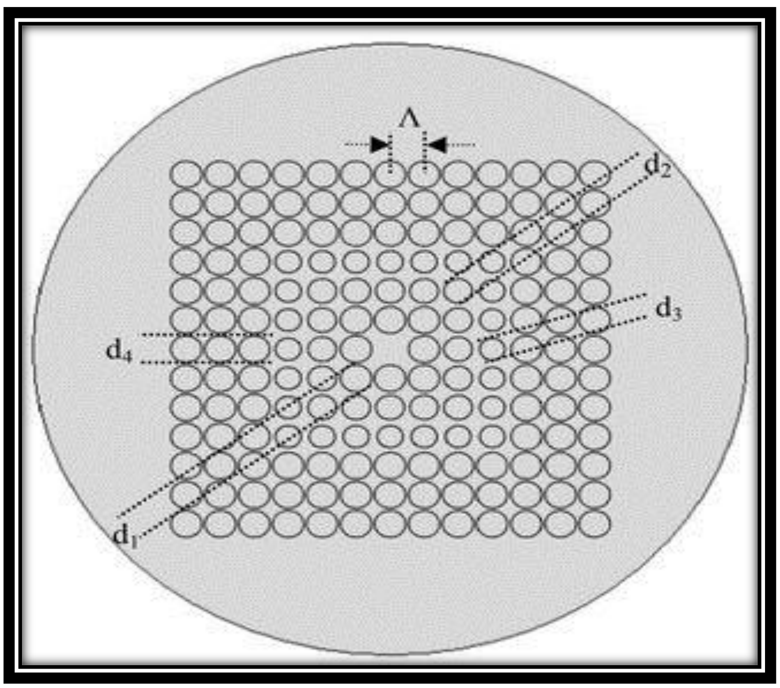

Figure 1.4: Index-guided photonic crystal fiber [23].

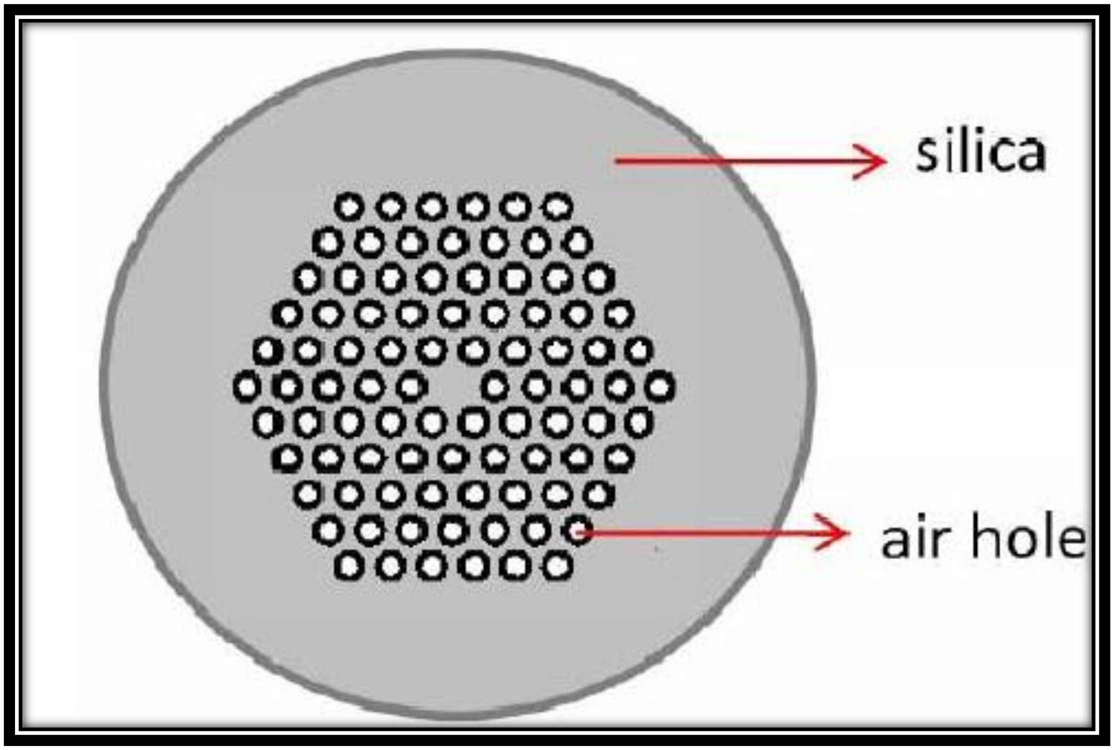

Figure 1.5: photonic band gap fiber or hollow fiber [24].

1.3.4 Coreless fiber (CF)

The coreless fiber is a new type of special fiber and has a uniform refractive index. It consists of a pure silica glass rod and an acrylate coating. The regular fiber have an inner core surrounding by cladding while the coreless fiber simply have a cladding only with a diameter of 125 µm as seen in figure (1.6).

This type has been fabricated with a different operation temperature (-65 _+300C˚) and a wide wavelengths operation range (400-2400) µm that can be useful for many applications [25].

Coreless fiber is considered as a special case of multimode fiber which outer diameter allows to multimode to be guided through it when the surrounding medium has lower refractive index than coreless fiber refractive index and

The absence of a waveguide makes this coreless fiber beneficial for reducing back reflections or to prohibit damage to the fiber end face in high-power applications [25].

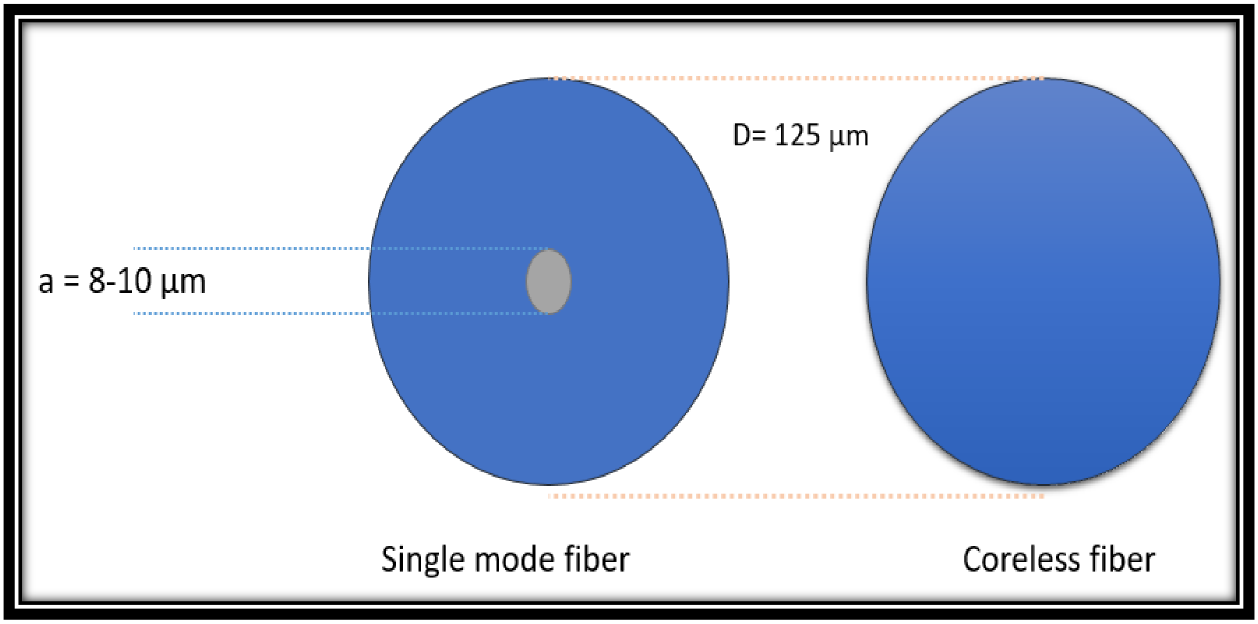

Figure (1.6): The compression between the single mode fiber and the coreless fiber.

1.4 Theory of Ray Transmission

1.4.1 Total Internal Reflection TIR:

The value of light that transmitted through a medium as radiation in certain velocity depends on the type of that medium where the transmission occurs.

In optical fiber the light will transmit as a ray and totally reflected according to the total internal reflection phenomena. The ratio of the velocity of light in space to a velocity of light in certain medium is called the refractive index which effects in how the light reflects when goes through a medium [26].

When the light incident at larger angle than the critical angle, the light will reflected back with high efficiency of 99%. The total internal reflection will occur when the light ray travels from a medium with refractive index lower (air) to a medium with higher refractive index (glass) and the incident angle exceeded the critical value. Figure (1.7) shows the transmission of light ray through a series of TIR at the interface of silica core and a little lower refractive index silica cladding. The ray has an angle of incidence φ at the interface who is greater than the critical angle and is reflected at the same angle to the normal axis [26].

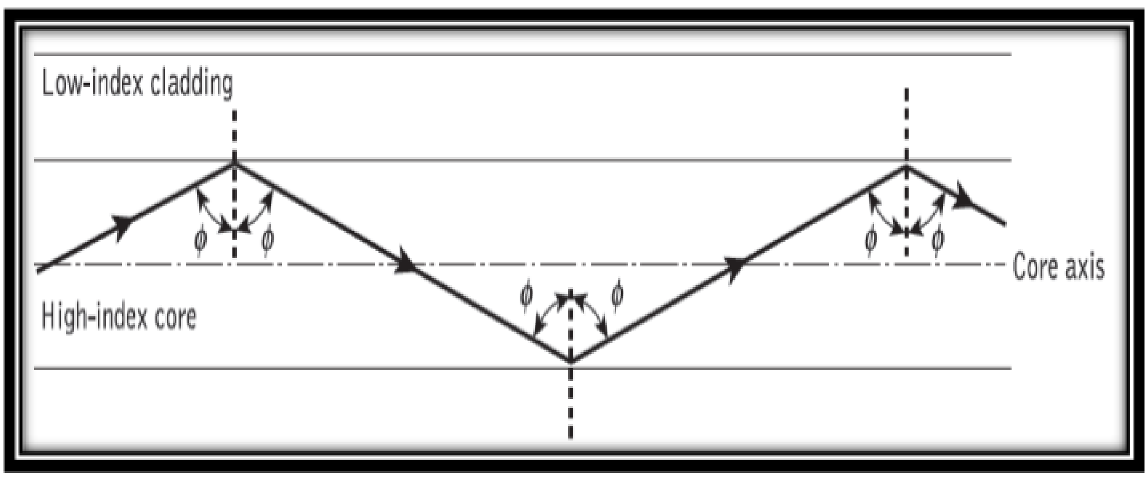

Figure 1.8: The transmission of light ray inside the optical fiber.

1.4.2 The Acceptance Angle

Considering the propagation of light in an optical fiber by TIR at the cladding and core interface it is valuable to magnify upon the geometric optics approach with reference to light rays entering the fiber. Since only rays by a sufficiently shallow grazing angle (for example: with an angle to the normal greater than φc) at the core- cladding interface are transmitted by TIR, it is obvious that not all rays entering the core of optical-fiber will keep to be propagated down [27]. The geometry heedful by launching a light ray into an optical fiber viewed in Figure (1.8), which clarifies a meridional ray (A) at the critical angle (φ_c) within the optical fiber at the cladding and core interface. It could be spotted that this ray enters the core of optical fiber at an angle (θ_a) to the optical fiber axis and is refracted at the air-core interface before transmission to the core-cladding boundary at the critical angle [30]. Thus, any rays which are incident into the core of optical fiber at an angle greater than (θa) will be transmitted to the core-cladding boundary at an angle minimal than (φc), and will not be totally internally reflected. This state is also seen in Figure 9, where the incident ray B at an angle greater than (θa) is refracted into the cladding and ultimately lost through radiation [28].

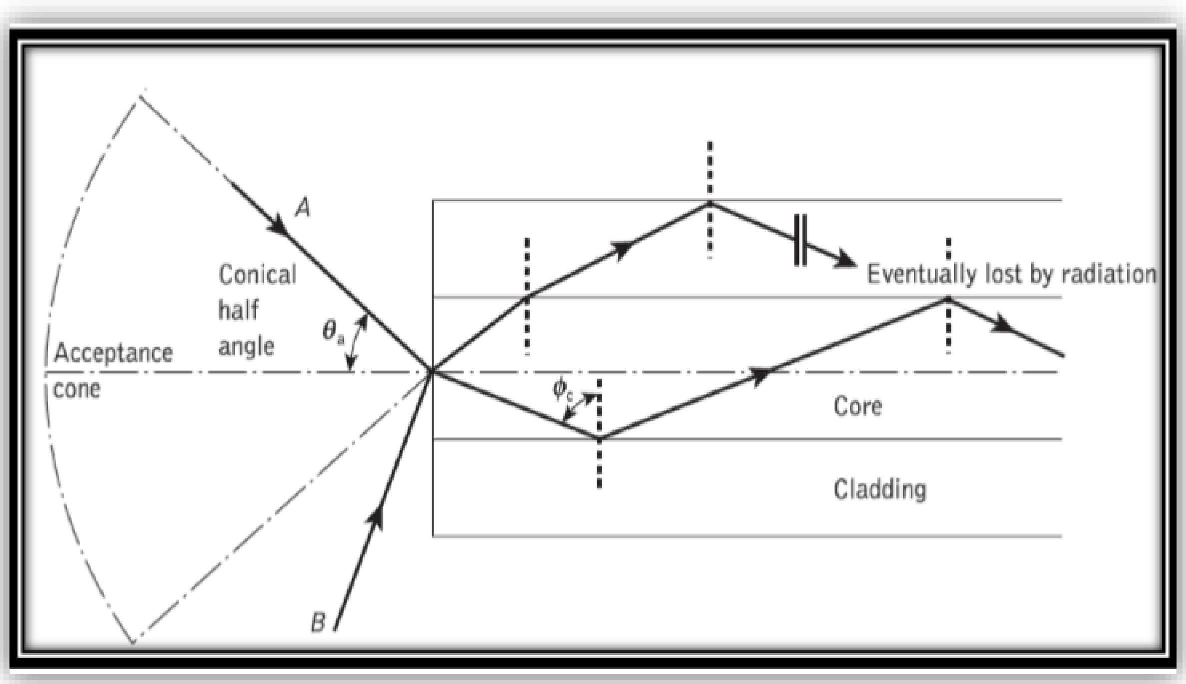

Figure 1.8: The acceptance angle θa when launching light into an optical fiber [29].

Therefore for the rays that had been transmitted by TIR within the core of optical fiber they necessity be incident on the core of optical fiber within an acceptance cone well-clarified by the conical half angle θa [30]. Thus θa is the greatest angle to the axis at which light may enter the optical fiber in order to be propagated, and is frequently pointed to as the acceptance angle for the optical fiber. If the fiber has a steady cross section (like. the core-cladding interfaces are parallel and there are no cutouts) an incident meridional ray at angle bigger than the critical angle will keep going to be reflected and will be transmitted through the fiber. From uniformity considerations it would be observed that the output angle to the axis will be equivalent to the input angle for the ray light, assuming the ray come out into a medium of the same refractive index from which it was input [31].

1.5 Multimode Interference

The structure of the optical fiber sensor is depends on the principle of the multimode interference (MMI) which occurs when the core mode of the light lead in single mode fiber section, a number of high-order modes are excited and propagated along the coreless fiber, at the second splicing point, the high-order modes are coupled and back to the core fiber of the lead out single mode fiber [32]. In general, these high order modes construct a complexes field distribution according to multimode interferences (MMI) effect. And so on, reproducible bright images or what is called self-imaging of the input field may be formed at specific locations where the excited modes are in phase [33].

The main parameters that influence in the design of such sensor are the length and the diameter parameters. According to MMI theory, the CF length can be calculated by the equation [34- 38]:

$$\mathbf{L_{CF} = P\,(3L_{\pi}/4) \qquad where\ P = 0, 1, 2} \ \ldots\ldots\ldots\ldots \ \mathbf{(1.6)}$$

Where the parameter p refers to the constructive interference number (self-imaging number). Such constructive interference can appear at periodic intervals known by p (p =0, 1, 2 …), at these lengths the formed images clarify a profile of a tight width and a high amplitude, and L_{π} is the beat length and can be expressed as:

$$\mathbf{L_{\pi} = (4n_{CF}D^{2}_{CF}) / (3\lambda_{o})} \ \ldots\ldots\ldots\ldots \ \mathbf{(1.7)}$$

Thus, the peak spectral response of this CF caused by self-imaging effect can be expressed as:

$$\mathbf{\lambda_{o} = P\,(n_{CF}\,D^{2}_{CF} / L_{CF})} \ \ldots\ldots\ldots\ldots \ \mathbf{(1.8)}$$

Here n_{CF} and D_{CF} correspond to the effective refractive index (RI) and the diameter of CF section, respectively. Then MMI will be increases by using the tapering and/or etching CF outer diameter and thus incensement in MMI due to varying in peak spectral response and sensitivity of the CF-MZI [39].

1.6 Evanescent Wave

The evanescent waves are created when the waves traveling in a medium endure total internal reflection (TIR) at its boundary because they hit it at an angle greater than the critical angle [40]. The physical illustration for the presence of the evanescent wave is that the electric and magnetic fields (or pressure gradients, in the state of acoustical waves) cannot be discontinuous at a boundary, as would be the status if there was no evanescent wave field. In optical fiber case, an evanescent wave is created whenever light undergoes TIR at the core cladding interface. The evanescent wave penetrating a small distance into the cladding of optical fiber [41].

Figure (1.9) is shown the evanescent wave which decays exponentially from the interface of core and clad and travelling parallel to it.

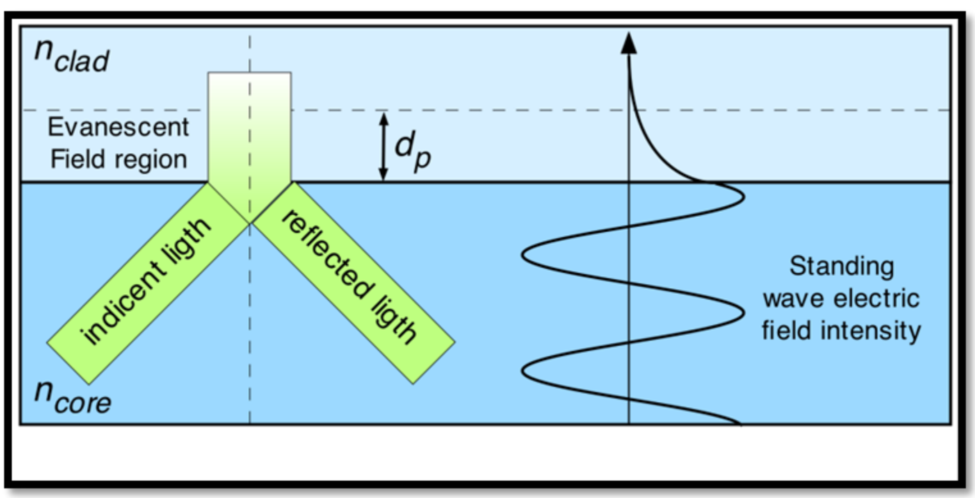

Figure 1.9: The evanescent wave in optical fiber [42].

1.7 Optical Fiber Sensors

The optical fiber sensors have significant advantages over other types of sensors and used in wider applications such as the physical properties measurements [refractive index, strain and humidity], Electric current measurement, distributed temperature monitoring, spatial displacement measurement and the application to the gas industry and oil, pressure sensing, temperature sensing [43].

The optical fiber sensors are categorized depending on the sensing location, the operating principle and their application.

1.7.1 Based on the sensing location:

On this foundation the fiber optic sensor labeled as intrinsic or extrinsic sensor. Figure (1.10) shows the extrinsic and intrinsic sensors.

1.7.1.1 Extrinsic Fiber Optic Sensor

The optical fiber simply uses to carry light from and to the outer optical device where the sensing takes place. In this issue the fiber is just the part that carries light.

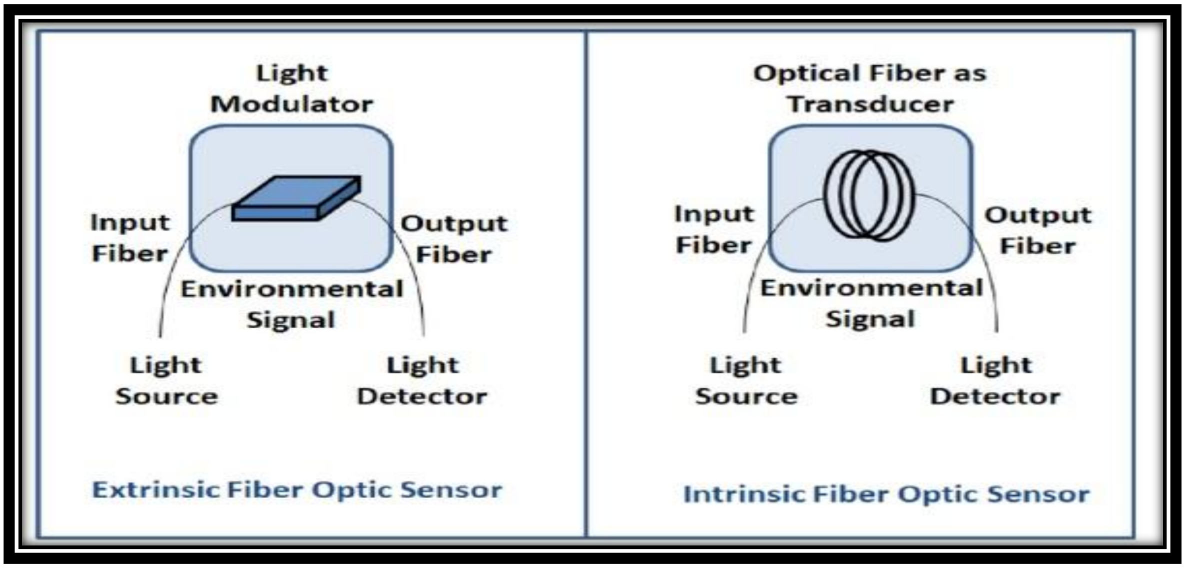

Figure 1.10: the extrinsic and intrinsic sensors [44].

1.7.1.2 Intrinsic Fiber Optic sensor

The physical parameter changes some characteristic of the propagating light beam that is sensed, here the optical fiber itself works as transducer, only a simple source and a detector is used [46]. Table 1.11 shows a Comparison of Extrinsic and Intrinsic optical sensors.

Table 1.11: comparison of Extrinsic and Intrinsic sensors [45].

Extrinsic	Intrinsic
• Applications- temperature, pressure, liquid level and flow. • Less sensitive • Easily multiplexed • Ingress/ egress connection problems • Easier to use • Less expensive	• Applications- rotation, acceleration, • strain, acoustic pressure and vibration. • More sensitive • Tougher to multiplex • Reduces connection problems • More elaborate signal demodulation • More expensive

1.7.2 Based on the intensity:

This sensor senses the variation of the light intensity that transmitted through the fiber by using a detector that placed at the end of the fiber. The evanescent wave sensor can be considered one of the intensity based sensor which uses evanescent field created whenever light transmitted between two dielectric media and total internal reflection occurs [46].

This type of sensor is used in chemical sensors that useful in measuring the chemical concentrations. The sensing process is accomplished by stripping the cladding from a piece of the optical fiber and a light source has been used that having a wavelength that can be absorbed by the chemical that is to be detected as shown in figure (1.12) [47].

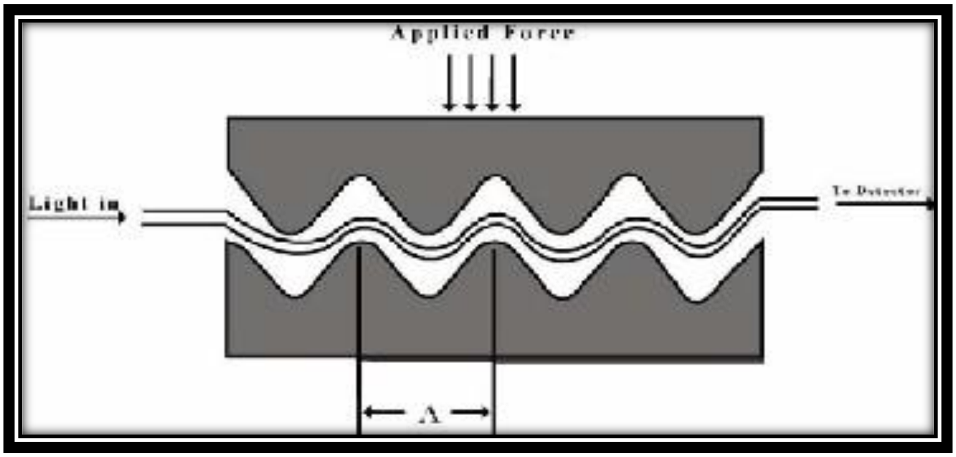

Figure 1.12: Fiber optic sensor based on intensity modulated (Micro bending sensor) [48].

1.7.3 Based on the wavelength:

Wavelength modulated fiber optic sensors use the changes in the wavelength of light for detection. Fluorescence sensors, the Bragg grating sensor and black body sensors are examples of wavelength-modulated sensors as shown in figure (1.13, 1.14) [49].

The fiber Bragg grating sensor is the most used sensor in different applications. This sensor is created by constructing frequent changes in index of refraction in the core of a single mode optical fiber which caused by strain, temperature of polarization changes, will result in a Bragg grating shift [50].

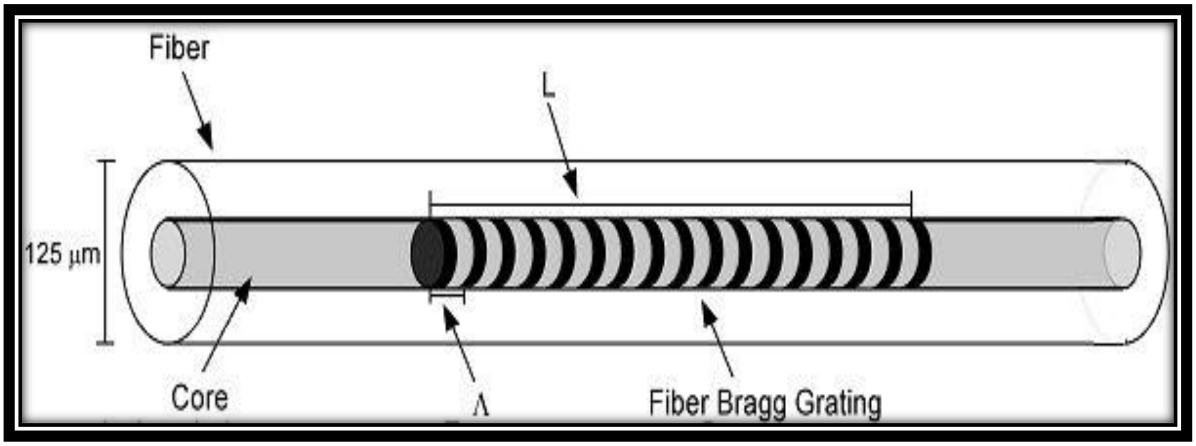

Figure 1.13: Fiber Bragg Grating sensor [51].

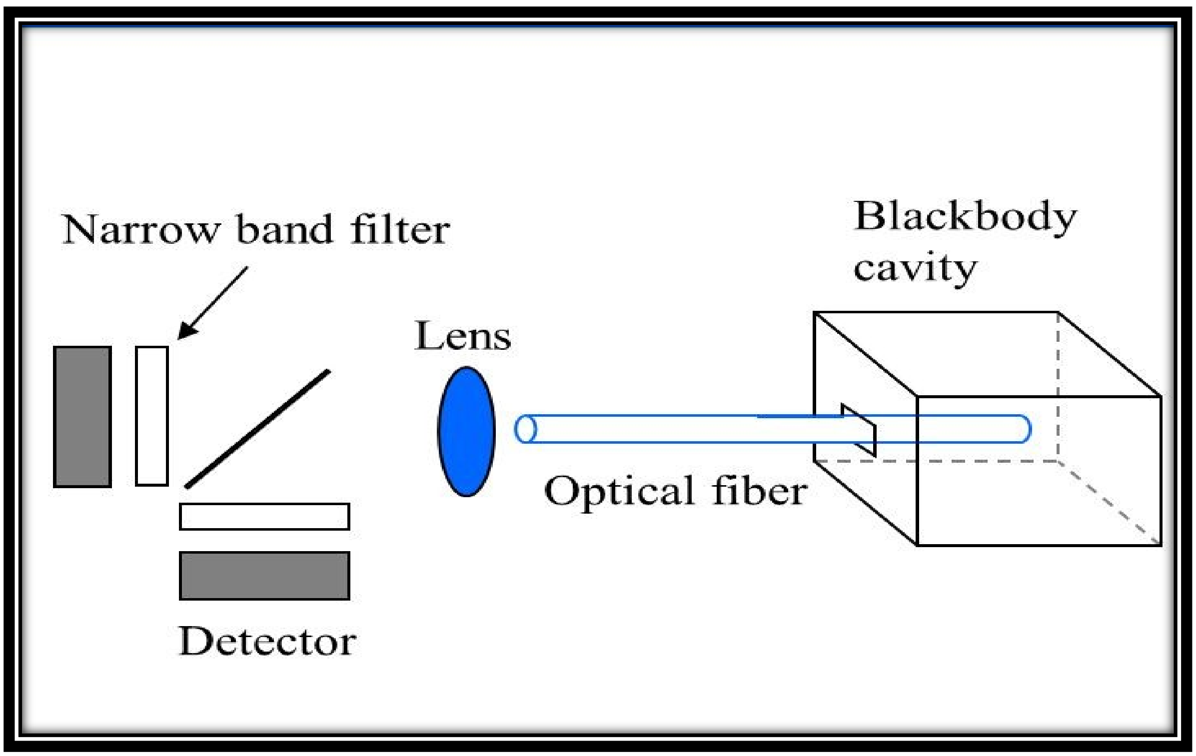

Figure (1.14): Black Body sensor [52].

1.7.4 Based on the Phase

The Phase modulated sensors utilize changes in the phase of light for detection. The optical phase of the light crossing through the fiber is modulated by the field to be detected [53]. This phase modulation is thereafter detected interferometerically, by matching the phase of the light in the signal fiber to that in a reference fiber. In an interferometer, the light is divide into two beams, where the first beam is exposed to the sensing environment and undergoes a phase shift and the other beam is isolated from the sensing environment and is applied for as a reference. Then the two beams will interfere with each other after they recombined [53].

The most ordinarily used interferometers are Mach-Zehnder, Michelson, Fabry-Perot and grating interferometers.

1.8 Interferometer types

1.8.1 Fabry- Perot interferometer (FPI)

The Fabry-Perot interferometer (FPI) is normally consist of two parallel reflecting surfaces splitted by a specific distance [54].

In optical fiber case the interference occurs between two parallel reflectors surfaces and in FPI these surfaces be either inside or outside the fiber [56]. The extrinsic and the intrinsic FPI sensors are the two main categories of the FPI sensor [55], where the extrinsic FPI cavity is formed outside the fiber. A supporting structure with a high reflecting mirrors formed the air cavity as shown in figure (1.15 a) and this structure is very useful for obtaining a high finesse interference signal.

In other hand, the intrinsic FPI sensors have the reflecting mirrors along the fiber as shown in fig (1.15 b) and this cavity can be formed in many methods such as fiber Bragg gratings (FBGs), micro machining, thin film deposition and chemical etching [56-58].

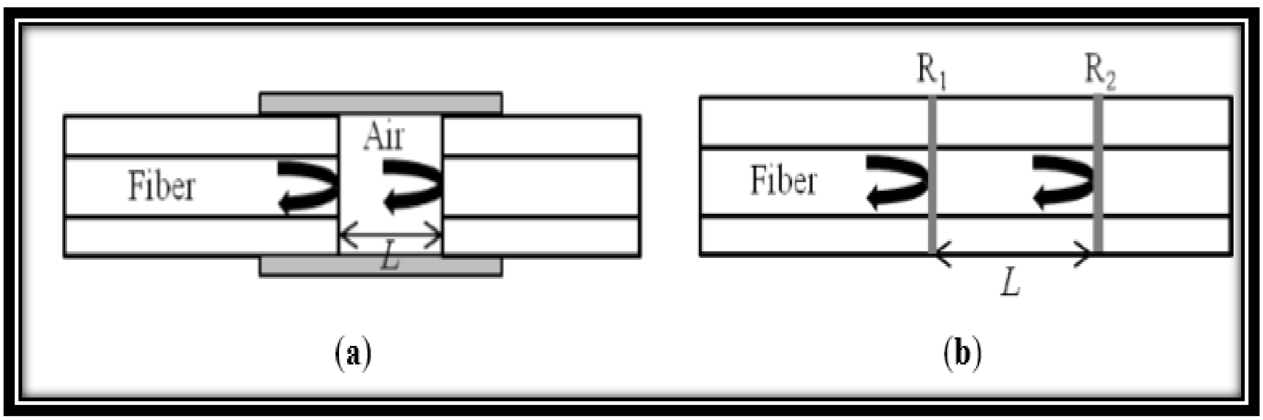

Figure1.15: (a) Extrinsic FPI sensor made by forming an external air cavity, and (b) intrinsic FPI sensor formed by two reflecting components, R1 and R2, along a fiber [55].

1.8.2 Sagnac Interferometers (SIs)

The Sagnac interferometers (SIs) getting a great attention in sensing applications. It’s structure consist of an optical fiber loop where a two beams along the fiber propagates in opposite directions with different polarization conditions. As clarified in figure (1.16), a 3-dB coupler used to split the light beam into two directions and the two counter-propagating beams are combined again at the same coupler [59].

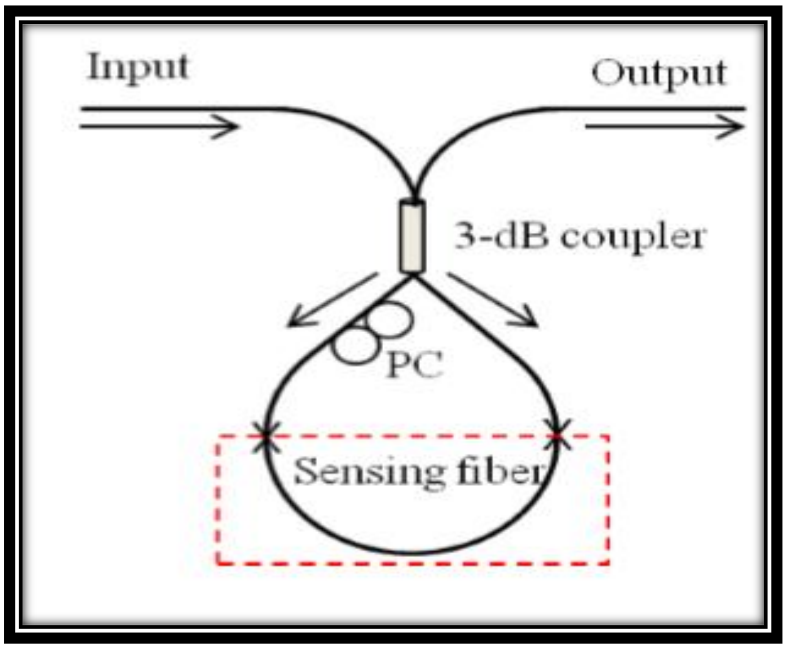

Figure 1.16: The schematic diagram of the sagnac interferometers (SIs) [60].

1.8.3 Mach-Zehnder Interferometers (MZIs)

The MZIs are the most common type of interferometers in sensing applications according to their flexibility. As shown in figure (1.17), the MZIs structure formed of two 3-dB coupler and two independent arms which are the reference arm and the sensing arm. The incident light is split into two beams in the first 3-dB coupler and then recombined by the second 3-dB coupler [61].

According to optical path difference (OPD), the interference appears in the recombined light between the two arms. For the sensing applications, the reference arm is maintain isolated from outer variation and only the sensing arm is exposed to the changing. Then, the variation in the sensing arm induced by such strain, temperature and RI changes the OPD of the MZI, which can be easily detected by analyzing the change in the interference signal [62]

Sometimes, the scheme of in-line waveguide interferometer is take place instead of the scheme of using two separated arms in the MZI since the apperance of long period fiber gratings (LPGs) as illustrated in figure (1.18a). Apart of the beam guided as the core mode of a SMF is coupled to cladding modes of the same fiber by an LPG, and then re-coupled to the core mode by another LPG.

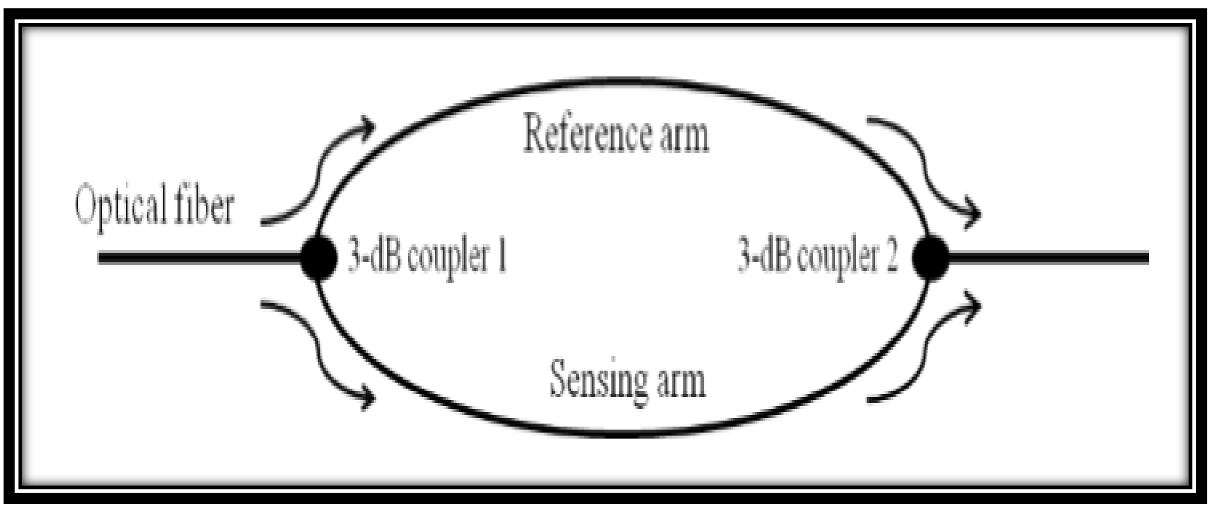

Figure1.17: The scheme of the MZI [63].

This in-line type of MZI had different optical path difference but the reference arm and the sensing arm have the same lengths [64].

Dividing a beam into the core and the cladding modes of optical fiber is splicing two fibers with a minute lateral offset can considers as one of the methods as seen in Figure (1.18b). According to the offset, a part of the core mode beam is coupled to multiple cladding modes without being heavily influenced by the wavelength [65].

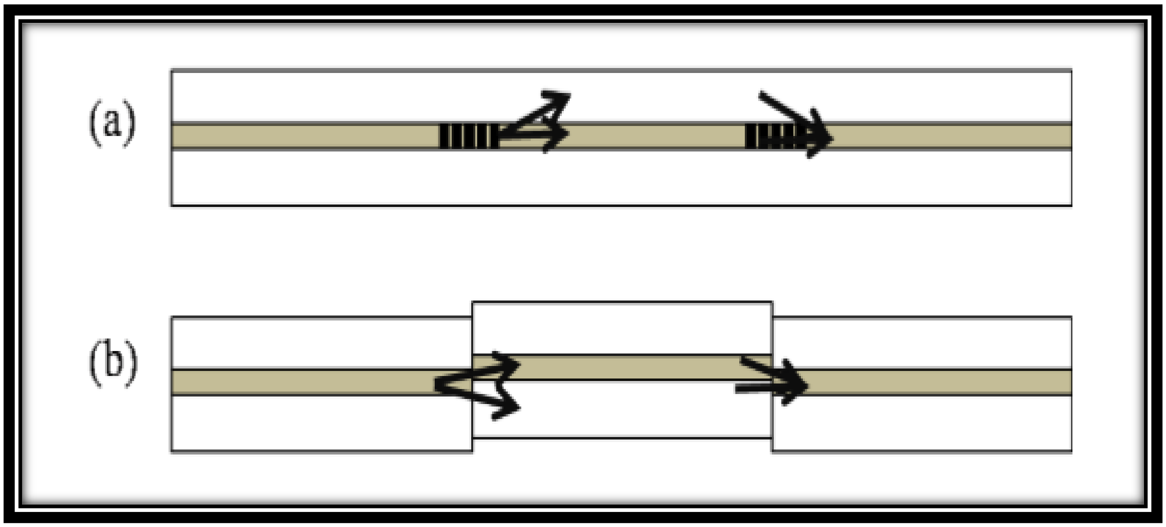

Figure 1.18: (a) a pair of LPGs [64], (b) core mismatch [65].

1.8.4 Michelson Interferometers (MIs)

The Michelson interferometers (MIs) are similar to the MZIs, the main principle of this interferometer is the interference between the sensing arm and the interference arm however in the end of each arm the beam is reflected as shown in figure (1.19a). In fact, the MI is similar in work to the MZI but depends on the reflectors. It is fundamental to check the fiber length difference between the sensing arm and the reference arm of an MI within the coherence length of the light source [66].

An in-line positioning of MI is also possible as viewed with Figure (1.19b). A section of the core mode beam is coupled to the cladding mode(s), which is reflected along with the uncoupled core mode beam by the mutual reflector at the end of the optical fiber [66].

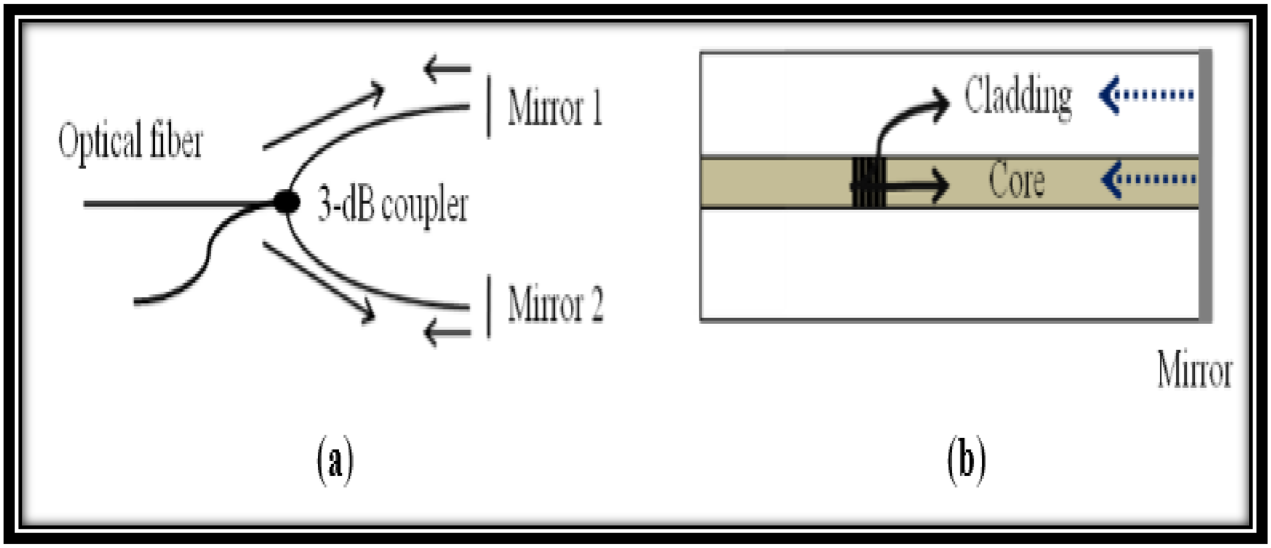

Figure1.19: (a) Main configuration of a Michelson interferometer and (b) The schematic of in-line Michelson interferometer [66].

1.9 Literature review

Recently, the researchers became more interested in the refractive index sensors because it’s have wide uses in different applications. In the past ten years, MZI has been proposed and constructed experimentally with different optical fiber types and configurations. The survey will be focused on this approach. The most significant published work are summarized in table (1.1).

Table (1.1): Summary of the Published Works in Refractive Index Sensor.

Year	Author	A brief of Published Work	Sensitivity	Reference
2010	J. Wang et al	Mach–Zehnder interferometer (MZI) coupled microring is demonstrated experimentally to obtain a high sensitivity as well as a large range for measuring change in refractive, BBS (1520-1620) nm , RI (1.0 -1.538)	111 nm/RIU	67
2011	J. Yang et al	Taper-based Mach–Zehnder interferometer (MZI) embedded in a thinned optical fiber is demonstrated as a highly sensitive refractive index (RI) sensor by decreasing the diameter of the thinned fiber and increasing the interferometer length of the MZI, BBS (1460-1580) nm, RI (1.33-1.42), (1.33-1.38).	2210.84nm/RIU 430.2 nm/RIU	68
2011	J.Yang et al	Femtosecond laser micromachining and arc fusion splicing were used to concatenating two micro air-cavities with two SMF to proposed Highly sensitive and robust refractive index (RI) fiber sensors, BBS (1450-1600) nm, RI (1.33-1.36)	172.4 nm/RIU	69

2012	L. Xue et al	Enhance the sensitivity of singlemode-multimode-singlemode (SMS) fiber structure in the measurement of surrounding refractive index (RI) depositing the multimode fiber section with a high RI overlay , BBS (1520-1600) nm, RI (1.31-1.35)	900 nm/ RIU 206 nm/ RIU	70
2012	H-Y. Lin et al	A tapered optical fiber sensor based on LSPR for RI sensing and label-free biochemical detection by using gold nanoparticle, BBS (1450-1600)nm, RI (1.33-1.403).	392.3 nm/RIU	71
2014	C. Chen et al	e Mach-Zehnder interferometer (MZI) used to test changes in the refractive index of sucrose solutions. RI (1.33-1.37) by using e two optical coupling structures are a duplicate of the beam splitter.	59.7 nm/ RIU	72
2014	J. Gabriel Ortega-Mendoza et al	optical fiber sensor based on the principle of local surface plasmon resonance to measure the refractive index in aqueous media using silver nanoparticles, pulsed laser used as a source.	67.6 nm/RIU	73
2014	Z. Liu et al	Demonstrated the refractive index (RI) characteristics of	131.64nm/RIU	74

		a singlemode-claddingless-singlemode fiber structure filter based fiber ring cavity laser sensing system, Fiber laser (1555-1565), RI (1.333-1.3707).		
2015	H. Luo et al	measurement of refractive index (RI) and temperature based on a microfiber-based dual inline Mach–Zehnder interferometer (MZI), BBS (1510- 1590) nm, RI (1.331-1.335)	-23.67 nm/RIU & 81.2 pm/ °C 3820.23 nm/RIU & -465.7 pm/ °C	75
2016	Q. Wang et al.	Mach-Zehnder mode interferometric refractive index sensor, which is based on splicing points tapered SMF-PCF-SMF (SMF, single-mode fiber; PCF, photonic crystal fiber) structure with different taper diameter, BBS (1530-1550) nm, RI (1.33331.3737)	260 nm/RIU	76
2017	Q. Wang et al	A high sensitivity of splicing regions tapered photonic crystal fiber (PCF) Mach–Zehnder Interferometric refractive index (RI) sensor compared with cascaded bi-tapered single-mode fiber (SMF) Mach–Zehnder interferometer (MZI), ASE (1535-1565) nm, RI (1.33-1.38).	240.16 nm/RIU	77

2017	N. A. Salman et al	Photonic Crystal Fiber Interferometer Based On Refractive Index sensor for different refractive index of direct splicing and splicing points tapered SMF-PCF-SMF Mach- Zehnder interferometer, Laser Diode 1550 nm , RI (1.33-1.38)	7.4 pm /RIU	78
2018	S-A. Mohammed et al	A refractive index sensor based on the multimode interference theory by using the coreless fiber, BBS (1500-1600), RI (1.33-1.38)	340.85 nm/RIU	79
2019	H.DU et al	A high sensitive refractive index sensor based on the cladding etched photonic crystal fiber (PCF) Mach-Zehnder interferometer (MZI), RI (1.33-1.38)	211.53 nm/RIU 359.37 nm/RIU	80
2019	W.Yang et al	A novel tapered-single mode-no core-single mode (TSNS) fiber refractometer based on multimode interference, RI (1.33-1.417).	1517.28nm/RIU	81
2020	T. Li et al	An Ag- graphene layers-coated H-shaped photonic crystal fiber (PCF) surface plasmon resonance (SPR) sensor with a U-shaped grooves open structure for refractive index (RI) sensing,	2770 nm/RIU	82

		RI (1.33 to 1.36).with the air hole diameter of .		
2020	N.A. Hamza	Refractive index sensor based on multimode interference using SCS structure to measure the changes in refractive index for different fluids and NaCl solution. RI (1.33-1.35),(1.33-1.38) with CF diameter of 50 μm	1058 nm/RIU 1012 nm/RIU	This work

1.9 The Aim of the work

1. Fabrication of the refractive index sensor based on coreless fiber as the sensing element.

2. Measuring the variation in the refractive index of NaCl solution.

3. Study the influence of changing the diameter of the coreless fiber on obtained sensitivity.

CHAPTER TWO

Experimental setup and Procedures

2.1 Introduction

This chapter clarify the components that are used during the experimental work, the sensing elements of the experiment setup and the procedures. The interferometers used in many applications because of their benefits. Many researchers had been established and investigated many types of interferometers such as MZI which consider one of the interferometers that have a wider uses in sensing field for measuring different parameters such as concentrations and refractive indices. The refractive index sensor is the most common sensor and had been fabricated and enhanced in this work by using different lengths and diameters of coreless fiber as shown in the flow chart below.

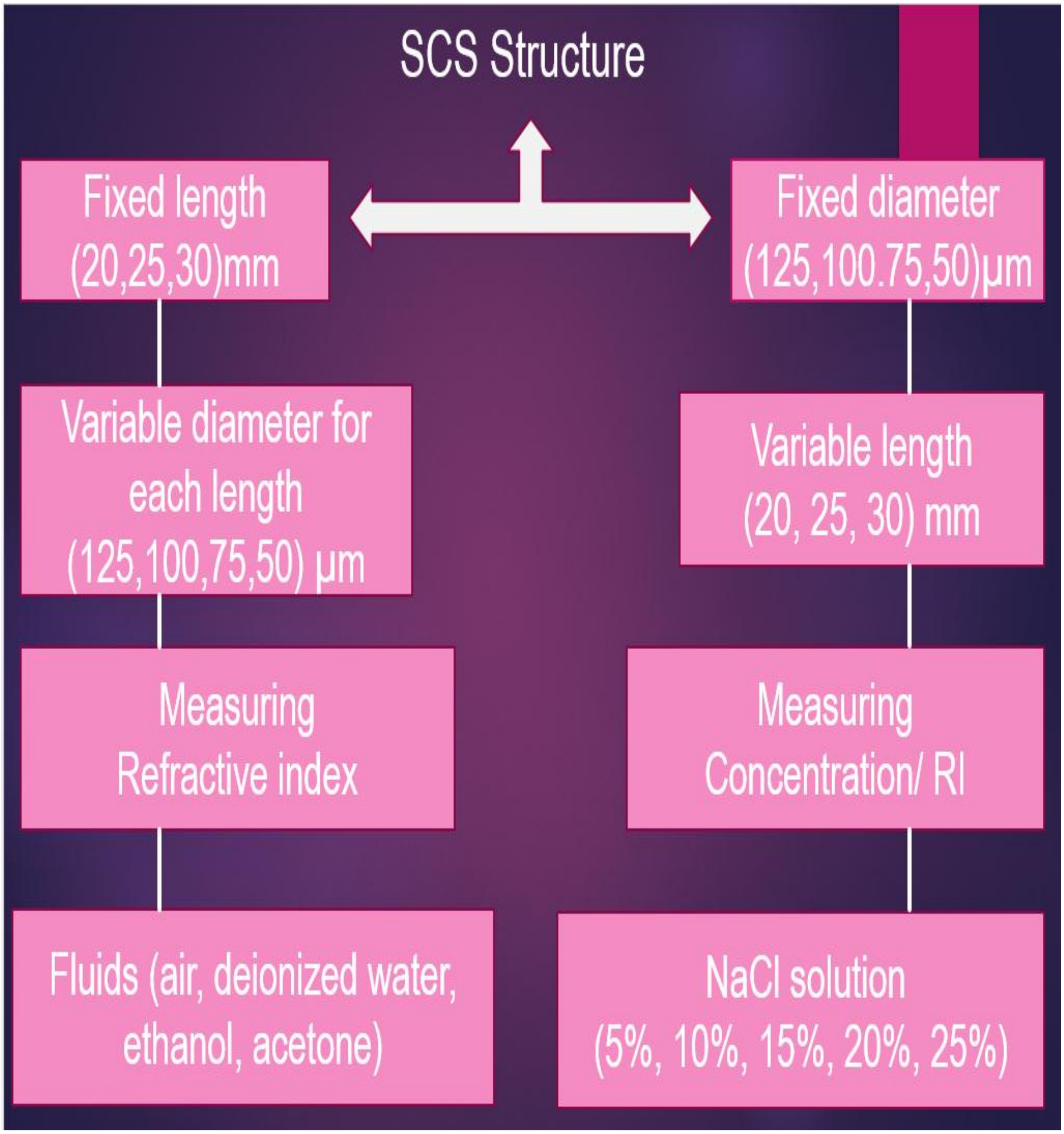

Figure (2.1): The flow chart of the experiment work of the RI sensor.

2.2 The broadband Source (B.B.S)

In these experiments, a broadband source as shown in figure (2.2) was used with a wavelength range (1500-1600) nm having output spectral near Gaussian profile and low ripple from Thorlabs Company. The B.B.S contains of four parts: Superluminescent laser diode (SLD IC Chipset), Laser Mount (LM), Temperature Controller (TED200C) and Laser Diode Controller (LDC210C). The most important part in B.B.S is the IC chip (composed of 14-pins Butterfly laser diode) where the light transmitted from the IC chip has 14 pins to fix it in LM. LDC control the operating current and the threshold current. The TED function is to stabilize the emitting wavelength through controlling the standardized operating temperature. (Appendices A, B, C, and D).

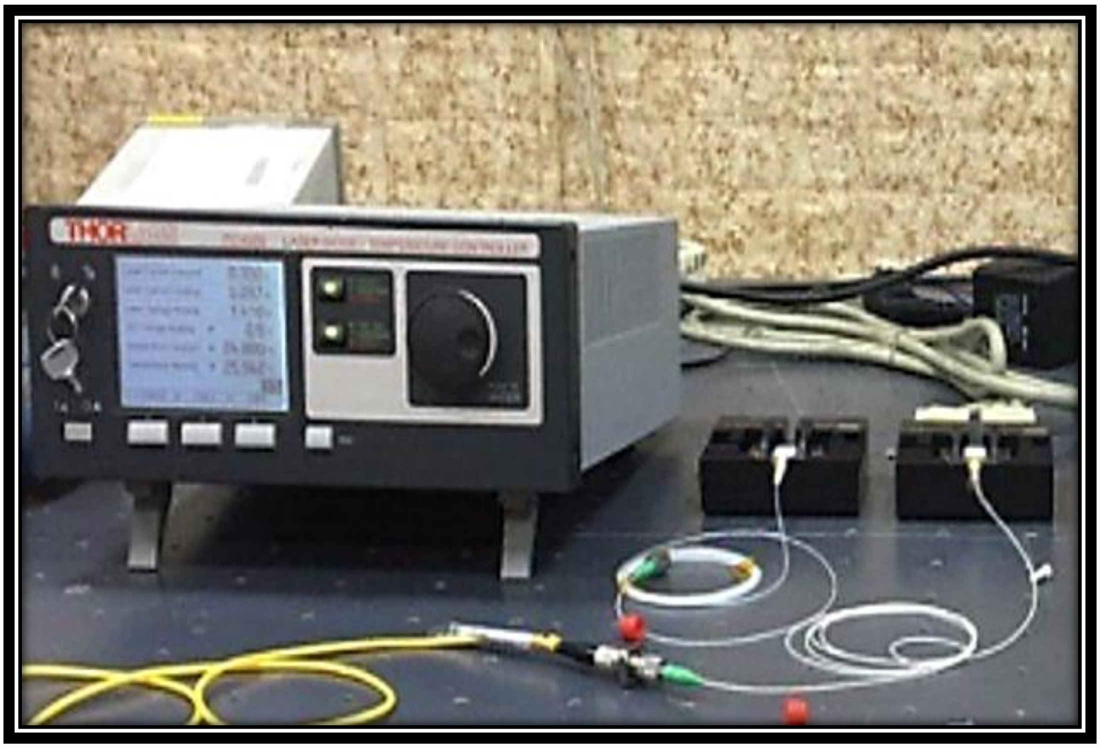

Figure (2.2): The broadband source (BBS).

2.3 Single Mode Fiber (SMF-28)

This type of fibers is made to be the main chain in specific specialties in optical communications and the sensing applications for its tiny losses, fast transfers, highest information-carrying capacity, high strength, lowest dispersion and the simplicity in handling. The Specifications of SMF-28 can be seen in the table (2.1).

Table (2.1): The specifications of SMF-28.

Mode Field Diameter MFD	
Wavelength (nm)	MFD Values (μm)
1310	9.2 ± 0.4
1550	10.4 ± 0.5
Dispersion	
Wavelength (nm)	Dispersion value[(ps/(nm*km)
1550	≤ 18.0
1625	≤ 22.0
Fiber Attenuation	
Wavelength (nm)	Maximum value (dB/km)
1310	0.33-0.35
1550	0.19-0.20
1625	0.20-0.23

2.4 Coreless fiber (CF)

The Thorlabs Company made a special type of multimode fiber which is called the coreless fiber FG125LA and represent the sensing element in this work. To reduce the damage in fiber or prevent the back reflections the CF can be spliced to the SMF-28 and the return loss is more than 65 dB with 0.25 m length of termination fiber. The wavelength range (400 – 2400) nm with different refractive indices but for the operation wavelength of 1550 µm, the refractive index is 1.444. The specifications of the CF can be shown in table (2.2).

Table (2.2): The specifications of the CF [Appendix E].

Coreless Fiber specifications	
Glass Refractive index	1.467287 @ 436 nm 1.458965 @ 589.3 nm 1.450703 @1020 nm 1.444 @1550 nm
Wavelength range (nm)	400-2400
Glass Diameter (µm)	125±1
Coating Diameter (µm)	250±5%
Operating Temperature C^o	-40 to 85

2.5 Instrument of Optical Fiber Preparation

2.5.1 Optical Fiber Stripper

To preparing the optical fiber for the sensing purposes, the protecting layer has to be removed by a stripping tools. As a first step, the coating will be removed by a stripping tool as the (JIC- 375 Tri – Hole) which consider as a traditional stripper. In all common fiber stripping function there are three holes. The first hole is utilized to strip the (1.6 to 3) mm protective coating, the second hole is to strip the second buffer coating, and the third hole is utilized to strip the Acrylate coating.

2.5.2 Fiber Optical Cleaving

The second step in preparing the optical fiber is the cleaving process. The fiber cleaving instruments are applied by Fujikura (CT-30) as illustrate in Figure (2.3).

The cleaving machine allow for clamping the optical fiber through a clear position, and offered to make an optical fiber flat face and perfectly smooth. Through holding the optical fiber low tension and to trigger the operation of cleaving via touching the end of optical fiber via a vibrating blade and by cleaving is to cut the end of optical fiber in 90o angle to achieved flat end cleaved surfaces.

Figure (2.3): Optical fiber cleaver (CT-30).

To clean the standard single mode fiber and the coreless fiber, a wet wipe, alcohol or another solvent should be used. When the CF is being cleaned, the fiber tip should not be exposed to liquids for cleaning the optical fiber after cleaver, which may cause the liquid to infiltration through the optical fiber microstructure, resulting in failure of sensing operation, and possible damage. A dry wiping was utilized to remove the remaining coating after striping. The optical fiber ends must be checked under a microscope and then cleaved again in case that the tip of optical fiber is not smooth. As shown in figure (2.4)

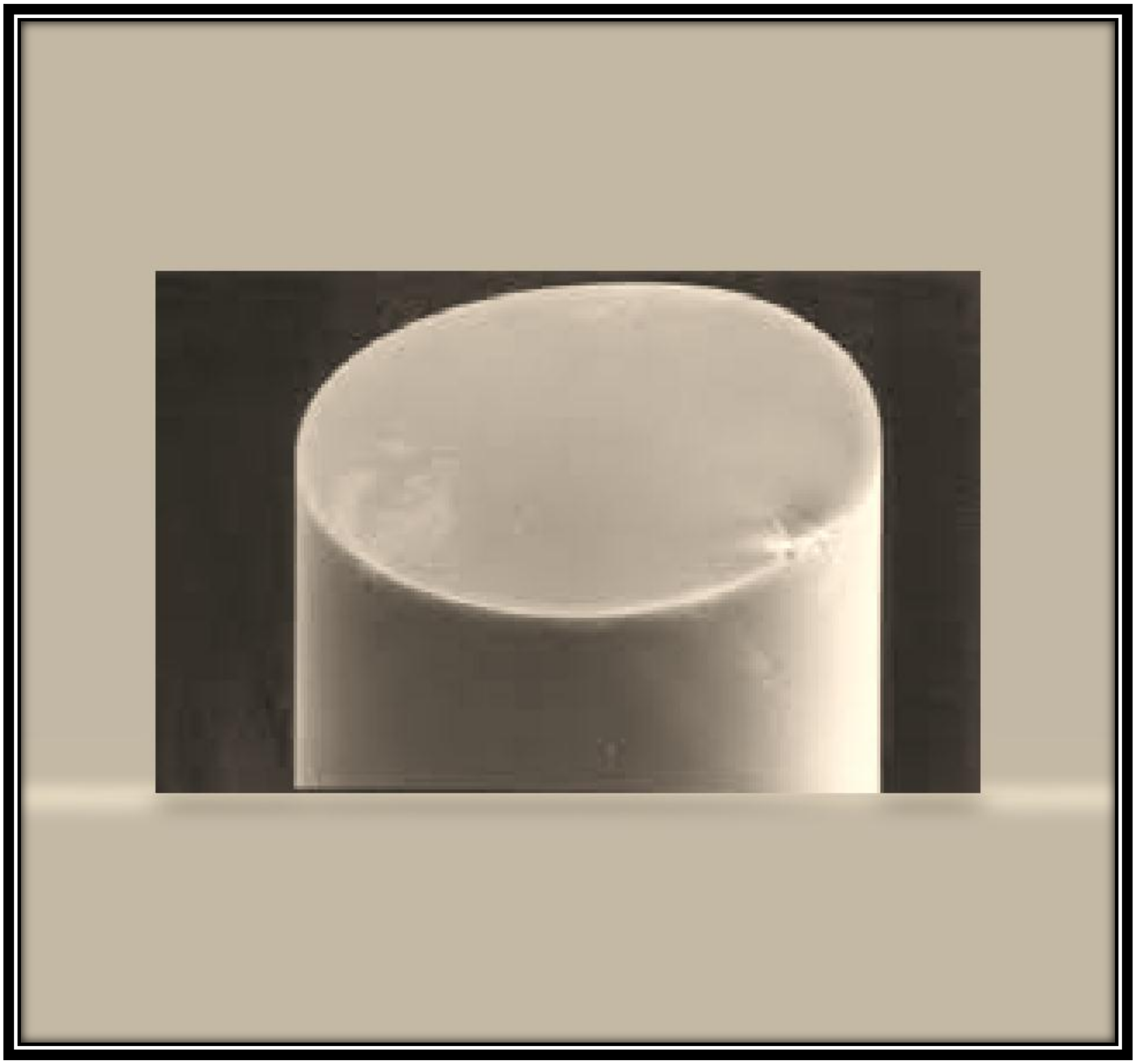

Figure (2.4): Microscope images of CF edges after cleaving.

2.6 Optical Spectrum Analyzer (OSA)

There are several types of the instruments that designed to monitor the sensor interference spectra. As shown in figure (2.5), the AQ6370 is Yokogawa's high speed and high performance Optical Spectrum Analyzer for characterization of optical communications system and optical components. The properties of the OSA can be shown in table (2.3).

Table (2.3): OSA (YOKOKAWA, Ando AQ6370) properties.

Wavelength range	(600-1700) nm
Wavelength resolution	High (0.2 nm)
Dynamic range	70 dB
Wavelength meter accuracy	±0.01nm
Applicable to	Single Mode and Multimode fiber test capability
Measurement range (power)	+20 dBm to -90 dBm
Measurement time	0.2 sec (100nm span)
Operating System	Has two USB 1.1 compatible interfaces. They support large size removable memory devices such as Flash ROM and hard disk drives (HDD).

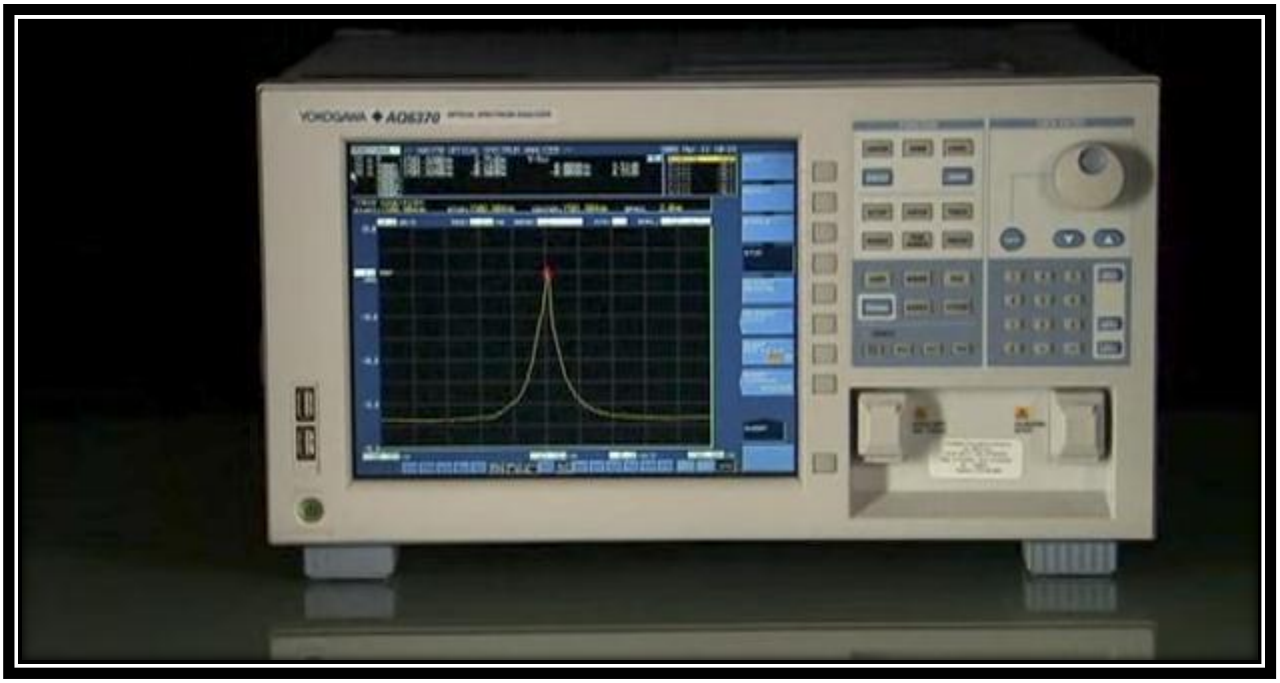

Figure (2.5): The optical spectrum analyzer (OSA).

2.7 The Procedures of the Experimental Work

To get the experimental results correctly, a few procedures had been done and will be mention below:

2.7.1 The Optical Fiber Splicing

After the preparation of the fibers, a fusion splicer Fujikura (FSM-60S) as shown in figure (2.6) was used to splice the SMF with the CF. This step was carried out after stripping the outer coating of the fiber (SMF and CF) and cleans the fibers before the splicer process has begun. The SMF sections have a core and cladding diameters of 9 μm and 125 μm, respectively with a 1.451 and 1.444 refractive indices for the core and cladding, respectively.

While the CF section has a diameter of 125 μm diameter with a similar refractive index of 1.444 at a 1550 nm. This process was performed by using two SMF sections with length of 20 mm for each section and the CF section with different 3 lengths of (20, 25, 30) mm, these two sections will be spliced with the CF as a sandwich. After building the structures, the sensing section (CF) should be etched for more enhancements in the sensing process.

Figure (2.6): the fusion splicer Fujikura (FSM-60S).

The typical steps to perform fusion splicing are: Remove any outer coating from the fiber using stripper then cleave the fiber end at right angles with 90o using clipper and clean the fiber ends with tissue and alcohol after that align the fiber ends in V- groove in fusion splicing machine precisely with a small gap in between the fibers. Press the set, the splicing motors will align the fiber ends and Arc fusion will start and check the quality of splicing by measuring the output power for the obtained spliced fiber, at the end Protect the splice region through the use of a heat shrink protector or a mechanical crimp protector.

2.7.2 The SMF-CF-SMF Structure

The RI sensors structure (Single Mode fiber- Coreless Fiber- Single Mode fiber) is proposed and fabricated by using different lengths of CF spliced between two pieces of SMF. The SCS structure of the optical fiber sensor is depend on principle of the multimode interference (MMI) which occurs while the core mode of the lead in single mode fiber section, a number of high-order modes are excited and propagated along the coreless fiber, at the other splicing point, the high-order modes are coupled and backwards to the core fiber of the single mode fiber [75]. The sensing section can be presented by the coreless fiber (CF) with different lengths surrounding by solution with variable concentrations (variable refractive index), where the sensing section is spliced between two single mode fibers (SMF).

Figure (2.7) represents the optical sensor system by using the coreless fiber (Thorlabs Inc.).

The schematic diagram consists of the broadband source (Thorlabs B.B.S) with wavelength range (1500 – 1600) nm which connected to the SCS structure from the first section of SMF (Coring SMF-28). Where SMF spliced to coreless fiber (three different lengths) by fusion splicer (Fujikura FSM-60S) and the interference between the fundamental mode and the higher-order modes happens in a second spliced area between the CF and SMF.

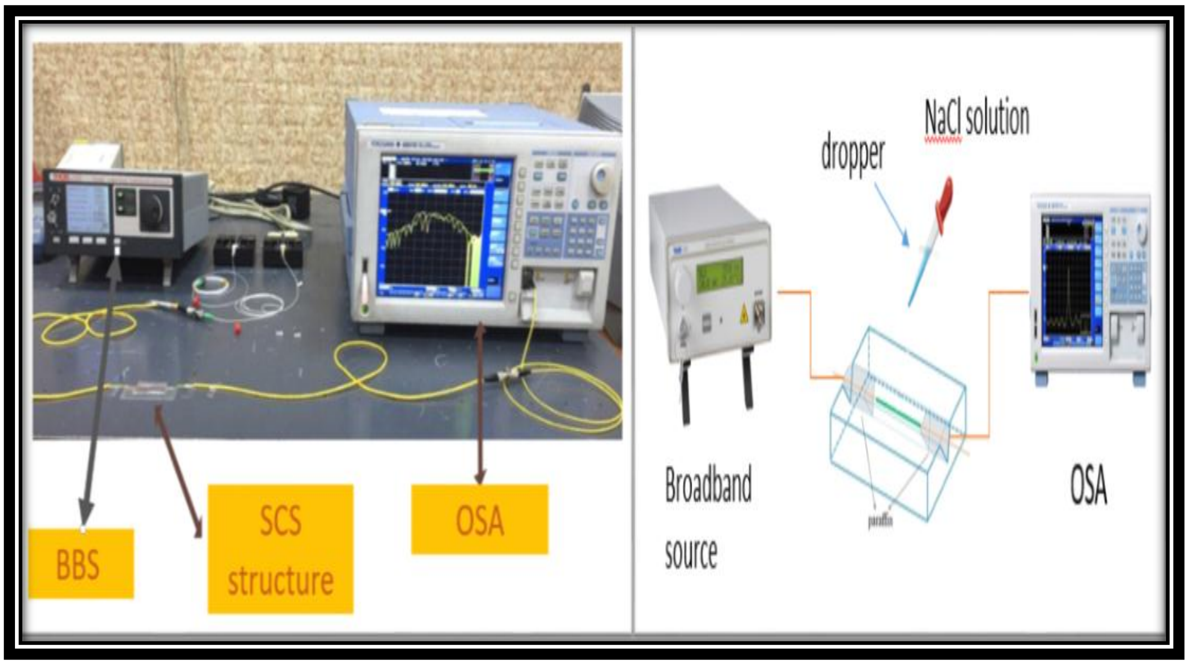

Figure (2.7): The RI sensor system.

2.7.3 The Coreless Fiber (CF) Etching Process

The refractive index sensing area includes CF with different lengths of (20, 25 and 30) mm, while the diameter is changed three times for every length to enhance the sensitivity of the sensor. The diameter can be changed by using a technique that cause a reduction in the CF diameter for different values, it’s called the etching process.

The etching process or as known the chemical etching is done by using the chemical solution called hydrofluoric acid (HF) solution with a concentration 40 %.

The reduction of the CF diameter was spotted after submerging the coreless fiber in HF liquid for a few minutes, then removing the CF from the HF and clean it with ethanol or deionized water. The time of etching is changed as the required diameter as shown in the table (2.4).

Table (2.4): The time of etching in minutes for each diameter of CF.

The CF diameter (µm)	The etching time (min)
125	0
100	13
75	23
50	36

The etched fiber will be suffer from chemical changes in its surface and to ensure that the fiber have a smooth surface with no fractions, a microscopic images can be taken by a transmission optical microscope (Euromex Company, Holland) as shown in figure (2.8)

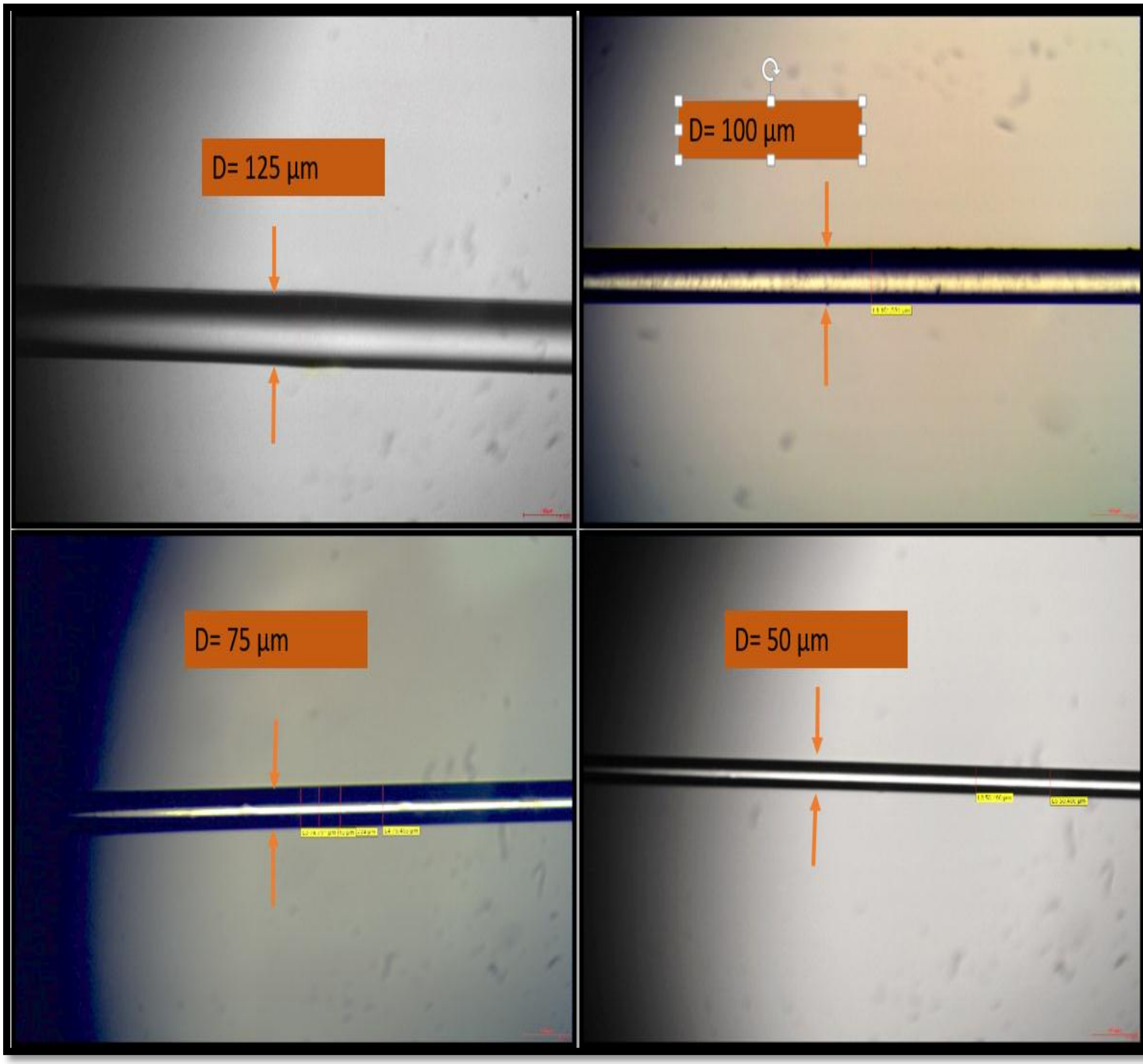

Figure (2.8): The Microscopic images of the CF diameters after etching (10X).

Figure (2.9): The transmission optical microscope (Euromex Company, Holland).

2.8 The Sodium Chloride (NaCl) Solution Preparation

The testing solution (sodium chloride solution) was prepared by taken a different concentration values of the NaCl powder (5, 10, 15, 20 and 25) mg weighted in electrical scale for more accuracy. These concentrations will be dissolved in a 100 ml of deionized water by the magnetic stirrer at room temperature (25C^{o}).

The testing solution with different concentrations (0%, 5%, 10%, 15%, 20% and 25%) are used as samples with different RIs. Abbe refractometer (Abbe refractometer is a bench-top device utilized for refractive index measurement with high degree of accuracy. Analogue Abbe Refractometer (AR4) fabricated by Krüss is used for refractive index measurement. AR4 offers reading via eyepiece. It has temperature controlled prisms, thermostat connections for prisms, and an adjustable scale) measured the RI of the solution with 1.333 to 1.382 range as shown in table (2.5). In our experiment the structure is totally submerged in the solution (NaCl solution) as shown in figure (2.10) and before each measurement, the structure is cleaning by the deionized water and dried in air.

Table (2.5): The concentrations of NaCl with their refractive indices.

The refractive indices (RIU)	The concentrations of NaCl (%)
1.33	0
1.34	5
1.35	10
1.36	15
1.37	20
1.38	25

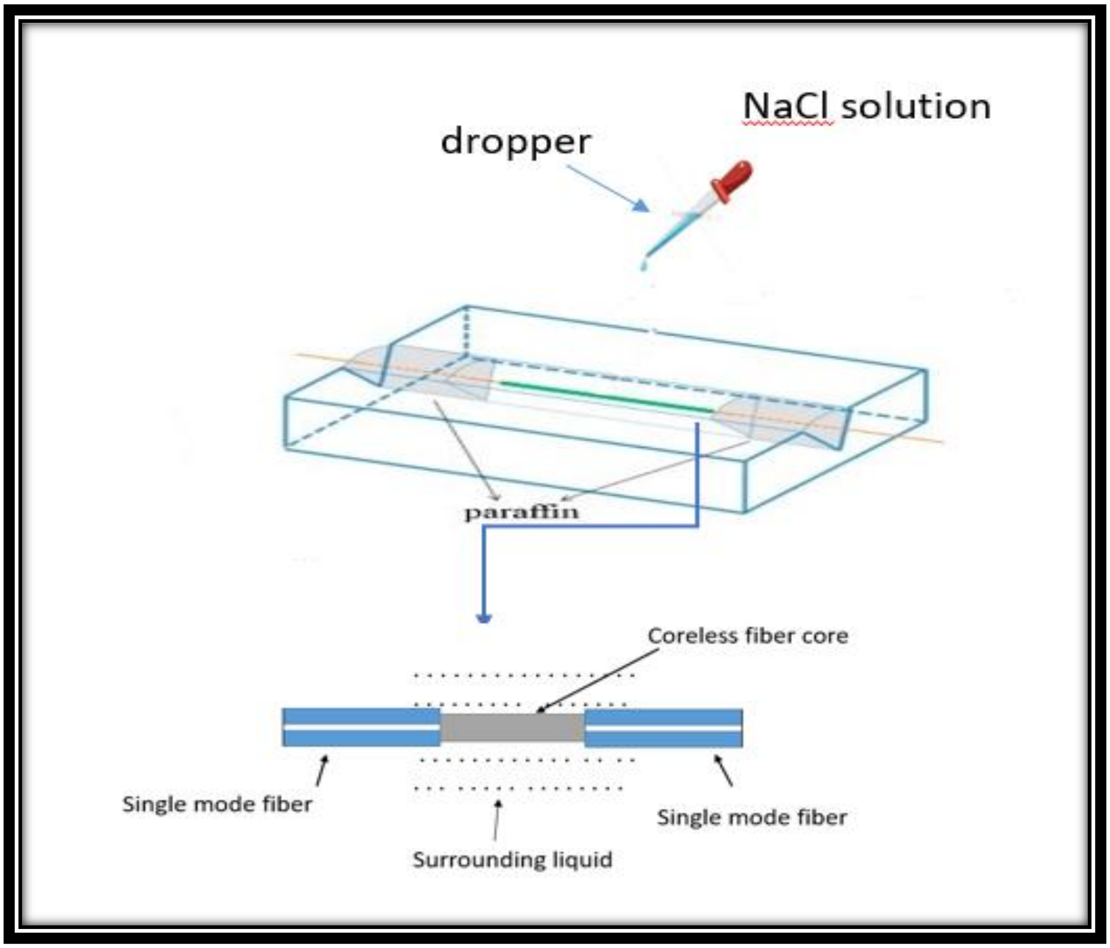

Figure (2.10): The NaCl solution testing process.

CHAPTER THREE

RESULTS AND DISCUSSION

3.1 Introduction

This chapter includes the results, discussion of the refractive index (RI) sensor based on multimode interference, conclusion and future work. To sense the change of the refractive index at different fluids, a refractive index sensor has been designed and demonstrated. The experimental results have been registered by the optical spectrum analyzer (OSA) and the sensor structure was illustrated by a broadband source (1500-1600) nm. The influence of the CF length and diameter were studied. This work also measures the sensing parameters (concentration /refractive index) of the NaCl solution and different fluids. These experimental results were recorded under a laboratory Circumstances at room temperature.

3.2 The Transmission Spectrum and the Stability of SCS Structure

The broadband source (B.B.S) transmission stability was tested to ensure the assurance of sensor measurements. As shown in Figure (3.1) the black bold curve represents the SMF test while for the SCS which represented by the red bold curve to test the function of the structure. This structure consist of CF spliced between two pieces of SMFs. The SCS filtered some of the wavelength so it acts as a band pass filter due to a multimode interference where the fundamental mode from the SMF at the first splicing region will split into multimode and coupled at the second splicing region. The single mode fiber structure (SS) and the SCS structure can be shown in Figure 3.2.

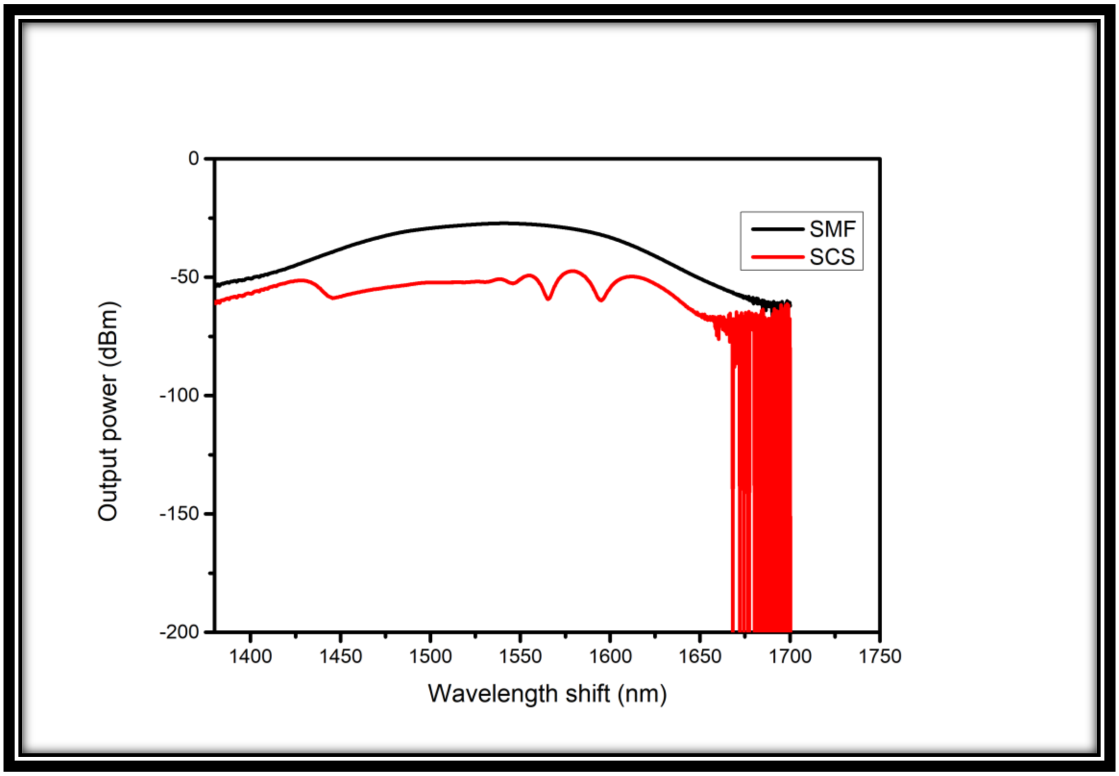

Figure (3.1): B.B. source transmission with SMF and SCS.

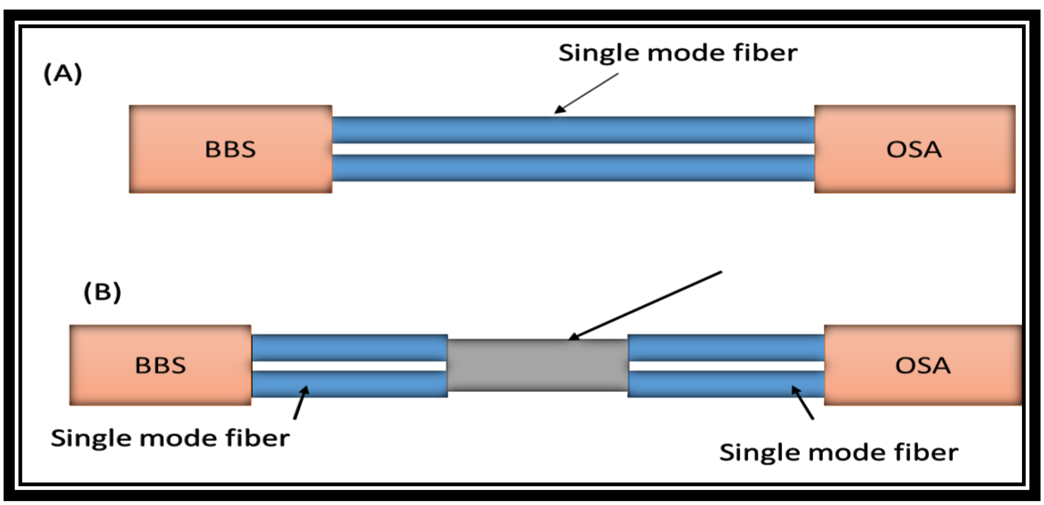

Figure (3.2): The schematic diagram of (A) SMF, (B) SCS.

3.3 The Influence of CF Length on the RI Sensor Sensitivity

In this work, the effectiveness of the CF length on the sensor sensitivity was studied by using a CF fixed diameter of 125μm with different CF lengths. The SCS structure was prepared by spliced two pieces of SMF with a piece of CF (20, 25, and 30) mm by fusion splicer. The first end of the structure connected to the BBS and the second end connected to the OSA. The changes of the refractive indices of the testing materials (solutions and fluids) were used to study the wavelength shift as function of refractive index which clarified by the experimental result as shown:

3.3.1: RI Sensor based on CF at different lengths

A different values (20, 25 and 30) mm of CF length was used in the experimental setup with different refractive index of (air, deionized water, ethanol and acetone) to measure the variation in wavelength shift. This variation can be seen in figure (3.3, 3.4 and 3.5) which represents the variation of the output power with the wavelength where the black line for air, red line for deionized water, blue for ethanol and purple for acetone. The results had shown the highest sensitivities for CF lengths (20, 25 and 30) mm are (255, 266.6 and 245) nm/RIU for acetone with wavelength shifts of (13, 13.6 and 12.5) nm respectively.

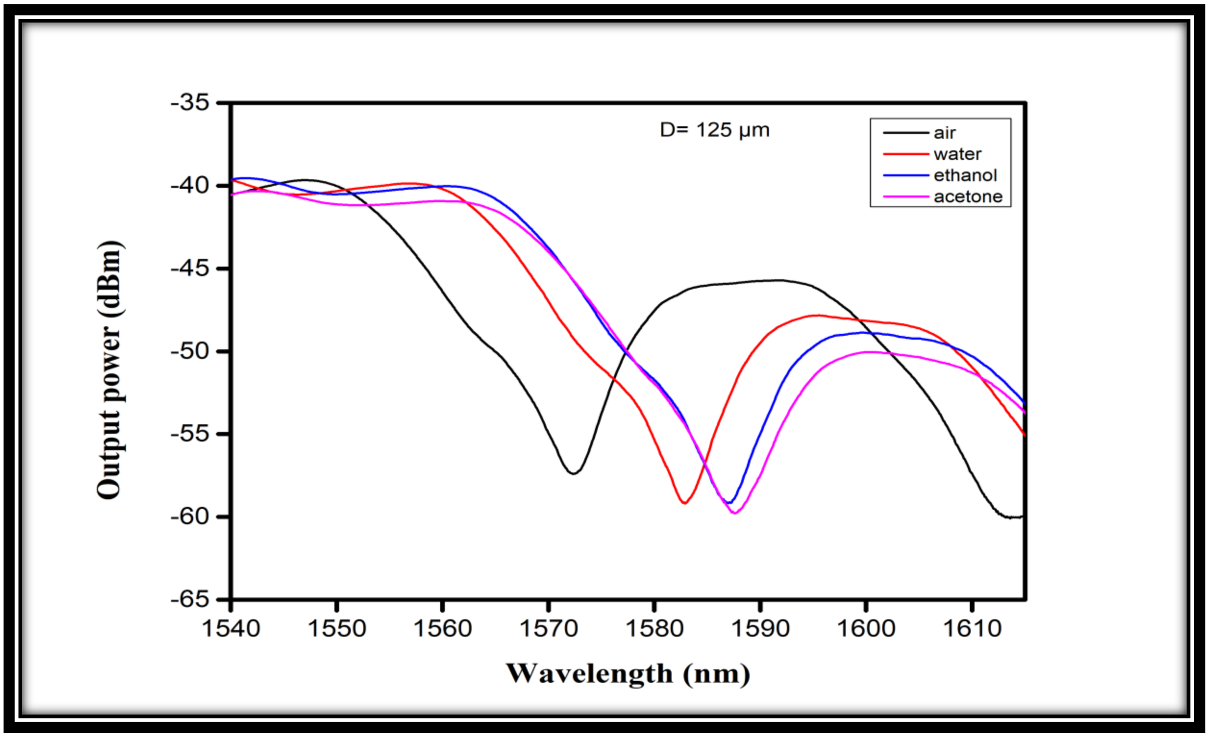

Figure (3.3): The output power versus wavelength for CF length of 20 mm.

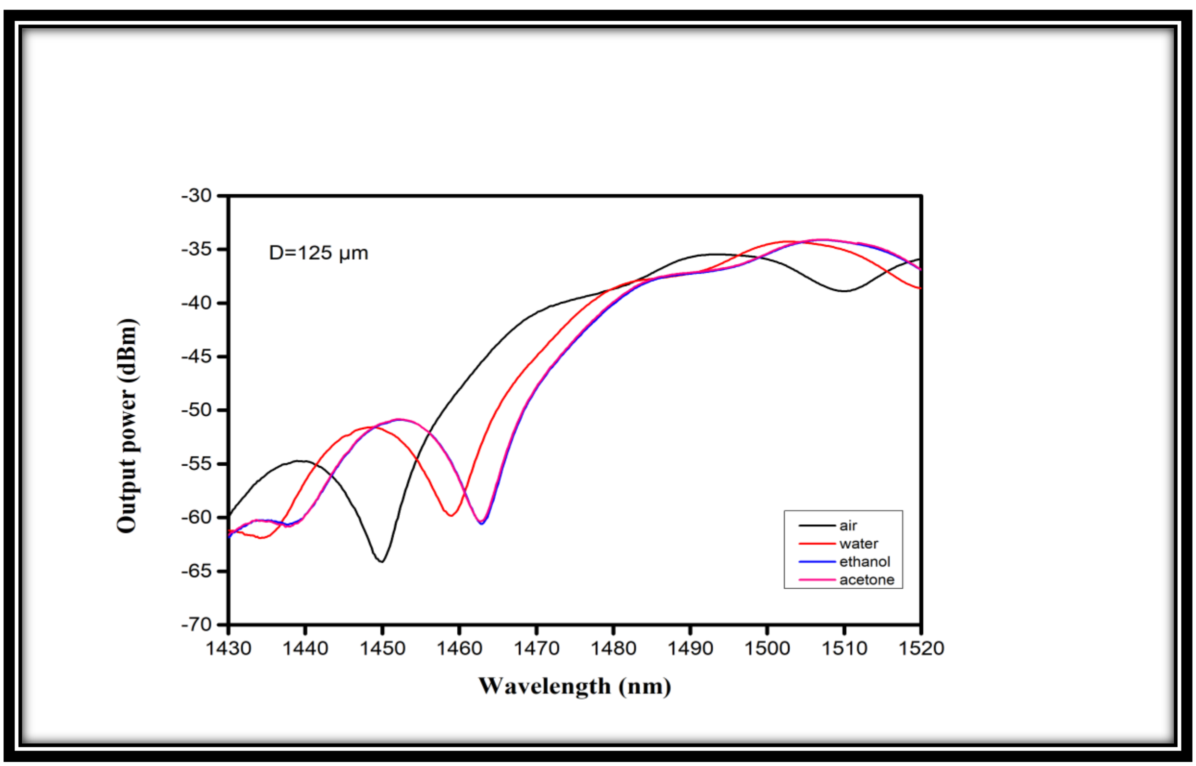

Figure (3.4): The output power versus wavelength for CF length of 25 mm.

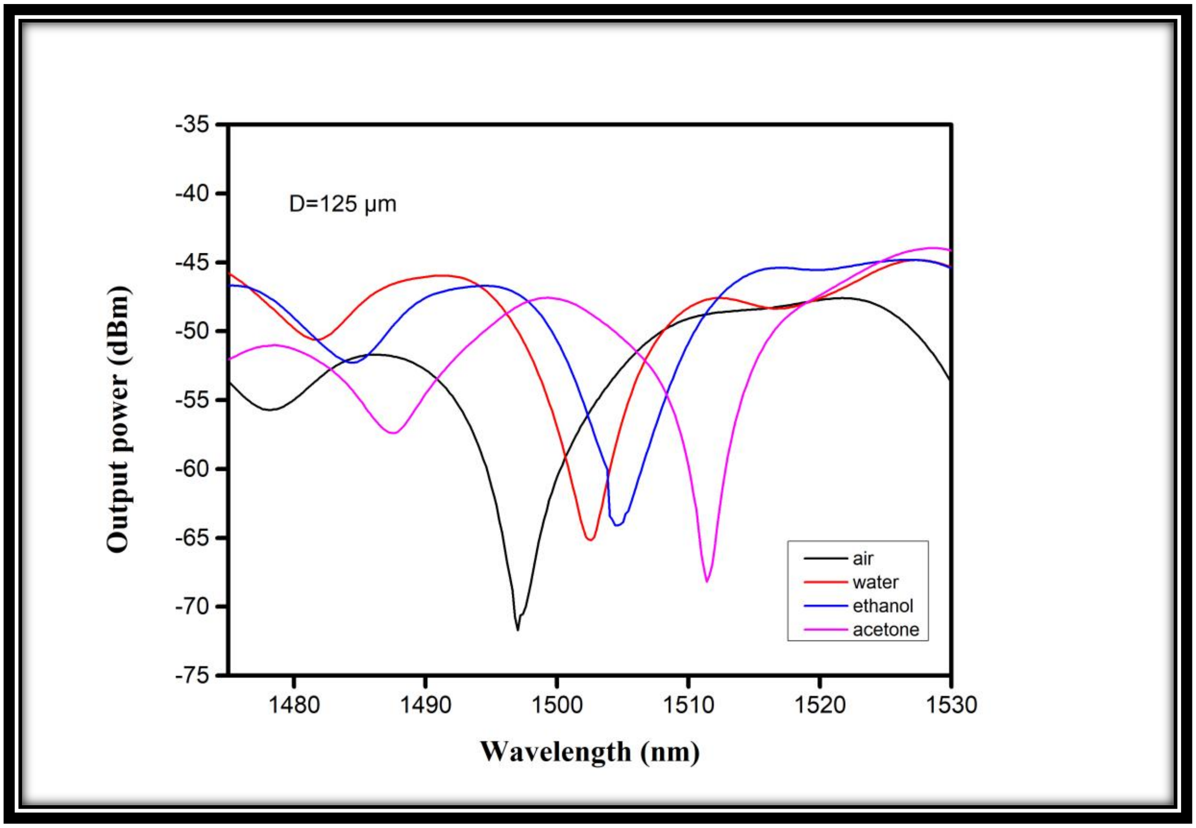

Figure (3.5): The output power versus wavelength for CF length of 30 mm.

3.4 Relation between CF Length and the RI Sensor Sensitivity

Since the wavelength is a function of refractive index as seen from Figures (3.3, 3.4 and 3.5), so the wavelength dips shifted toward longer wavelength (red- shift) when the refractive index increases from (1 for air to 1.3501 for acetone). The relationship between the refractive index and the wavelength shift can be seen in Figure (3.6). There was a slight variation in the wavelength shift and sensitivity for different CF lengths and fixed diameter, this because of the self-imaging on the MMI principle.

Table (3.1) represent the sensitivity with the different lengths of CF and fixed diameter at 125 μm.

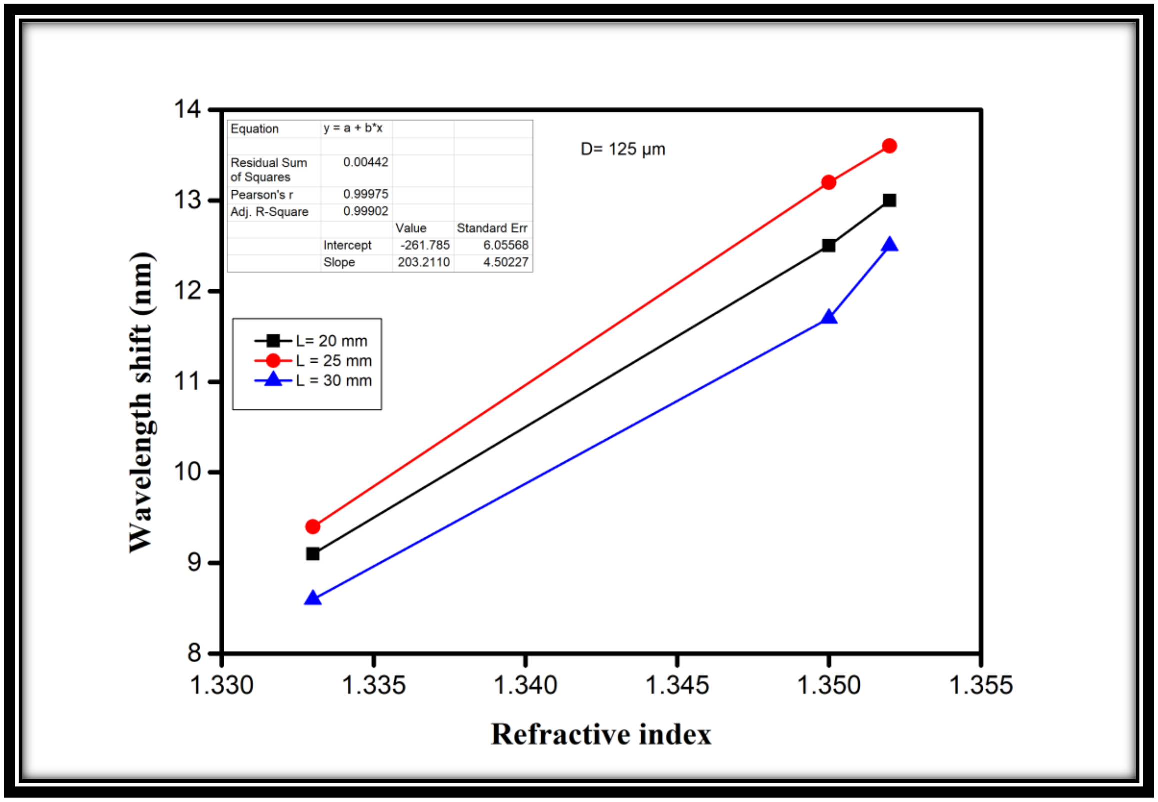

Figure (3.6): The wavelength shift versus the refractive index of different fluids with different CF lengths.

Table (3.1): The sensitivity of RI sensor with different CF lengths and fixed diameter.

CF length (mm)	Wavelength shift (nm)	RI sensor sensitivity (nm/RIU)
20	13	255
25	13.6	266.6
30	12.5	245

3.5 The etched CF Diameter Influence on the RI Sensor Sensitivity

The RI sensor sensitivity influenced by reducing the diameter of the CF to different values by the chemical etching process. The diameters were reduced for each CF lengths (20, 25 and 30) mm to enhance the sensitivity of RI sensor. The SCS structure was prepared by spliced the cleaved CF with two pieces of SMF by fusion splicer. The CF piece has been etched by the (40 %) HF to reduce the CF diameter from 125 µm to 100, 75 and 50 µm, respectively. This work has been demonstrated by testing the performance of the SCS structure by using different fluids (varies refractive indices). The wavelength shifts acts as the function of the refractive index and has been shown experimentally.

3.5.1 RI Sensor for Fixed CF Length of 20 mm with Different Diameters:

3.5.1.1 Etched CF Diameters of RI Sensor

After preparing the fixed CF length of 20 mm in the SCS structure, the CF diameter has been reduced for the values (100, 75 and 50) µm. A different fluids with different refractive indices have been shown in Figure (3.7, 3.8 and 3.9) where the colored lines in the transmission spectrum of black, red, blue and purple represents the refractive indices of air, deionized water, ethanol and acetone ,respectively.

The transmission spectrum had a maximum wavelength shifts of (21.6, 22.6 and 39.8) nm for acetone and the sensitivities of RI sensor are (423.5, 443.1 and 780.3) nm/RIU respectively.

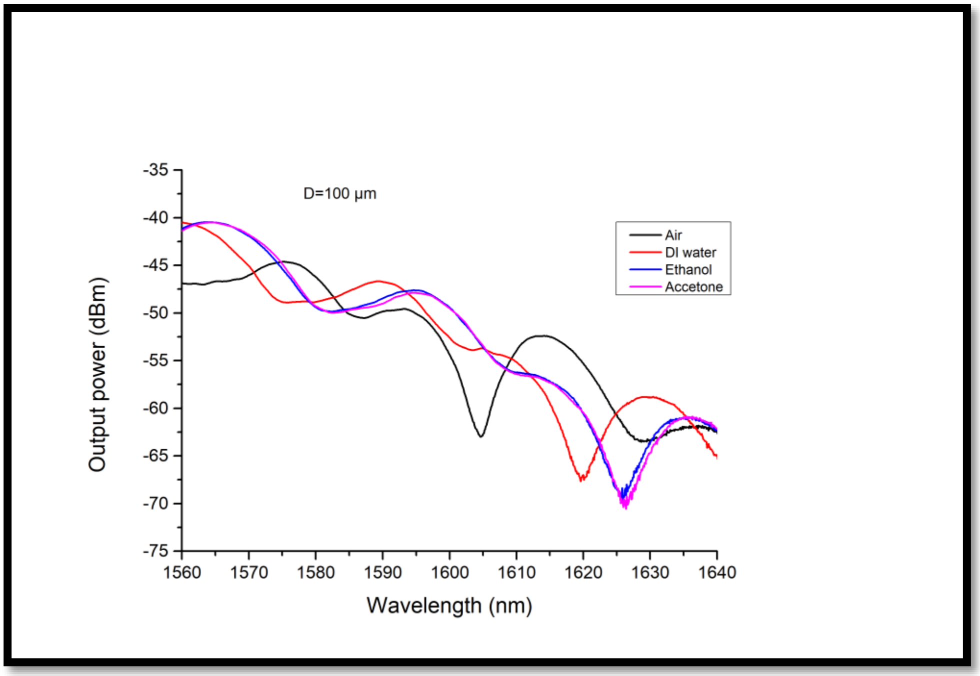

Figure (3.7): The output power versus wavelength for CF diameter of 100 µm and fixed length.

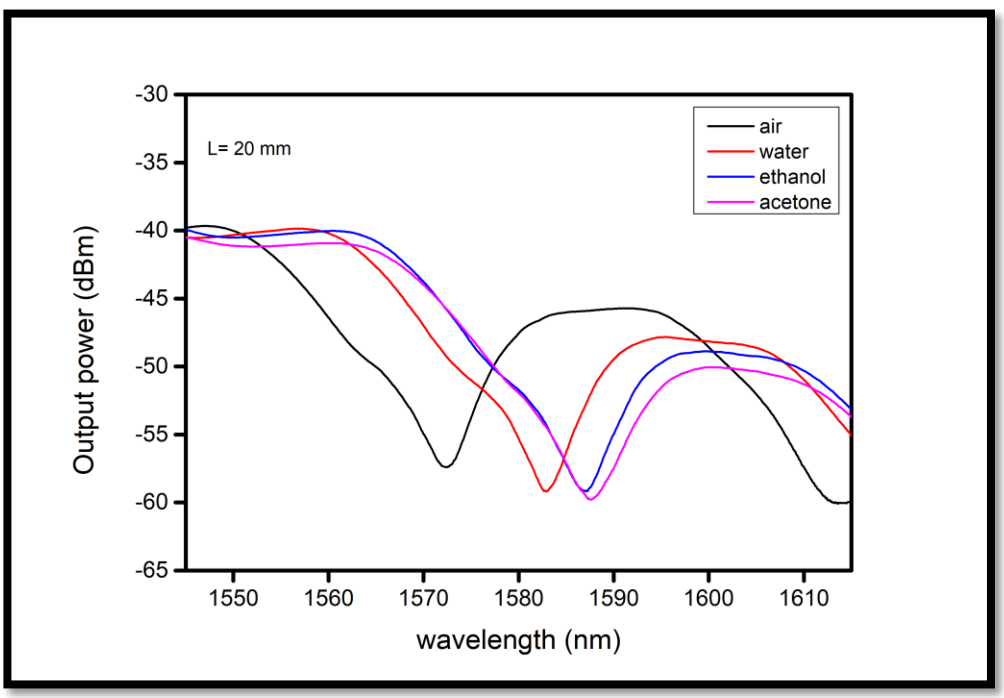

Figure (3.8): The output power versus wavelength for CF diameter of 75 µm and fixed length.

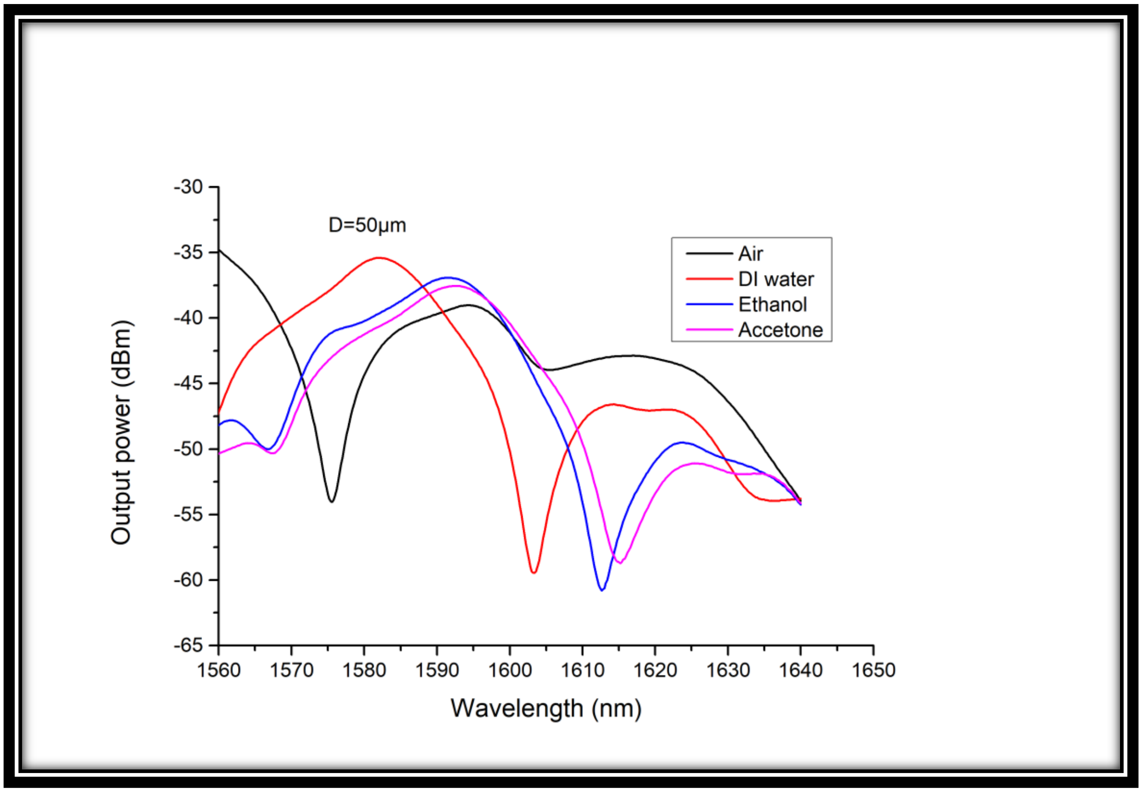

Figure (3.9): The output power versus wavelength for CF diameter of 50 µm and fixed length.

Table 3.2: The sensitivity of RI sensor for different CF diameters with fixed length at 20 mm.

CF diameter (µm)	Wavelength shift (nm)	Sensitivity (nm/ RIU)
100	21.6	423.5
75	22.6	443.1
50	39.8	780.3

3.5.2 RI Sensor for Fixed CF Length of 25 mm with Different Diameters:

3.5.2.1 Etched CF Diameters of RI Sensor

After preparing the fixed CF length of 25 mm in the SCS structure, the CF diameter has been reduced for the values (100, 75 and 50) µm. A different fluids with different refractive indices have been shown in figures (3.10, 3.11 and 3.12) where the colored lines in the transmission spectrum of black, red, blue and purple represents the refractive indices of air, deionized water, ethanol and acetone ,respectively.

The transmission spectrum had a maximum wavelength shifts of (20.2, 26.8 and 54) nm for acetone and the sensitivities of RI sensor is (396.07, 525.4 and 1058) nm/RIU respectively.

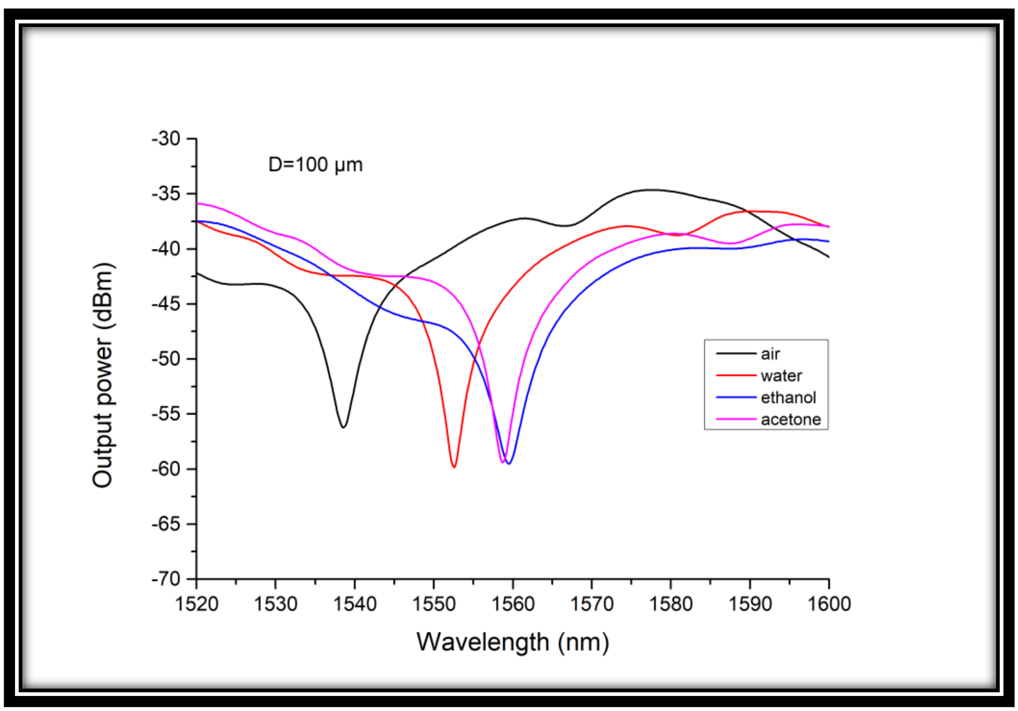

Figure (3.10): The output power versus wavelength for CF diameter of 100 µm and fixed length.

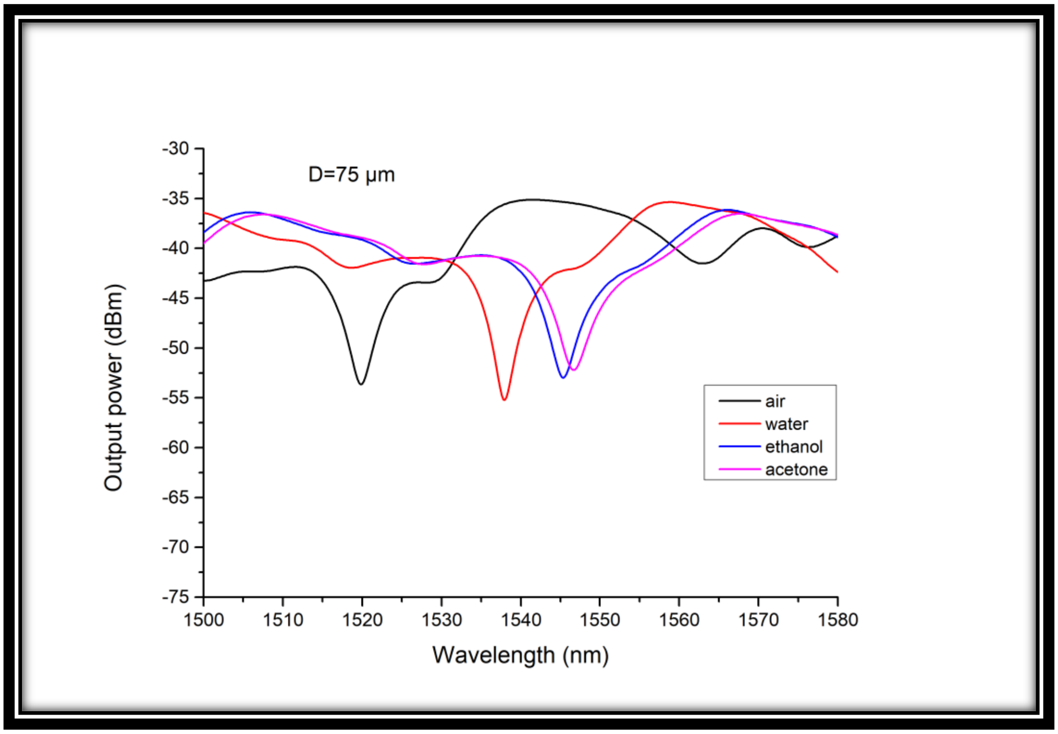

Figure: (3.11): The output power versus wavelength for CF diameter of 75 µm and fixed length.

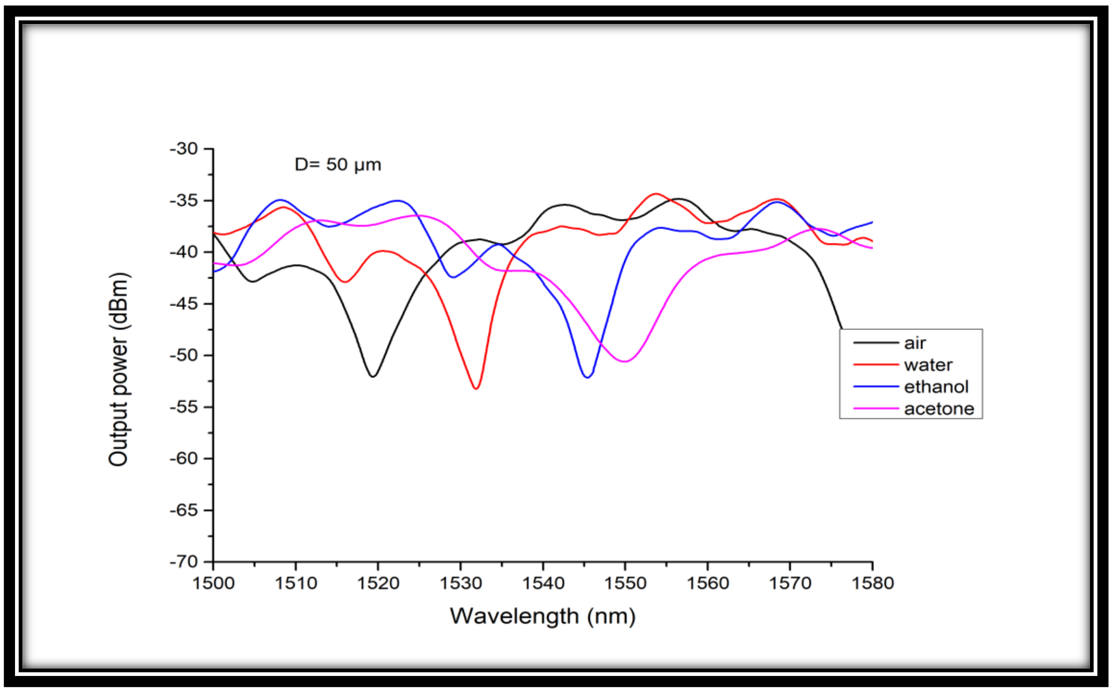

Figure: (3.12): The output power versus wavelength for CF diameter of 50 µm and fixed length.

Table 3.3: The sensitivity of RI sensor for different CF diameters with fixed length at 25 mm.

CF diameter (µm)	Wavelength shift (nm)	Sensitivity (nm/ RIU)
100	20.2	396.07
75	26.8	525.4
50	54	1058

3.5.3 RI Sensor for Fixed CF Length of 30 mm with Different Diameters:

3.5.3.1 Etched CF Diameter of RI Sensor

After preparing the fixed CF length of 30 mm in the SCS structure, the CF diameter has been reduced for the values (100, 75 and 50) µm. A different fluids with different refractive indices have been shown in figures (3.13, 3.14 and 3.15) where the colored lines in the transmission spectrum of black, red, blue and purple represents the refractive indices of air, deionized water, ethanol and acetone ,respectively.

The transmission spectrum had a maximum wavelength shifts of (14.4, 18.7 and 23.4) nm for acetone and the sensitivities of RI sensor are (282.35, 366.6 and 458.8) nm/RIU respectively.

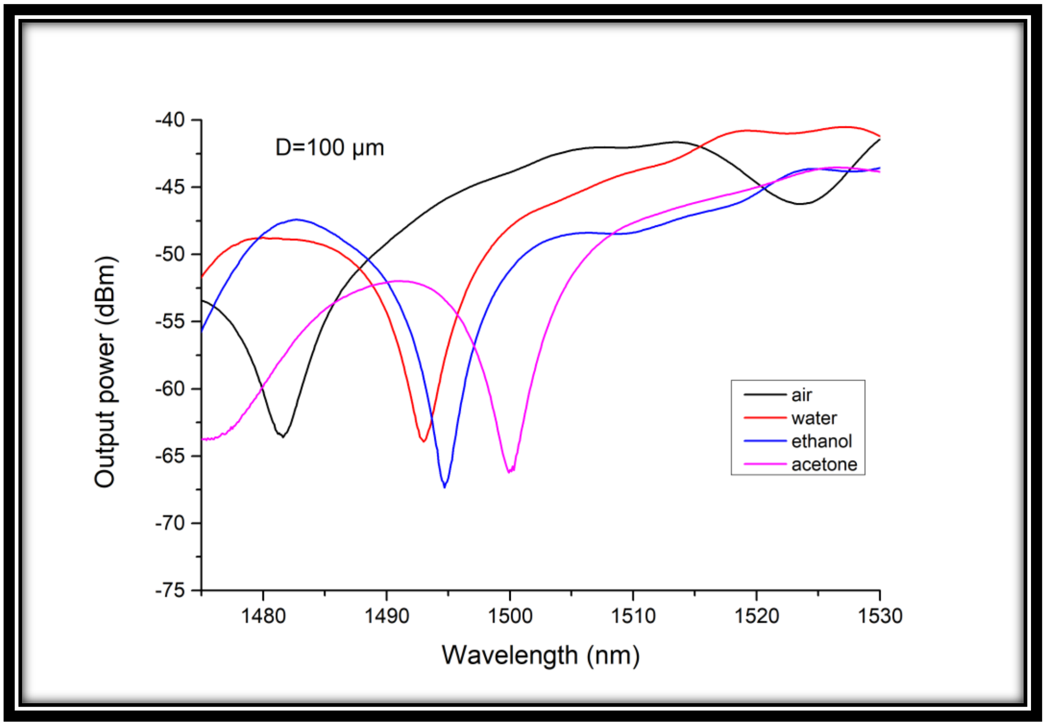

Figure (3.13): The output power versus wavelength for CF diameter of 100 µm and fixed length.

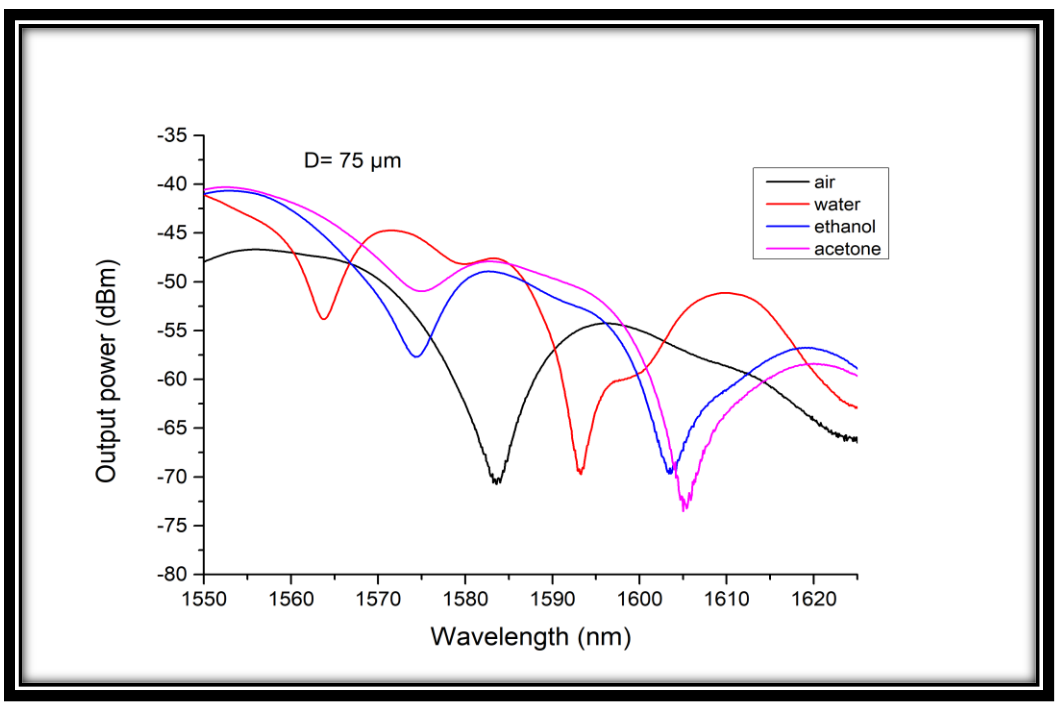

Figure (3.14): The output power versus wavelength for CF diameter of 75 µm and fixed length.

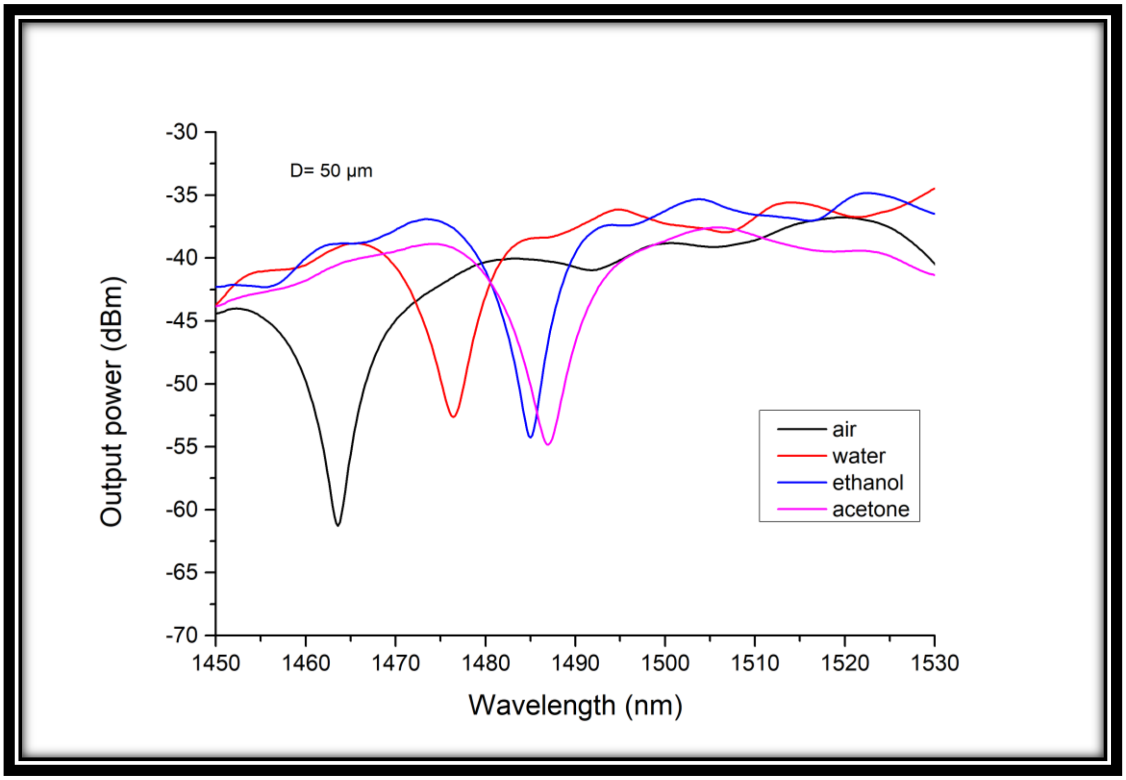

Figure (3.15): The output power versus wavelength for CF diameter of 50 µm and fixed length.

Table 3.4: The sensitivity of RI sensor for different CF diameters with fixed length at 30 mm.

CF diameter (µm)	Wavelength shift (nm)	Sensitivity (nm/ RIU)
100	14.4	282.35
75	18.7	366.6
50	23.4	458.8

3.6 The Influence of the CF Diameter on the Sensitivity

Reducing the CF diameter effected on the sensor sensitivity for each fixed CF on the SCS structure. From figures (3.7, 3.8, 3.9, 3.10, 3.11, 3.12, 3.13, 3.14 and 3.15), increasing the refractive indices from 1 for air to 1.351 for acetone leads to move the dip wavelength toward the red shift. The relation between the varied diameter of CF with wavelength shifts for each fixed length of the CF (20, 25 and 30) mm can be seen in figures (3.16, 3.17 and 3.18) respectively.

When the diameter of the CF reduced from 125 μm to 50 μm with the fixed CF length of 20 mm, the sensitivity of RI sensor increases from 255 nm/RIU to 780.3 nm/RIU.

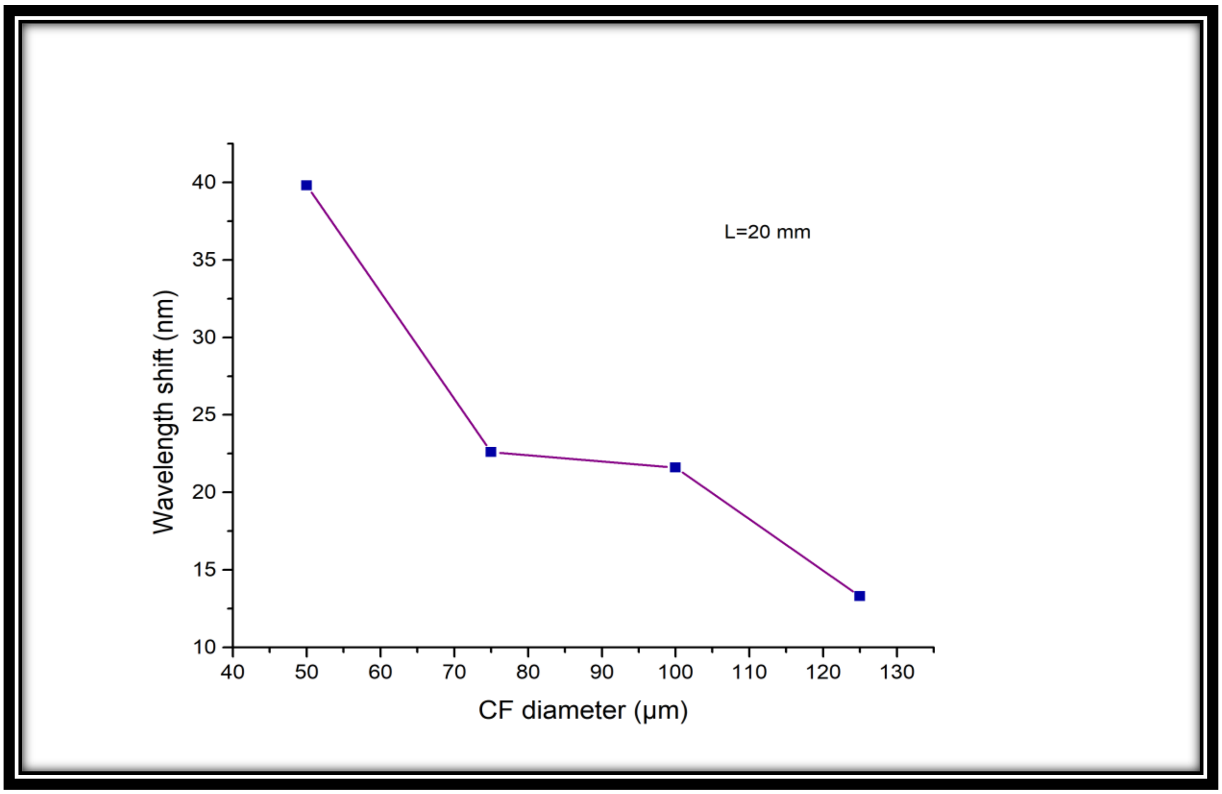

Figure (3.16): The wavelength shift (nm) as a function of CF diameter with fixed length of 20 mm.

For the CF fixed length of 25 mm with decreased CF diameter from 125μm to 50 μm, the sensor sensitivity rises from 266.6 nm/RIU to 1058 nm/RIU.

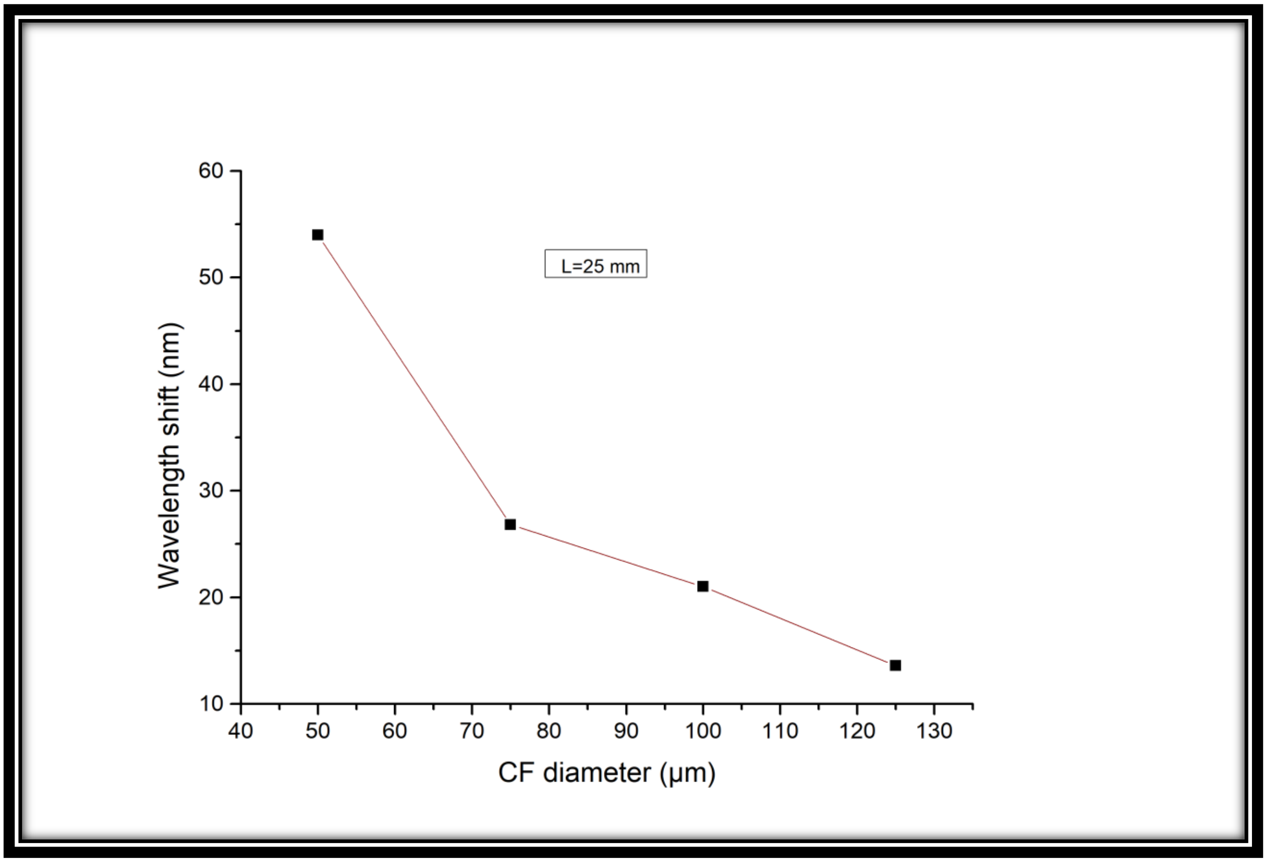

Figure 3.17: The wavelength shift (nm) as a function of CF diameter with fixed CF length of 25 mm.

For the third CF fixed length of 30 mm with decreased CF diameter from 125 μm to 50 μm, the RI sensor sensitivity increases from 245 nm/RIU to 458.8 nm/RIU.

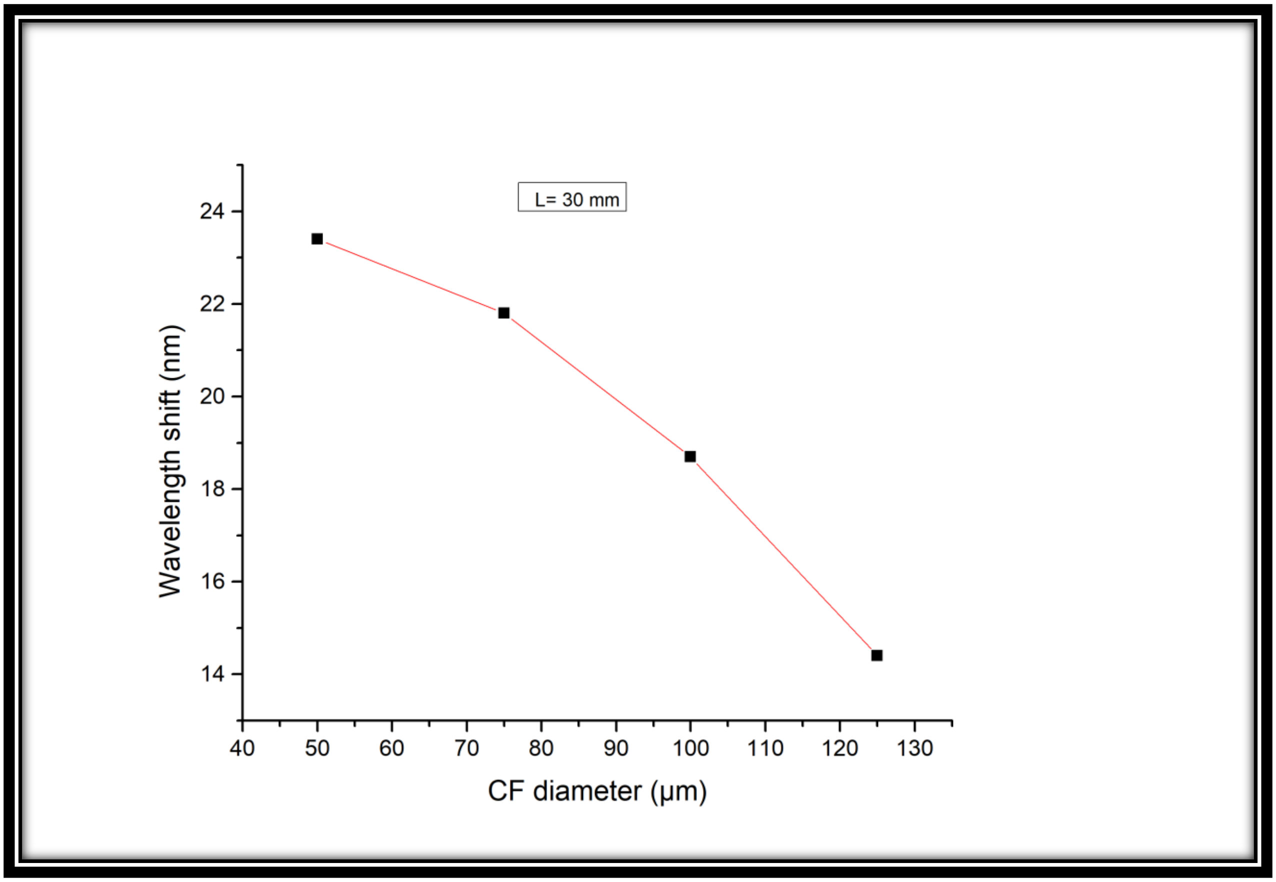

Figure (3.18): The wavelength shift (nm) as a function of CF diameter with CF fixed length of 30 mm.

The stimulated evanescent signals will interact with the surrounding RI and initiate the variation in output spectrum. Besides it can be observed that when the RI rises with the reduction of CF diameter, the transmission spectra shifted to longer wavelength (red- shift). This shifting in wavelength will lead to increases the sensitivity of the RI sensor.

3.7 The SCS Concentration Sensor

Sodium chloride is an iconic compound also known as salt with chemical formula NaCl. It has a similar ratio of ions 1:1 (sodium: chloride) and shaped as solid, clear crystal. Sodium chloride dissolved very well in water and the ions of NaCl crystal will separate to create the solution. It used in wide range of industrial applications.

3.7.1 The 20 mm SCS Concentration Sensor

Different concentrations of the NaCl solution were prepared and tested using the SCS structure with CF length of 20 mm and varies diameters. Figures (3.19, 3.20, 3.21 and 3.22) represents the transmission spectrum for diameters of (125, 100, 75 and 50) µm respectively, where the black line refers to air while the other colors are refer to NaCl solution concentrations ranged from 0% to 25% by 5 % step. The wavelength shifts for different CF diameters with fixed length of 20 mm and maximum sensitivities for the 25 % concentration can be noticed in Tables (3.5, 3.6, 3.7 and 3.8).

Table (3.5): The wavelength shifts (nm) and the maximum sensitivities for CF fixed length at diameter 125 µm.

Concentration (%)	Wavelength shift (nm)	Sensitivity (nm/RIU)
0	11	220
5	11.8	236
10	12.8	256
15	13.8	276
20	15	300
25	16	320

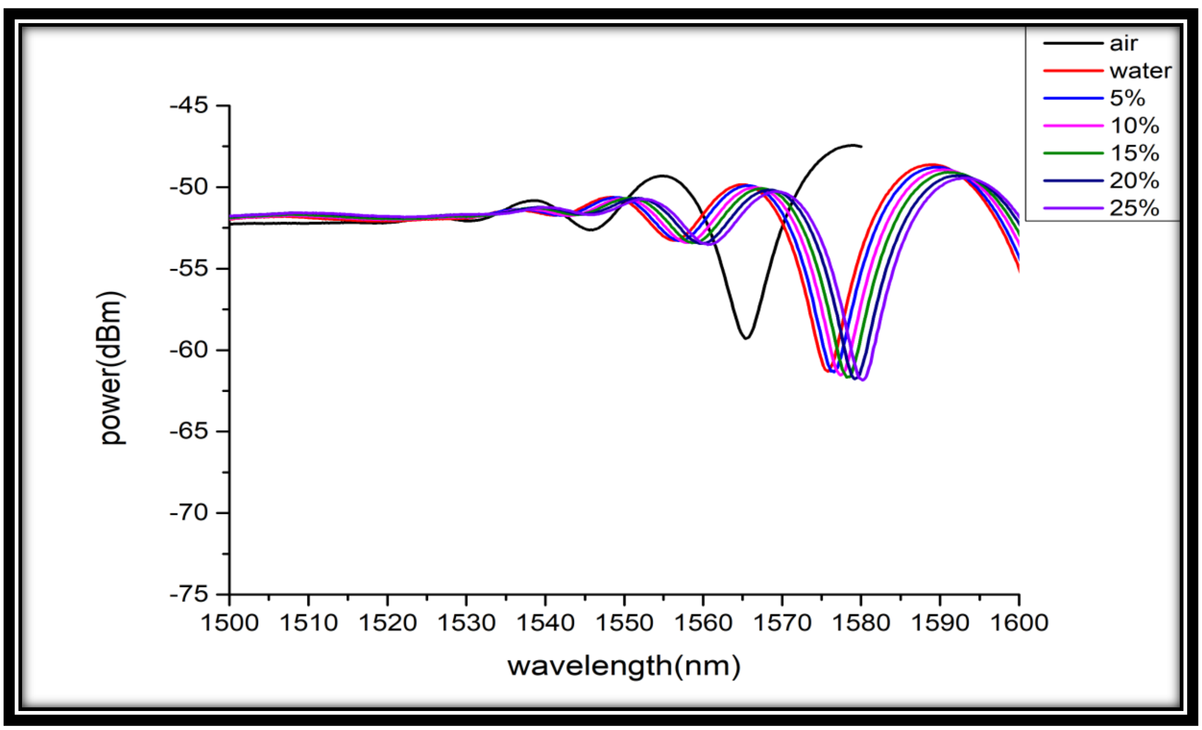

Figure (3.19): The transmission spectrum of CF length 20 mm and CF diameter 125 µm.

Table (3.6): The wavelength shifts (nm) and the maximum sensitivities for CF fixed length at diameter 100 μm.

Concentration (%)	Wavelength shift (nm)	Sensitivity (nm/ RIU)
0	12.8	256
5	13.8	276
10	14.8	296
15	16	320
20	17	340
25	18.4	368

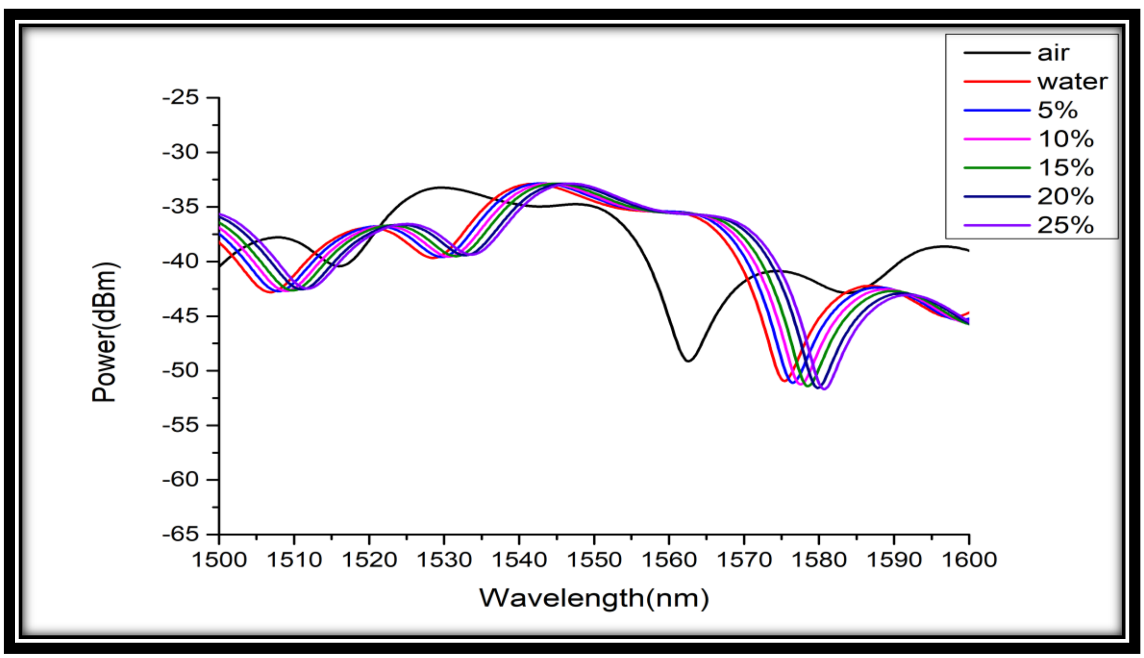

Figure (3.20): The transmission spectrum of CF length 20 mm and CF diameter 100 μm.

Table (3.7): The wavelength shifts (nm) and the maximum sensitivities for CF fixed length at diameter 75 μm.

Concentration (%)	Wavelength shift (nm)	Sensitivity (nm/ RIU)
0	15.6	312
5	17.2	344
10	18.2	364
15	19.8	396
20	21	420
25	22.6	452

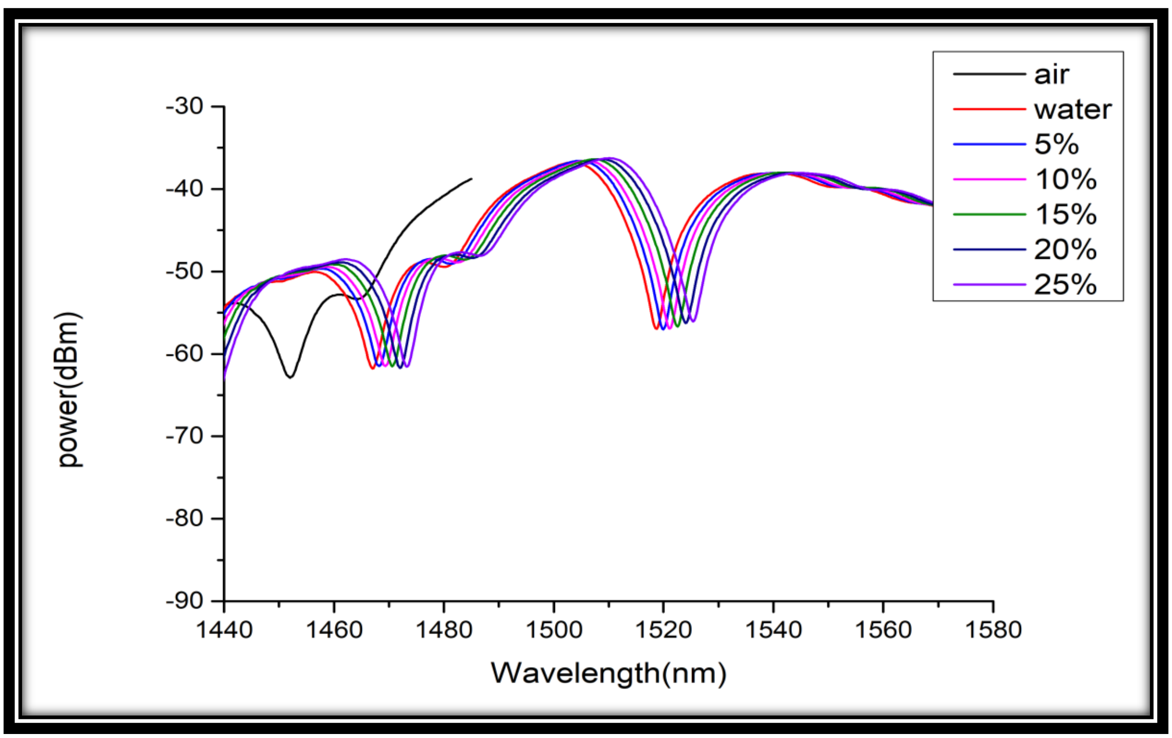

Figure (3.21): The transmission spectrum of CF length 20 mm and CF diameter 75 μm.

Table (3.8): The wavelength shifts (nm) and the maximum sensitivities for CF fixed length at diameter 50 µm.

Concentration (%)	Wavelength shift (nm)	Sensitivity (nm/ RIU)
0	27.6	552
5	30.2	604
10	32.2	644
15	34.2	684
20	37	740
25	39	780

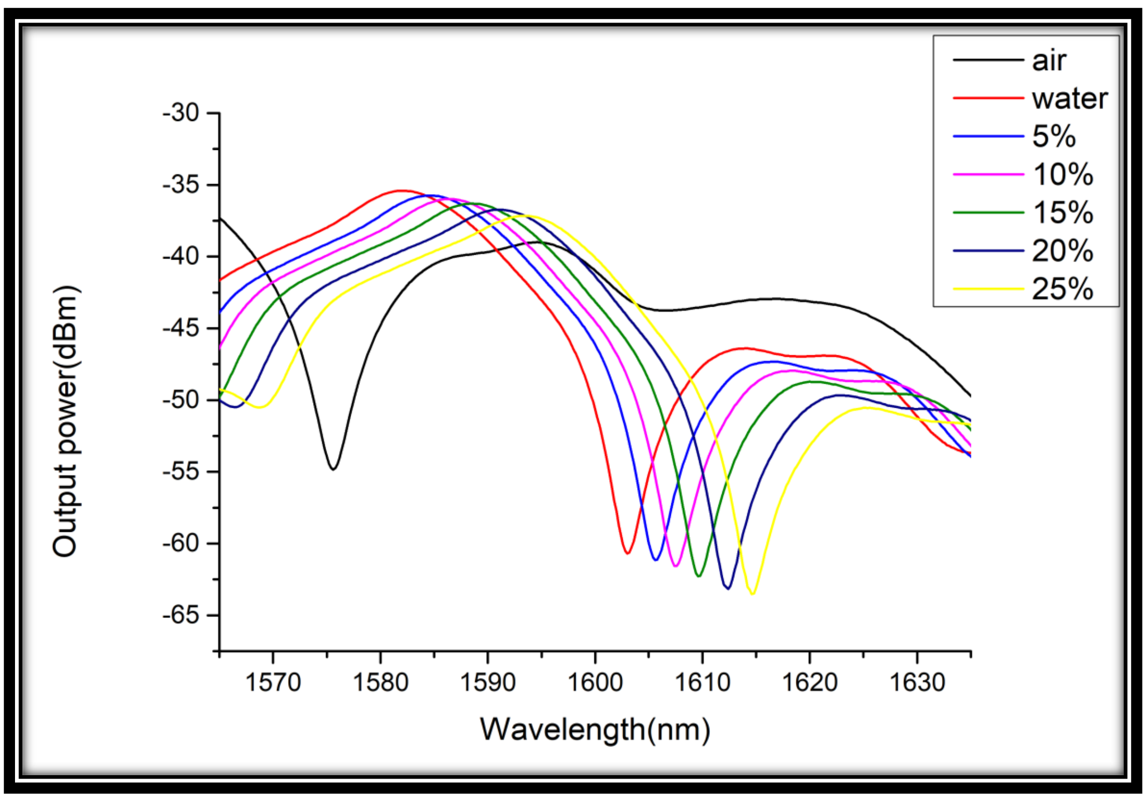

Figure (3.22): The transmission spectrum of CF length 20 mm and CF diameter 50 µm.

3.7.2 The 25 mm SCS Concentration Sensor

Different concentrations of the NaCl solution were prepared and tested using the SCS structure with CF length of 25 mm and varies diameters. Figures (3.23, 3.24, 3.25 and 3.26) represents the transmission spectrum for diameters of (125, 100, 75 and 50) µm respectively, where the black line refers to air while the other colors are refer to NaCl solution concentrations ranged from 0% to 25% by 5 % step. The wavelength shifts for different CF diameters with fixed length of 25 mm and maximum sensitivities for the 25 % concentration can be noticed in Tables (3.9, 3.10, 3.11 and 3.12).

Table (3.9): The wavelength shifts (nm) and the maximum sensitivities for CF fixed length at diameter 125 µm.

Concentration (%)	Wavelength shift (nm)	Sensitivity (nm/RIU)
0	9.4	188
5	10.2	204
10	10.8	216
15	12.2	244
20	12.8	256
25	13.4	268

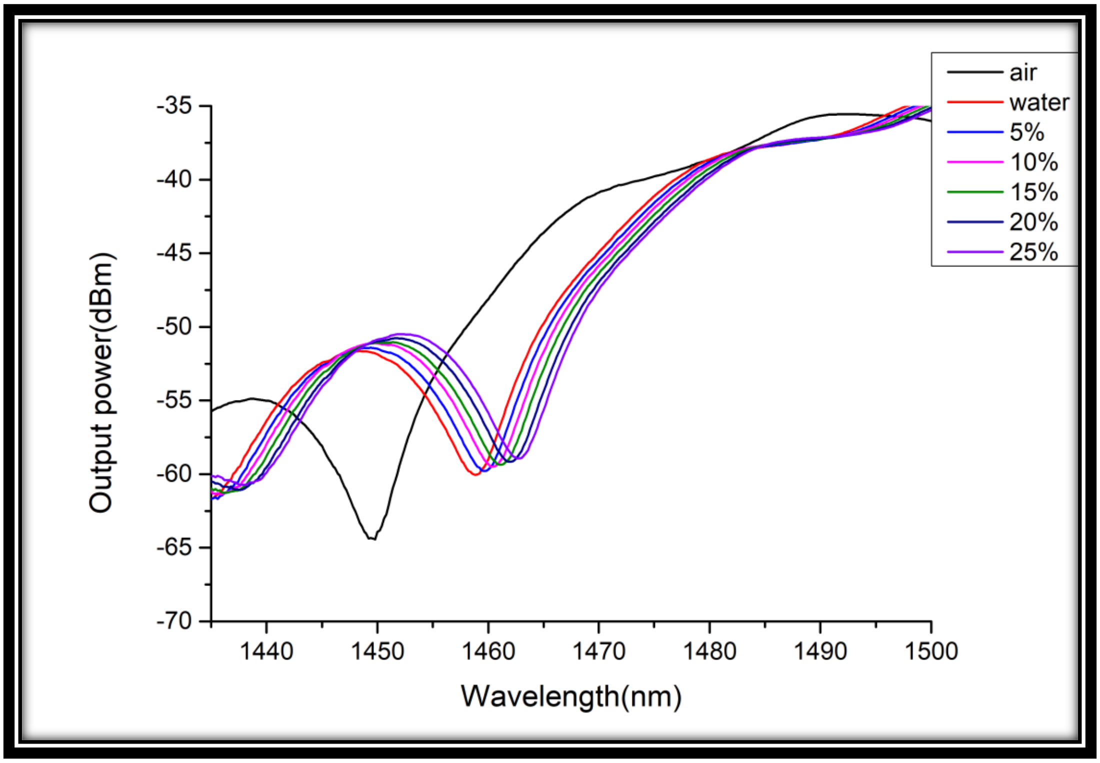

Figure (3.23): The transmission spectrum of CF length 25 mm and CF diameter 125 µm.

Table (3.10): The wavelength shifts (nm) and the maximum sensitivities for CF fixed length at diameter 100 µm.

Concentration (%)	Wavelength shift (nm)	Sensitivity (nm/ RIU)
0	13.8	276
5	15.3	306
10	15.6	312
15	16.9	338
20	18.1	362
25	19.1	382

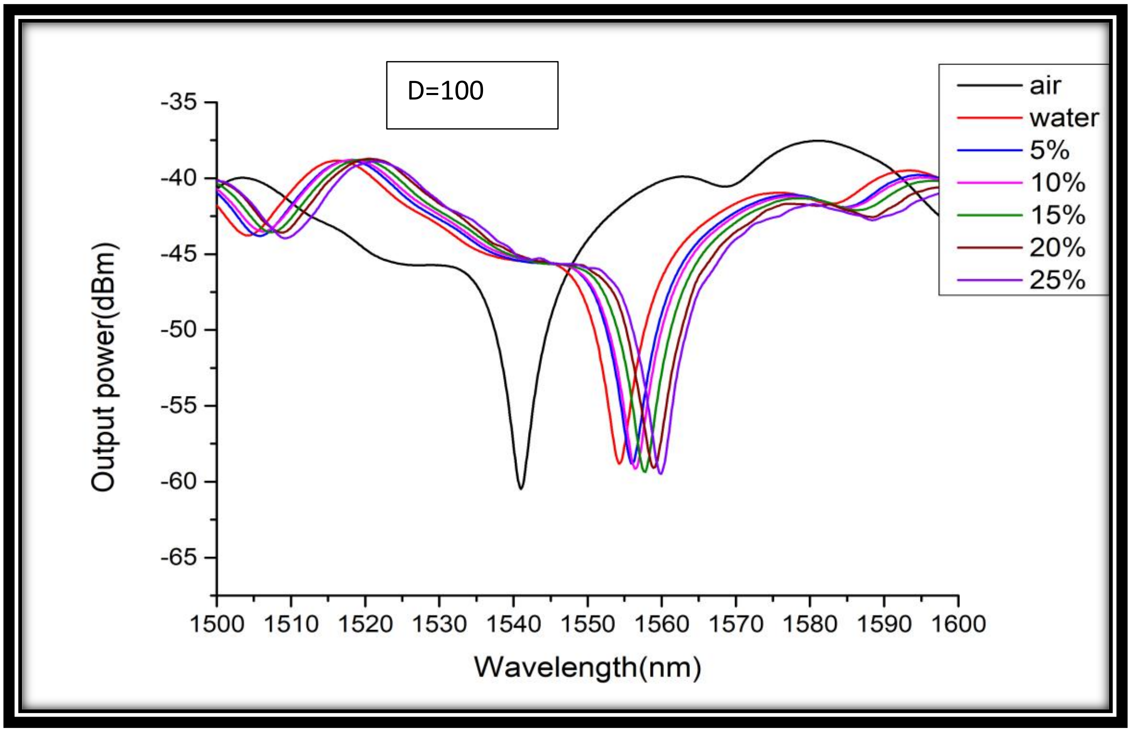

Figure (3.24): The transmission spectrum of CF length 25 mm and CF diameter 100 µm.

Table (3.11): The wavelength shifts (nm) and the maximum sensitivities for CF fixed length at diameter 75 µm.

Concentration (%)	Wavelength shift (nm)	Sensitivity (nm/ RIU)
0	17.4	348
5	19.2	384
10	21.2	424
15	22.6	452
20	24	480
25	25.4	508

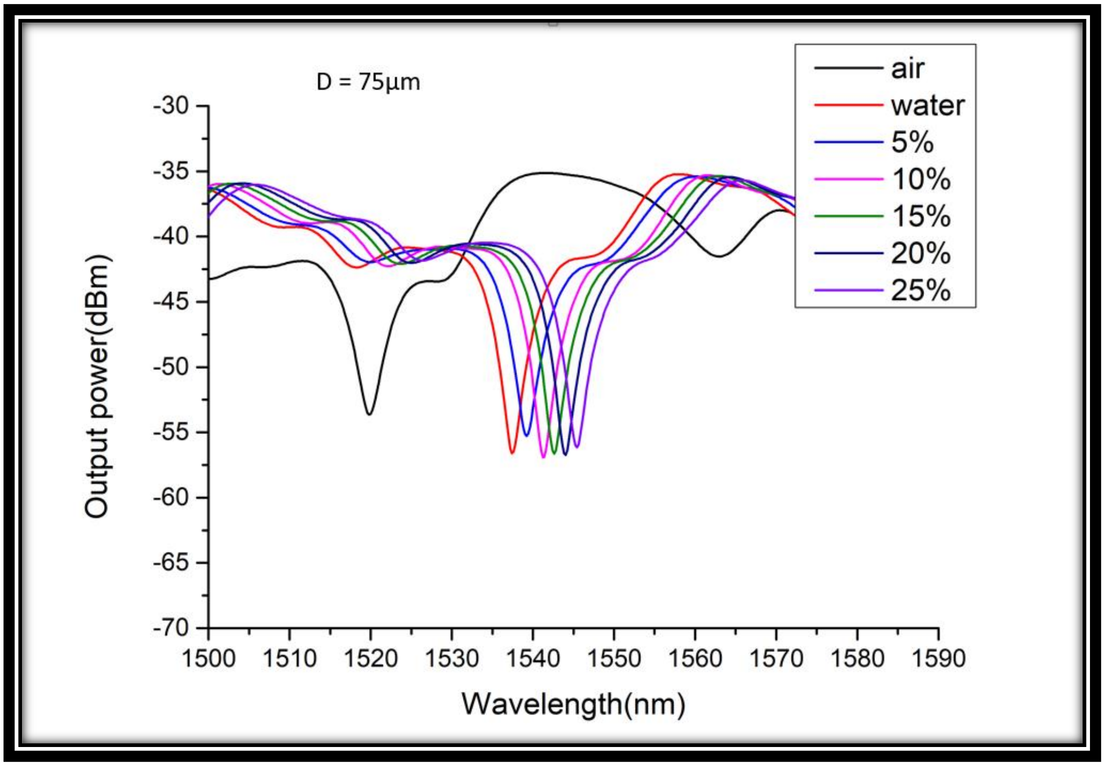

Figure (3.25): The transmission spectrum of CF length 25 mm and CF diameter 75 µm.

Table (3.12): The wavelength shifts (nm) and the maximum sensitivities for CF fixed length at diameter 50 µm.

Concentration (%)	Wavelength shift (nm)	Sensitivity (nm/ RIU)
0	35	700
5	38.6	772
10	41.4	828
15	43.8	876
20	47.6	952
25	50.6	1012

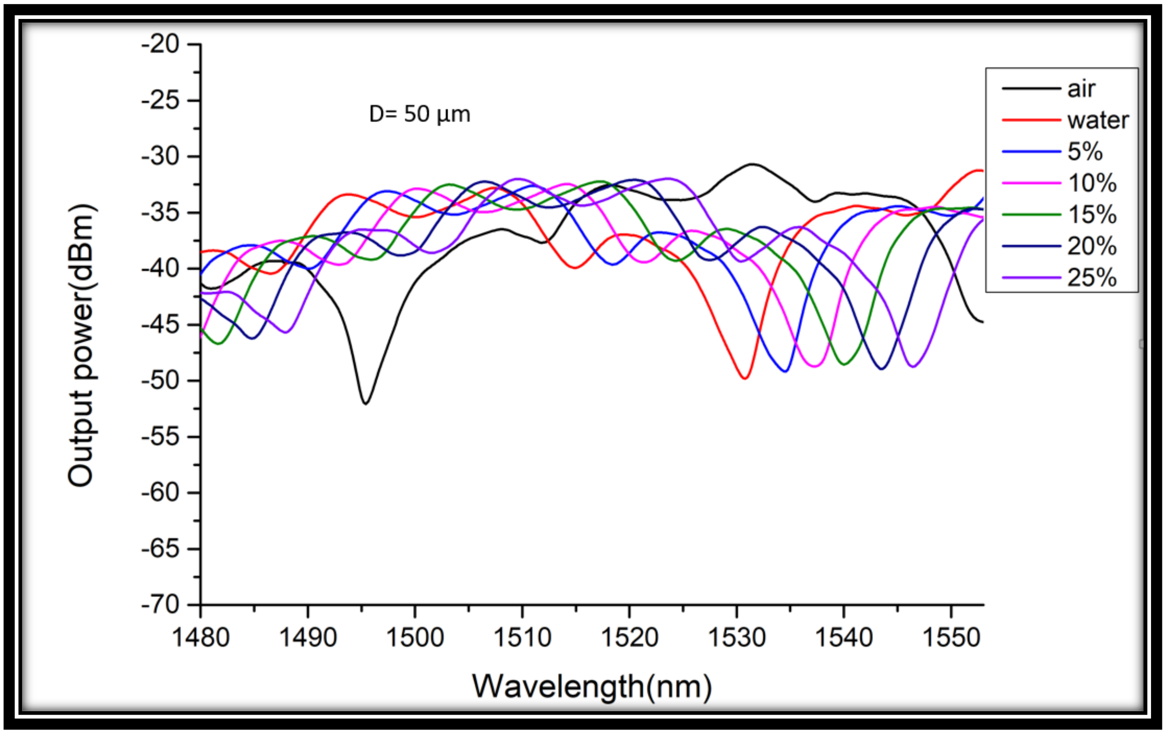

Figure (3.26): The transmission spectrum of CF length 25 mm and CF diameter 50 µm.

3.7.3 The 30 mm SCS Concentration Sensor

Different concentrations of the NaCl solution were prepared and tested using the SCS structure with CF length of 30 mm and varies diameters. Figures (3.27, 3.28, 3.29 and 3.30) represents the transmission spectrum for diameters of (125, 100, 75 and 50) µm respectively, where the black line refers to air while the other colors are refer to NaCl solution concentrations ranged from 0% to 25% by 5 % step. The wavelength shifts for different CF diameters with fixed length of 30 mm and maximum sensitivities for the 25 % concentration can be noticed in Tables (3.12, 3.13, 3.14 and 3.15).

Table (3.13): The wavelength shifts (nm) and the maximum sensitivities for CF fixed length at diameter 125 μm.

Concentration (%)	Wavelength shift (nm)	Sensitivity (nm/RIU)
0	6.7	134
5	6.9	138
10	7.8	156
15	9.1	182
20	9.3	186
25	9.8	196

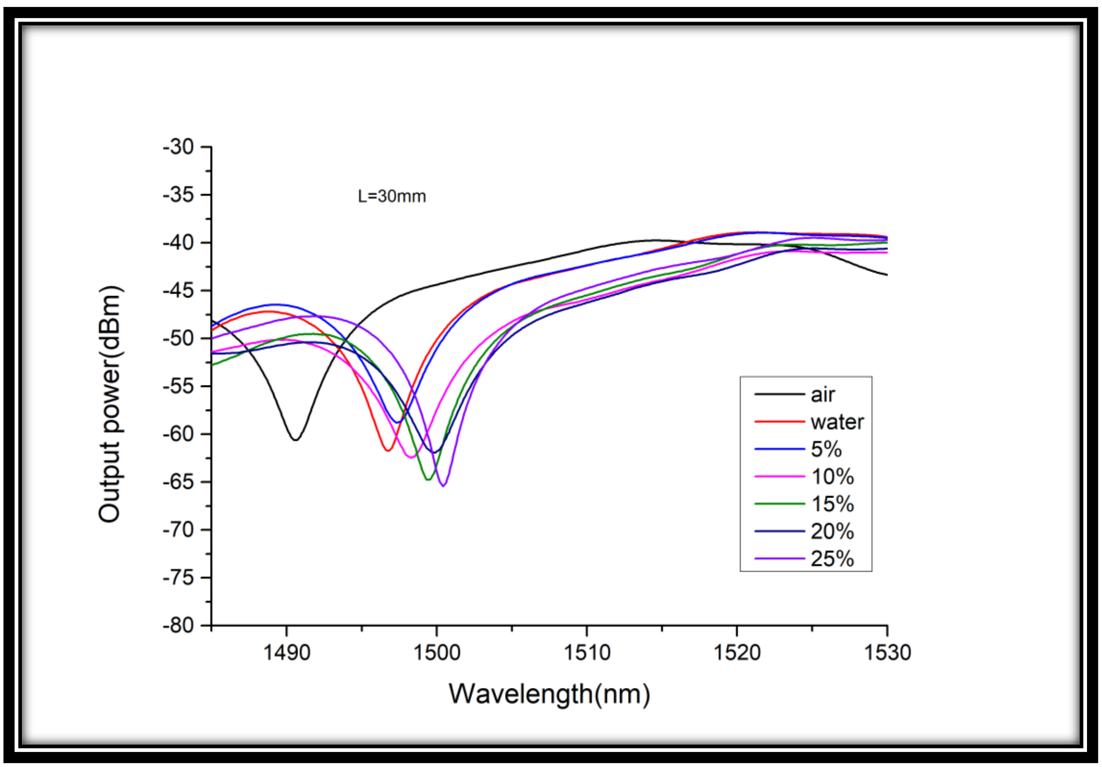

Figure (3.27): The transmission spectrum of CF length 30 mm and CF diameter 125 μm.

Table (3.14): The wavelength shifts (nm) and the maximum sensitivities for CF fixed length at diameter 100 µm.

Concentration (%)	Wavelength shift (nm)	Sensitivity (nm/ RIU)
0	10.5	210
5	11.2	224
10	12.1	242
15	13.1	262
20	14	280
25	14.9	298

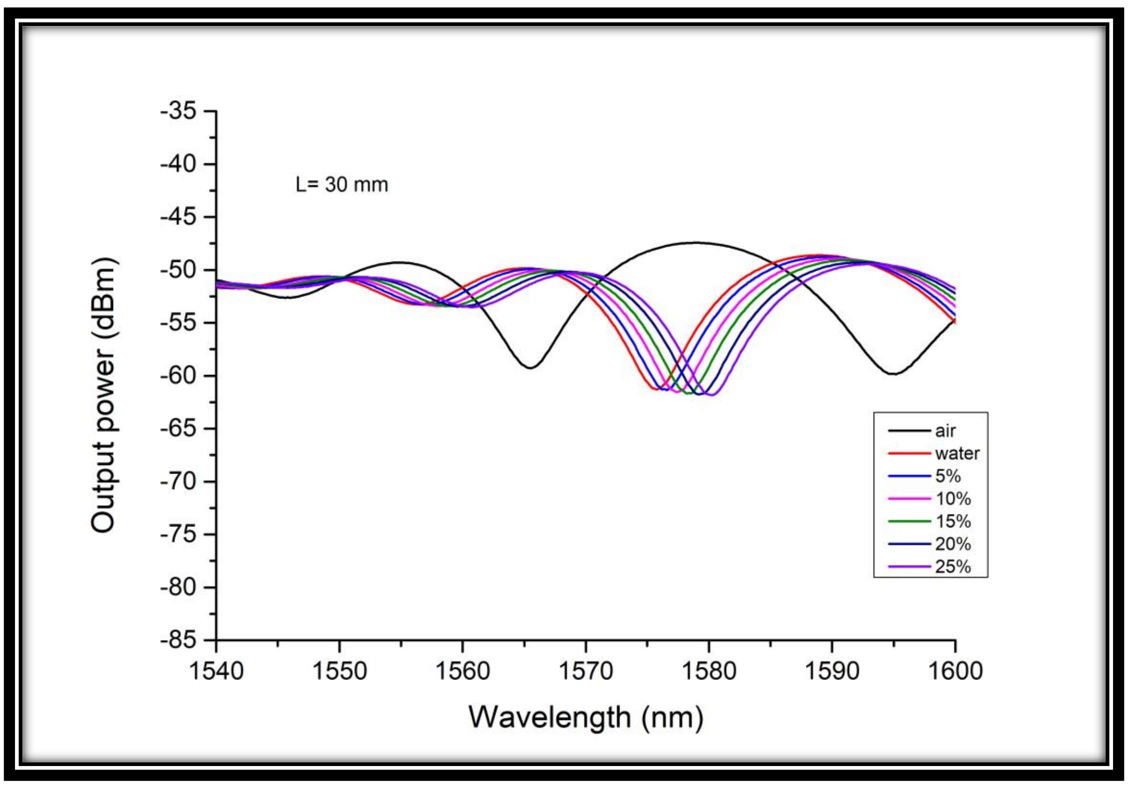

Figure (3.28): The transmission spectrum of CF length 30 mm and CF diameter 100 µm.

Table (3.15): The wavelength shifts (nm) and the maximum sensitivities for CF fixed length at diameter 75 µm.

Concentration (%)	Wavelength shift (nm)	Sensitivity (nm/ RIU)
0	11.6	232
5	15.4	308
10	15.8	316
15	17.3	346
20	19.5	390
25	21.6	432

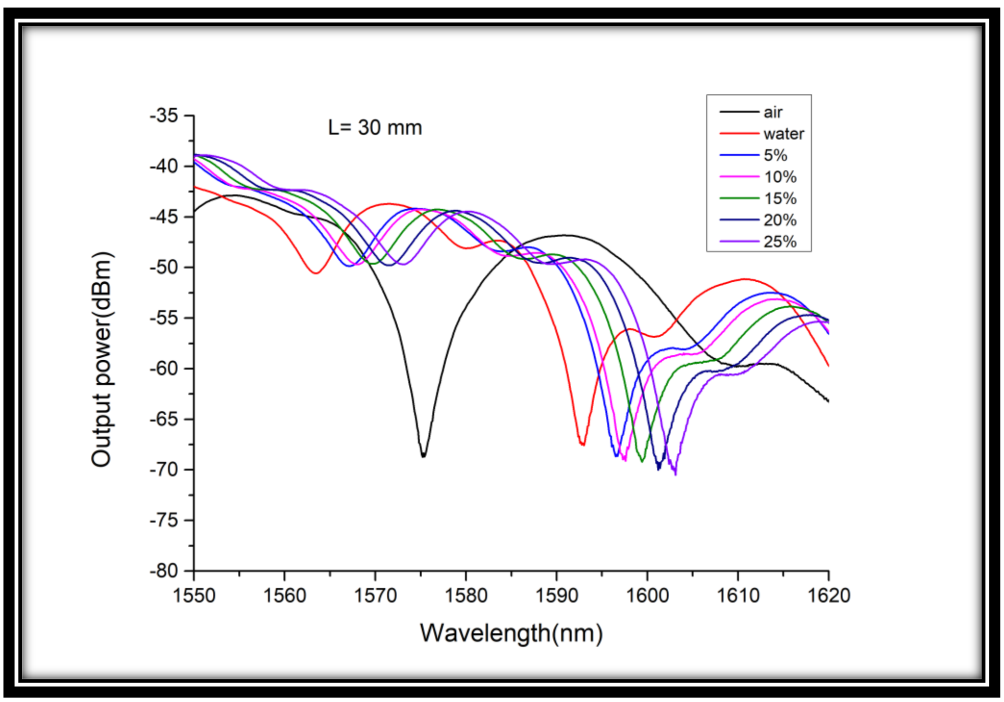

Figure (3.29): The transmission spectrum of CF length 30 mm and CF diameter 75 µm.

Table (3.16): The wavelength shifts (nm) and the maximum sensitivities for CF fixed length at diameter 50 µm.

Concentration (%)	Wavelength shift (nm)	Sensitivity (nm/RIU)
0	17.5	350
5	21.2	424
10	22.3	446
15	24.1	482
20	26.1	522
25	27.6	552

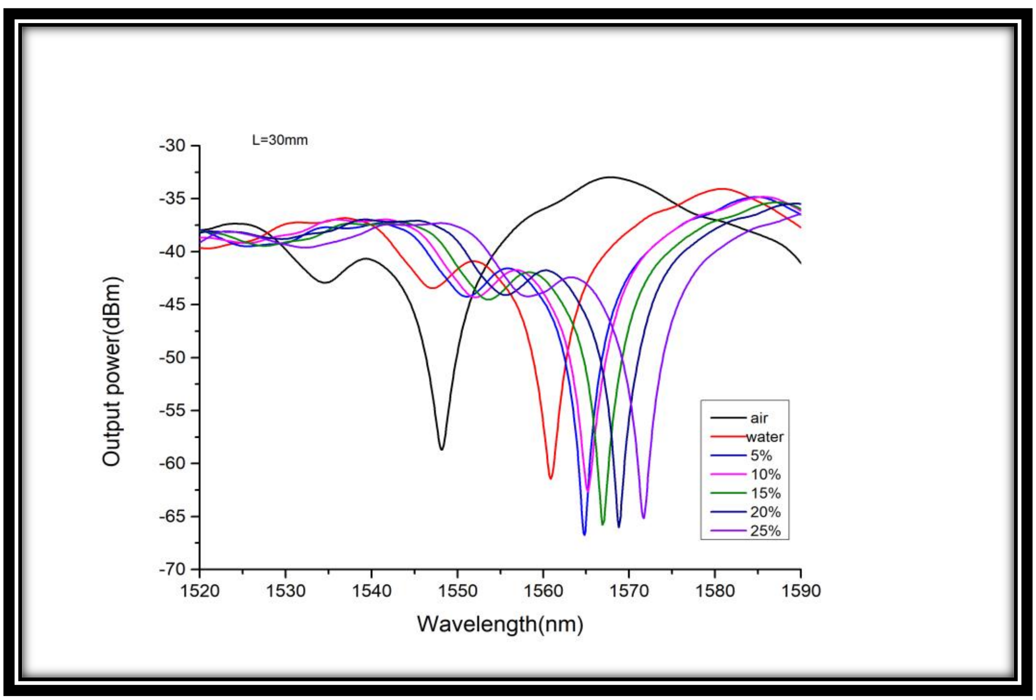

Figure (3.30): The transmission spectrum of CF length 30 mm and CF diameter 50 µm.

3.8 The Relation between the Concentration and the CF Diameter of SCS-MZI Concentration Sensor

3.8.1 For 20 mm CF Length of SCS Concentration Sensor

The wavelength dip shifted to longer wavelength when the concentration of NaCl solution increases (0-25) % for SCS structure with CF length of 20 mm and diameters of 125, 100, 75 and 50 μm. Figure (3.31) clarified the relation between NaCl solution concentrations and the wavelength shift.

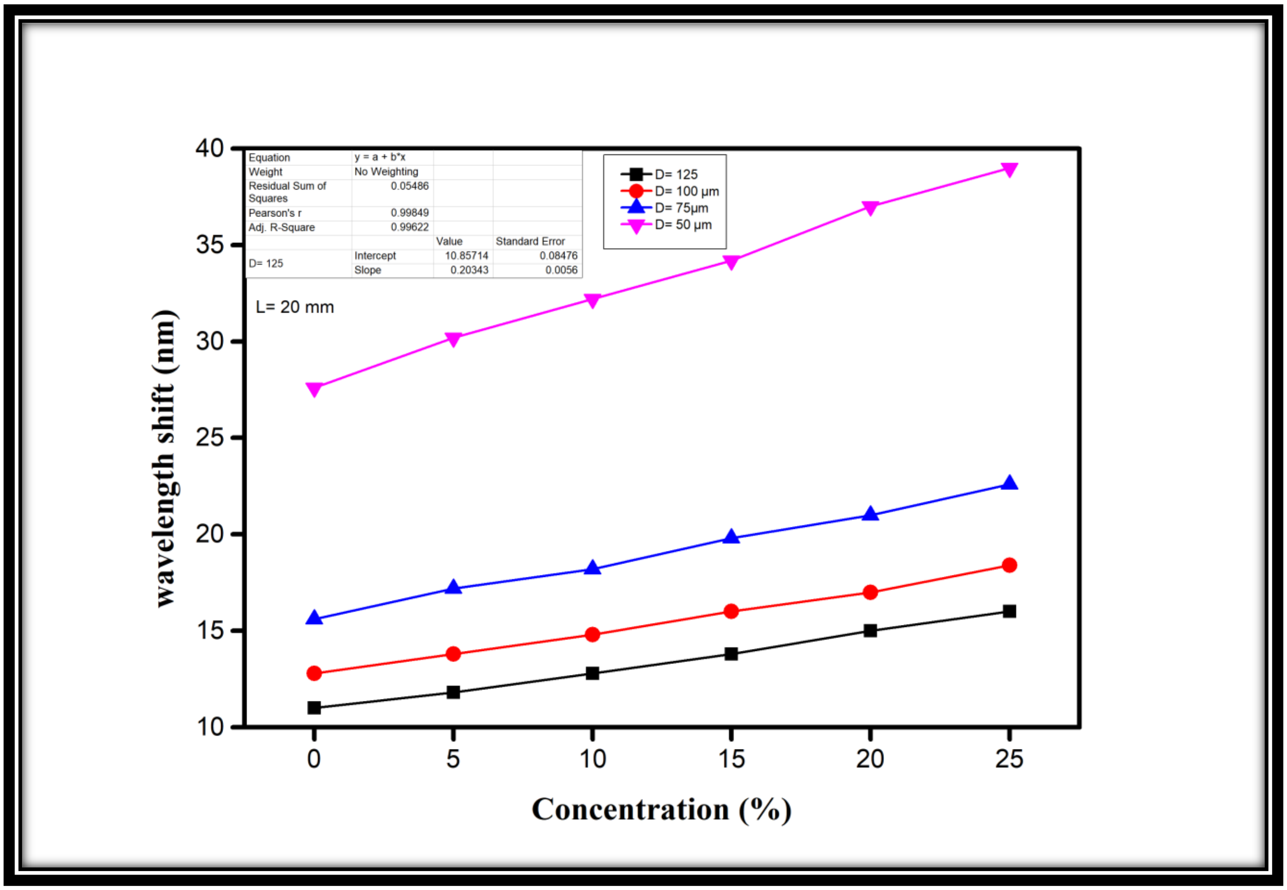

Figure (3.31): The concentration of NaCl solution versus the wavelength shift for CF diameters and 20 mm CF length.

3.8.2 For 25 mm CF Length of SCS-MZI Concentration Sensor

The wavelength dip rises to longer wavelength shift when the concentration of NaCl solution increases (0-25) % for SCS structure with CF length of 25 mm and diameters of 125, 100, 75 and 50 μm. Figure (3.32) clarified the relation between NaCl solution concentrations and the wavelength shift.

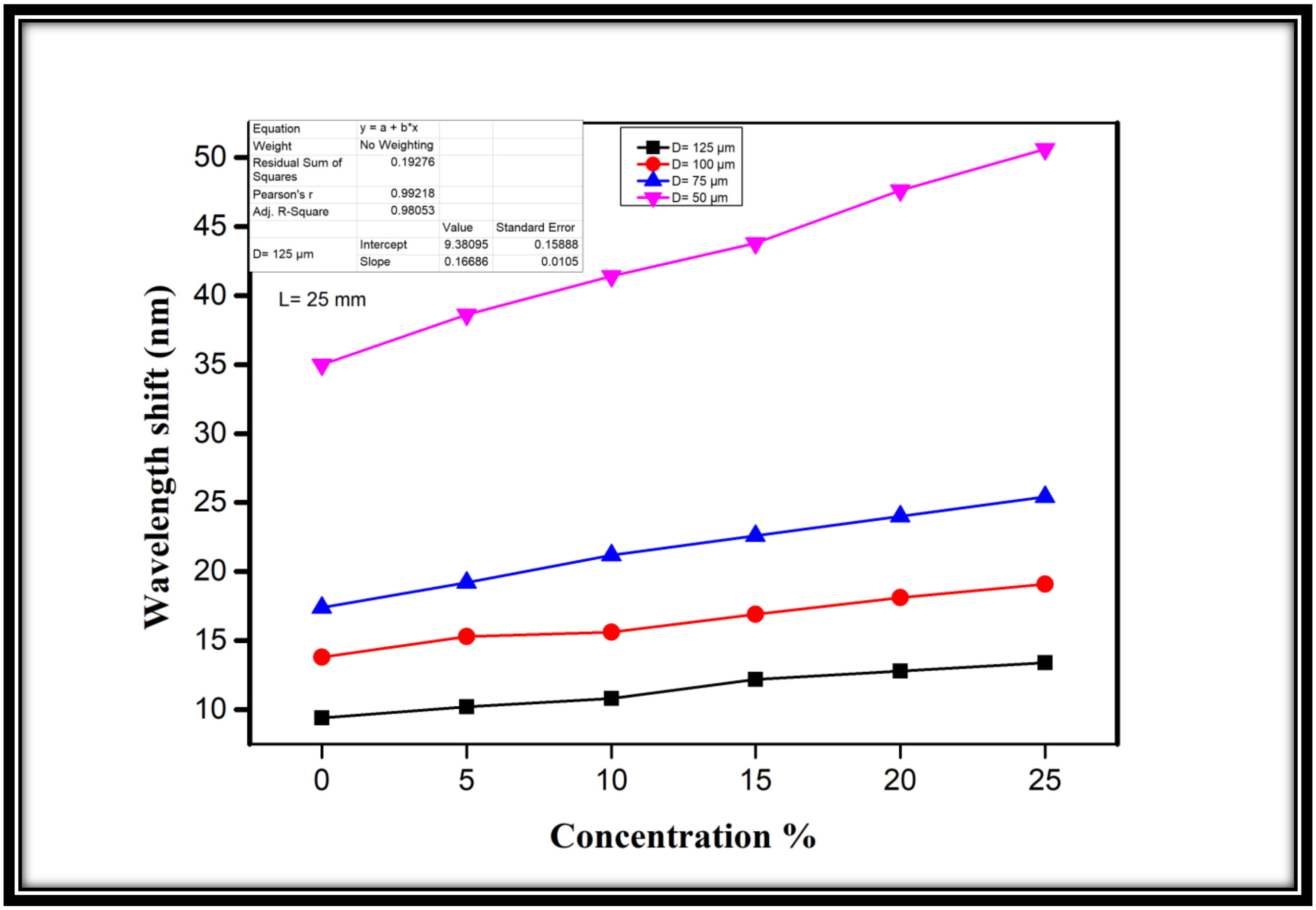

Figure (3.32): The concentration of NaCl solution versus the wavelength shift for CF diameters and 25 mm CF length.

3.8.3 For 30 mm CF Length of SCS-MZI Concentration Sensor

The wavelength dip rises to longer wavelength shift when the concentration of NaCl solution increases (0-25) % for SCS structure with CF length of 30 mm and diameters of 125, 100, 75 and 50 µm. Figure (3.33) clarified the relation between NaCl solution concentrations and the wavelength shift.

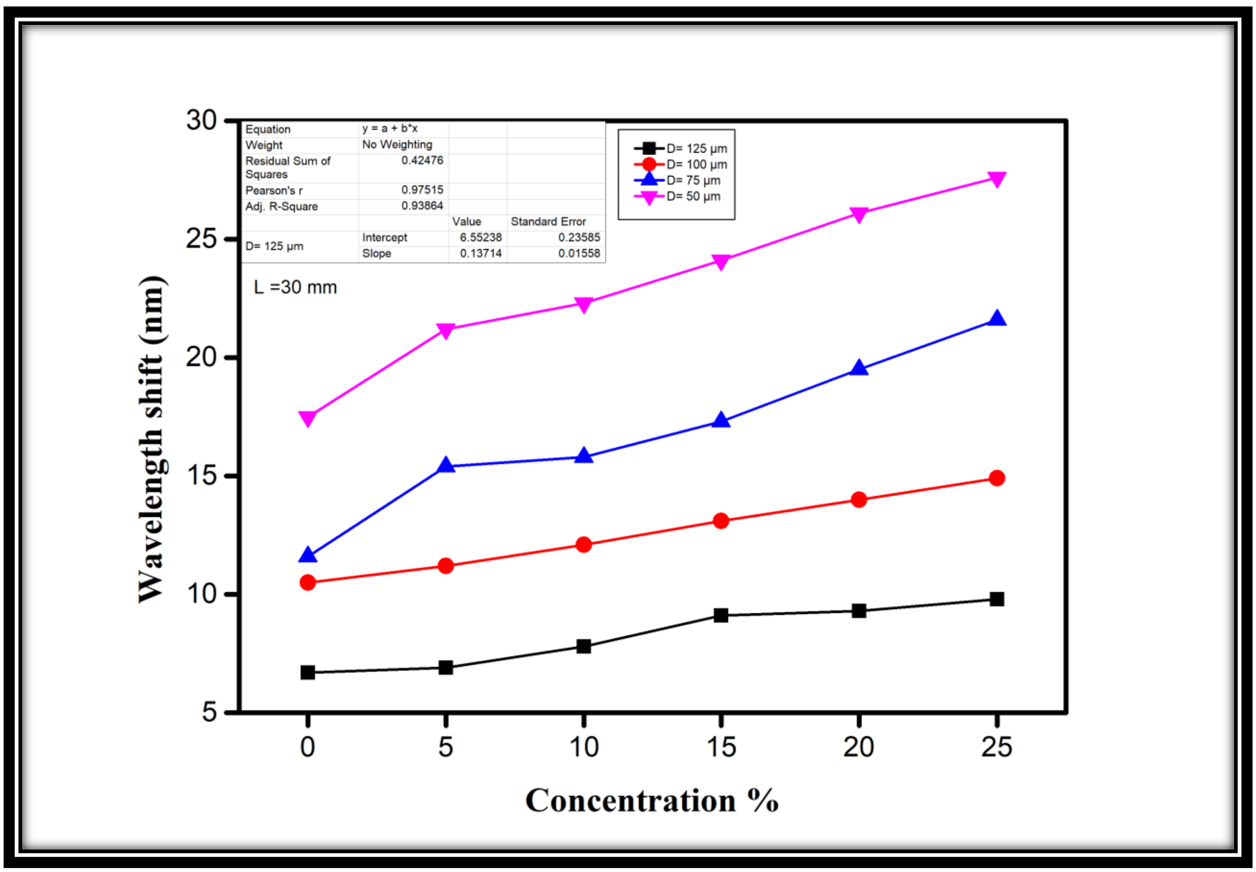

Figure (3.33): The concentration of NaCl solution versus the wavelength shift for CF diameters and 30 mm CF length.

3.9: Effect of the Concentration on the Sensitivity

A three varies lengths of CF (20, 25 and 30) mm were used to build a refractive index sensor to study the changes of NaCl solution concentration/ RI with the wavelength shift variations as shown in figures (3.18- 3.29). It is obvious that when the concentration / RI increases, the wavelength dip heads to red shift. From these results, it can be observed that the greatest RI sensitivity of the proposed configuration was with CF of 50 µm diameter and 25 mm length. It represents the minimum portion of the light transmitting via the fiber that induces highest evanescent fields, causing in an improvement of optical interaction between the surrounding RI light and the fiber-guided. Corresponding to MMI principle, the length and diameter of CF would influence the output spectra and too there is an optimum length for every diameter to preserve the self-imaging and reduction the losses. From Figure 3.34, the linear fitting coefficient (R^2) is 0.998 for SCS fiber configuration with 50 µm diameter and 25 mm length, which exhibits an excellent RI sensing features of the SCS-based sensor.

Additionally, it can be observed that the transmission response of the proposed SCS sensor reveals a significant red-shift, this due to the lower refractive indices of the surrounding material which the surrounding ambient function as a cladding layer.

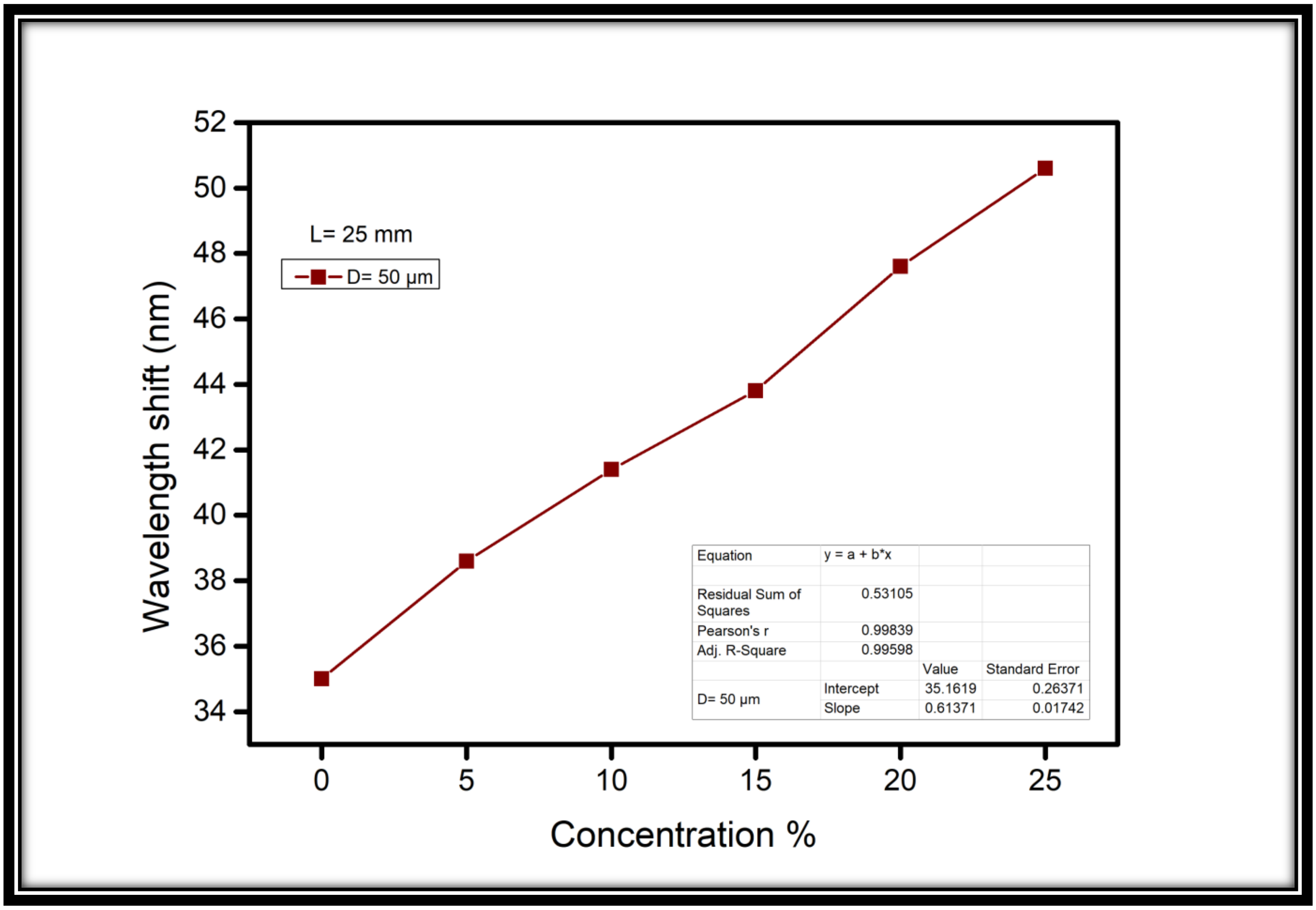

Figure (3.34): The wavelength shift versus the concentration of NaCl solution for CF diameter 50 μm and 25 mm CF length.

Conclusion

In this work, an all-optical fiber RI sensor based on multimode interference has been proposed and experimentally demonstrated. SCS configuration comprises of CF section which represent the sensing area spliced between two small pieces of SMF. A various diameters of CF of 125, 100, 75 and 50 µm with three different lengths 20, 25 and 30 mm have been employed as a sensing area to substitute the traditional MMF. The effect of CF diameter variation on the sensor performance has been examined. Chemical etching process was used to tune the CF diameter from 125 to 50 µm. The surrounding medium of the SCS structure were fluids (air, deionized water, ethanol and acetone) with refractive indices (1.33- 1.38) and NaCl solution with concentrations (0- 25) %. For the variation of CF length, a slight difference was noticed in wavelength shift for CF diameter of 125 µm. when the concentration/ RI increases, the obtained wavelength rises toward the red shift.

The experimental results of the SCS configuration encompassed of the etched CF at 50 µm diameter with a CF length of 25 mm exhibited a maximum wavelength shift was about 50.6 nm and the greatest sensitivity is about 1012 nm/RIU for NaCl solution when the concentration is 25%. While for the refractive index of 1.38, a maximum wavelength shift is 56 nm and the greatest sensitivity is 1058 nm/RIU for fluids. The SCS structure has attractive benefits such as low cost, high measurement sensitivity, simple structure, and fast response. As a result for these advantages it can be considered a suitable choice for sensing applications. This work and the works of other researchers were compared based on the structure, diameters, refractive indices and the sensitivities as shown in table 3.17.

Table 3.17: comparison between the sensitivities of this work and other researchers.

researcher	Sensor structure	Diameter (µm)	RI range	Sensitivity (nm/RIU)	Reference
Yong Zhao et al.	SMF-MMF-SMF	40	1.33-1.4	286.2	81
Min shao et al.	SMF-TF-MMF-SMF	90	1.33-1.42	148.27	82
Haifeng DU et al.	SMF-PCF-SMF	112 91	1.33-1.38 1.33-1.38	211.53 359.37	76
Saif A. et al.	SMF-CF-SMF	60	1.33-1.38	340.85	75
This work	SMF-CF-SMF	50	1.33-1.38	1012	

Future work

1. Fabrication and implementation a refractive index sensor based on different type of optical fiber such as twin core fiber.

2. Replace the NaCl solution with another chemical solutions had a different concentrations and refractive indices.

3. Using a different splicing technique such as offset splicing or tapering splicing.

References

[1]: Vaz, A., Barroca, N., Ribeiro, M., Pereira, A. and Frazão, O.,. “Optical fiber humidity sensor based on polyvinylidene fluoride Fabry–Perot”. *IEEE Photonics Technology Letters*, *31*(7), pp.549-552, 2019.

[2]: Zhao, L., Jiang, L., Wang, S., Xiao, H., Lu, Y. and Tsai, H.L., “A high-quality Mach-Zehnder interferometer fiber sensor by femtosecond laser one-step processing”. *Sensors*, *11*(1), pp.54-61, 2011.

[3]: Zheng, S., Zhu, Y. and Krishnaswamy, S., April. “Nanofilm-coated long-period fiber grating humidity sensors for corrosion detection in structural health monitoring”. In Nondestructive Characterization for Composite Materials, Aerospace Engineering, Civil Infrastructure, and Homeland Security 2011 (Vol. 7983, p. 79831A). International Society for Optics and Photonics, 2011.

[4]: Kraft, M., Jakusch, M., Karlowatz, M., Katzir, A. and Mizaikoff, B., “ New frontiers for mid-infrared sensors: Towards deep sea monitoring with a submarine FT-IR sensor system”. Applied spectroscopy, 57(6), pp.591-599, 2003.

[5]: Kumagai, T., Soekawa, H., Yuhara, T., Kajioka, H., Oho, S. and Sonobe, H., March. “Fiber optic gyroscopes for vehicle navigation systems”. In Fiber Optic and Laser Sensors XI (Vol. 2070, pp. 181-191). International Society for Optics and Photonics, 1994.

[6]: Zhao, Y., Lei, M., Liu, S.X. and Zhao, Q., “Smart hydrogel-based optical fiber SPR sensor for pH measurements”. Sensors and Actuators B: Chemical, 261, pp.226-232, 2018.

[7]: Yang, W., Zhang, S., Geng, T., Li, L., Li, G., Gong, Y., Zhang, K., Tong, C., Lu, C., Sun, W. and Yuan, L., "High Sensitivity Refractometer Based on a Tapered-Single Mode-No Core-Single Mode Fiber Structure". Sensors, 19(7), p.1722, 2019.

[8]: Du, H., Sun, X., Hu, Y., Dong, X. and Zhou, J., "High sensitive refractive index sensor based on cladding etched photonic crystal fiber Mach-Zehnder interferometer". Photonic Sensors, 9(2), pp.126-134, 2019.

[9]: Novais, S., Ferreira, C.I., Ferreira, M.S. and Pinto, J.L., "Glucose Measurements with Optical Fiber Sensor based on Coreless Silica Fiber". In Optical Fiber Sensors (p. ThE2). Optical Society of America, September, 2018.

[10]: Zanoon, N.I., "The Phenomenon of Total Internal Reflection and Acceleration of Light in Fiber Optics". International Journal of Computer Applications, 975, p.8887, 2014.

[11]: Aslian, A., Honarvar Shakibaei Asli, B., Tan, C.J., Adikan, F.R.M. and Toloei, A., "Design and analysis of an optical coupler for concentrated solar light using optical fibers in residential buildings". International Journal of Photoenergy, 2016.

[12]: Olusola, A., Oluwadare, S., Olaojoyetan, E. and Christianah, M., "Fibre Broadband Development in Nigeria: A Catalyst to Economic Growth and Social Development". Global Advanced Research Journal of Engineering, Technology and Innovation, 3(5), pp.83-99, 2014.

[13]: Rekha, M., Singh, M. and Raj, B., "SINGLE MODE FIBER STANDARDS": A REVIEW, 2008.

[14]: J. M. Senior, "Optical Fiber Communications principles and practice", 3rd edition, Prentice Hall, ch2, pp. 26-28, (2009).

[15]: S. M. Dhanshetti, "Advance Module Communication System and Specilized Module Dth And Other Communication System," India, 2015.

[16]: Wang, Q., Farrell, G. and Yan, W., 2008. Investigation on single-mode–multimode–single-mode fiber structure. *Journal of Lightwave Technology*, *26*(5), pp.512-519.

[17]: Choi, M., Humar, M., Kim, S. and Yun, S.H., “Step- index optical fiber made of biocompatible hydrogels”. Advanced Materials, 27(27), pp.4081-4086, 2015.

[18]: Agrawal, G.P., “Fiber-optic communication systems” (Vol. 222). John Wiley & Sons, 2012.

[19]: Arumugam, M., Optical fiber communication—An overview. Pramana, 57(5-6), pp.849-869, 2001.

[20]: Gong, Q. and Hu, X., Photonic crystals: “principles and applications”. Jenny Stanford Publishing, 2014.

[21]: Yasin, M., Harun, S.W. and Arof, H. eds., “Recent progress in optical fiber research”. BoD–Books on Demand, 2012.

[22]: Han, Y.G., Kim, G., Lee, K., Lee, S.B., Jeong, C.H., Oh, C.H. and Kang, H.J., “Bending sensitivity of long-period fiber gratings inscribed in holey fibers depending on an axial rotation angle”. Optics express, 15(20), pp.12866-12871, 2007.

[23]: Saitoh, K., Koshiba, M., Hasegawa, T. and Sasaoka, E., Chromatic dispersion control in photonic crystal fibers: application to ultra-flattened dispersion. Optics express, 11(8), pp.843-852, 2003.

[24]: Abobaker, A.M., Olupitan, S., Aphale, S.S., Nakkeeran, K., Senthilnathan, K. and Babu, P.R., Dynamics of 850 nm optical pulses upon compression in a tapered photonic crystal fiber. In 2011 Saudi International Electronics, Communications and Photonics Conference (SIECPC) (pp. 1-4). IEEE, April, 2011.

[25]: Khaleel, W.A. and Al-Janabi, A.H.M., High-sensitivity sucrose erbium-doped fiber ring laser sensor. Optical Engineering, 56(2), p.026116, 2017.

[26]: https://www.thorlabs.com/newgrouppage9.cfm?objectgroup_id=9979 2017.

[27]: Zanoon, N.I., The Phenomenon of Total Internal Reflection and Acceleration of Light in Fiber Optics. International Journal of Computer Applications, 975, p.8887, 2014.

[28]: Okoshi, T., Optical fibers. Elsevier, 2012.

[29]: Obianuju, O.N. and Chong, K.K., High acceptance angle optical fiber based daylighting system using two-stage reflective non-imaging dish concentrator. Energy Procedia, 105, pp.498-504, 2017.

[30]: Born, M. and Wolf, E., Principles of Optics, 7th (expanded) edition. United Kingdom: Press Syndicate of the University of Cambridge, 461, 1999.

[31]: Mhdi, B.R., Aljbar, N.A., Kadhim, S.A., Hamode, J.F., Khalid, A.H., Ali, S.M. and Mhdi, A.S., Design Ammonia Gas Detection System by Using Optical Fiber Sensor. IJECCE, 4(4), pp.1330-1333, 2013.

[32]: Senior, J.M. and Jamro, M.Y., Optical fiber communications: principles and practice. Pearson Education, 2009.

[33]: Li, Y., Liu, Z. and Jian, S., Multimode interference refractive index sensor based on coreless fiber. Photonic Sensors, 4(1), pp.21-27, 2014.

[34]: Huang, S.C., Lin, W.W., Tsai, M.T. and Chen, M.H., 2007. Fiber optic in-line distributed sensor for detection and localization of the pipeline leaks. *Sensors and Actuators A: Physical*, *135*(2), pp.570-579.

[35]: Ballato, J. and Dragic, P., 2016. Glass: the carrier of light- a brief history of optical fiber. *International Journal of Applied Glass Science*, *7*(4), pp.413-422.

[36]: Choi, S., Eom, T.J., Yu, J.W., Lee, B.H. and Oh, K., 2002. Novel all-fiber bandpass filter based on hollow optical fiber. *IEEE Photonics Technology Letters*, *14*(12), pp.1701-1703.

[37]: Aslian, A., Honarvar Shakibaei Asli, B., Tan, C.J., Adikan, F.R.M. and Toloei, A., 2016. Design and analysis of an optical coupler for concentrated solar light using optical fibers in residential buildings. *International Journal of Photoenergy*, *2016*.

[38]: Agrawal, G.P., 2012. *Fiber-optic communication systems* (Vol. 222). John Wiley & Sons.

[39]: Lohmann, A.W., Knuppertz, H. and Jahns, J., Fractional Montgomery effect: a self-imaging phenomenon. JOSA A, 22(8), pp.1500-1508, 2005.

[40]: Aneesh, R. and Khijwania, S.K., Titanium dioxide nanoparticle based optical fiber humidity sensor with linear response and enhanced sensitivity. Applied optics, 51(12), pp.2164-2171, 2012.

[41]: Rivero, P.J., Urrutia, A., Goicoechea, J. and Arregui, F.J., Optical fiber humidity sensors based on Localized Surface Plasmon Resonance (LSPR) and Lossy-mode resonance (LMR) in overlays loaded with silver nanoparticles. Sensors and Actuators B: Chemical, 173, pp.244-249, 2012.

[42]: Lee, B.H., Kim, Y.H., Park, K.S., Eom, J.B., Kim, M.J., Rho, B.S. and Choi, H.Y., Interferometric fiber optic sensors. sensors, 12(3), pp.2467-2486, 2012.

[43]: Perales, M., Wu, C.L. and Yang, M.H., Merits of a hybrid fluorescent fiber sensor and power over fiber partial discharge detection solution. In Fiber Optic Sensors and Applications XV (Vol. 10654, p. 1065406). International Society for Optics and Photonics, May, 2018.

[44]: Lecler, S. and Meyrueis, P., Intrinsic optical fiber sensor. In Fiber Optic Sensors. IntechOpen, 2012.

[45]: Kwon, L., Long, K.D., Wan, Y., Yu, H. and Cunningham, B.T., Medical diagnostics with mobile devices: Comparison of intrinsic and extrinsic sensing. Biotechnology advances, 34(3), pp.291-304, 2016.

[46]: Kong, W., Zheng, Z., Wan, Y., Li, S. and Liu, J.,. High-sensitivity sensing based on intensity-interrogated Bloch surface wave sensors. Sensors and Actuators B: Chemical, 193, pp.467-471, 2014.

[47]: Singha, J. and Borah, R.J., Recent Advances in Microbend Sensors in Various Applications. 2013

[48]: De Acha, N., Elosúa, C., Corres, J.M. and Arregui, F.J.,. Fluorescent sensors for the detection of heavy metal ions in aqueous media. Sensors, 19(3), p.599, 2019.

[49]: Campanella, C.E., Cuccovillo, A., Campanella, C., Yurt, A. and Passaro, V.,. Fibre Bragg grating based strain sensors: review of technology and applications. Sensors, 18(9), p.3115, 2018.

[50]: Albert, J., Shao, L.Y. and Caucheteur, C., 2013. Tilted fiber Bragg grating sensors. *Laser & Photonics Reviews*, *7*(1), pp.83-108.

[51]: Udd, E.,. Overview of fiber optic sensors. In Fiber Optic Sensors (pp. 1-34). CRC Press, 2017.

[52]: Gholamzadeh, B. and Nabovati, H.,. Fiber optic sensors. World Academy of Science, Engineering and Technology, 42(3), pp.335-340, 2008.

[53]: Khan, H.,. Fabry-Pérot Interferometer: construction, calibration and development, 2015.

[54]: Sánchez-Soto, L.L., Monzón, J.J. and Leuchs, G.,. The many facets of the Fabry–Perot. European Journal of Physics, 37(6), p.064001, 2016.

[55]: Gribaev, A.I., Pavlishin, I.V., Stam, A.M., Idrisov, R.F., Varzhel, S.V. and Konnov, K.A.,. Laboratory setup for fiber Bragg gratings inscription based on Talbot interferometer. Optical and Quantum Electronics, 48(12), p.540, 2016.

[56]: MALLMANN, G., VOSS, K., RESINK, S. and BORREMAN, A.,, SMART MICROMACHINING, 2015.

[57]: Yoshino, H., Abbas, A., Kaminski, P.M., Smith, R., Walls, J.M. and Mansfield, D.,. Measurement of thin film interfacial surface roughness by coherence scanning interferometry. Journal of Applied Physics, 121(10), p.105303, 2017.

[58]: Sun, L.P., Li, J., Jin, L., Ran, Y. and Guan, B.O.,. High-birefringence microfiber Sagnac interferometer based humidity sensor. Sensors and Actuators B: Chemical, 231, pp.696-700, 2016.

[59]: Singh, C. and Marshman, E.,. Developing an interactive tutorial on a Mach-Zehnder interferometer with single photons. arXiv preprint arXiv:1510.01319, 2015.

[60]: Lin, H.S., Raji, Y.M., Lim, J.H., Lim, S.K., Mokhtar, M.R. and Yusoff, Z.,. Packaged in-line Mach–Zehnder interferometer for highly sensitive curvature and flexural strain sensing. Sensors and Actuators A: Physical, 250, pp.237-242, 2016.

[61]: Huerta-Mascotte, E., Sierra-Hernandez, J.M., Mata-Chavez, R.I., Jauregui-Vazquez, D., Castillo-Guzman, A., Estudillo-Ayala, J.M., Guzman-Chavez, A.D. and Rojas-Laguna, R.,. A core-offset Mach Zehnder interferometer based on a non-zero dispersion-shifted fiber and its torsion sensing application. Sensors, 16(6), p.856, 2016.

[62]: Baumann, H., Pythoud, F., Blas, D., Sibiryakov, S., Eichenberger, A. and Klingelé, E.E.,. Experimental assessment of the speed of light perturbation in free-fall absolute gravimeters. Metrologia, 52(5), p.635, 2015.

[63]: Wang, J. and Dai, D.,. Highly sensitive Si nanowire-based optical sensor using a Mach–Zehnder interferometer coupled microring. Optics letters, 35(24), pp.4229-4231, 2010.

[64]: Yang, J., Jiang, L., Wang, S., Li, B., Wang, M., Xiao, H., Lu, Y. and Tsai, H.,. High sensitivity of taper-based Mach–Zehnder interferometer embedded in a thinned optical fiber for refractive index sensing. Applied optics, 50(28), pp.5503-5507, 2011.

[65]: Yang, J., Jiang, L., Wang, S., Chen, Q., Li, B. and Xiao, H.,. Highly sensitive refractive index optical fiber sensors fabricated by a femtosecond laser. IEEE photonics Journal, 3(6), pp.1189-1197, 2011.

[66]: Xue, L.L. and Yang, L.,. Sensitivity enhancement of RI sensor based on SMS fiber structure with high refractive index overlay. Journal of lightwave technology, 30(10), pp.1463-1469, 2012.

[67]: Lin, H.Y., Huang, C.H., Cheng, G.L., Chen, N.K. and Chui, H.C.,. Tapered optical fiber sensor based on localized surface plasmon resonance. Optics express, 20(19), pp.21693-21701, 2012.

[68]: Chen, C.H., Hsu, C.Y., Huang, P.H., Wang, J.N. and Wu, W.T., . Optical coupling structures of fiber-optic Mach-Zehnder interferometers using CO2 laser irradiation. International Journal of Antennas and Propagation, 2014.

[69]: Ortega-Mendoza, J.G., Padilla-Vivanco, A., Toxqui-Quitl, C., Zaca-Morán, P., Villegas-Hernández, D. and Chávez, F.,. Optical fiber sensor based on localized surface plasmon resonance using silver nanoparticles photodeposited on the optical fiber end. Sensors, 14(10), pp.18701-18710, 2014.

[70]: Liu, Z.K., Zhou, B., Zhang, Y., Wang, Z.J., Weng, H.M., Prabhakaran, D., Mo, S.K., Shen, Z.X., Fang, Z., Dai, X. and Hussain, Z.,. Discovery of a three-dimensional topological Dirac semimetal, Na3Bi. Science, 343(6173), pp.864-867, 2014.

[71]: Luo, H., Sun, Q., Xu, Z., Jia, W., Liu, D. and Zhang, L.,. Microfiber-based inline Mach–Zehnder interferometer for dual-parameter measurement. IEEE Photonics Journal, 7(2), pp.1-8, 2015.

[72]: Wang, Q., Kong, L., Dang, Y., Xia, F., Zhang, Y., Zhao, Y., Hu, H. and Li, J.,. High sensitivity refractive index sensor based on splicing points tapered SMF-PCF-SMF structure Mach-Zehnder mode interferometer. Sensors and Actuators B: Chemical, 225, pp.213-220, 2016.

[73]: Wang, Q., Wang, B.T., Kong, L.X. and Zhao, Y., . Comparative analyses of bi-tapered fiber Mach–Zehnder interferometer for refractive index sensing. IEEE Transactions on Instrumentation and Measurement, 66(9), pp.2483-2489, 2017.

[74]: N. A. Salman, "Photonic Crystal Fiber Interferometer Based on Refractive Index Sensor ", M.SC thesis, Institute of Laser for Postgraduate Studies, University of Baghdad, (2017).

[75]: Mohammed, S.A. and Al-Janabi, A.H.,. All Fiber Chemical Liquids Refractive Index Sensor Based on Multimode Interference. Iraqi Journal of Laser, 17(A), pp.33-39, 2018.

[76]: Du, H., Sun, X., Hu, Y., Dong, X. and Zhou, J.,. High sensitive refractive index sensor based on cladding etched photonic crystal fiber Mach-Zehnder interferometer. Photonic Sensors, 9(2), pp.126-134, 2019.

[77]: Yang, W., Zhang, S., Geng, T., Li, L., Li, G., Gong, Y., Zhang, K., Tong, C., Lu, C., Sun, W. and Yuan, L.,. High Sensitivity Refractometer Based on a Tapered-Single Mode-No Core-Single Mode Fiber Structure. Sensors, 19(7), p.1722, 2019.

[78]: Li, T., Zhu, L., Yang, X., Lou, X. and Yu, L.,. A Refractive Index Sensor Based on H-Shaped Photonic Crystal Fibers Coated with Ag-Graphene Layers. Sensors, 20(3), p.741, 2020.

[79]: Noor, S.F.S.M., Harun, S.W., Ahmad, H. and Muhammad, A.R.,, January. Multimode interference based fiber-optic sensor for temperature measurement. In Journal of Physics: Conference Series (Vol. 1151, No. 1, p. 012023). IOP Publishing, 2019.

[80]: Teng, C., Deng, H., Liu, H., Yang, H., Yuan, L., Zheng, J. and Deng, S., , June. Refractive index sensor based on twisted tapered plastic optical fibers. In Photonics (Vol. 6, No. 2, p. 40). Multidisciplinary Digital Publishing Institute, 2019.

[81]: Li, Y., Liu, Z., & Jian, S. (2014). Multimode interference refractive index sensor based on coreless fiber. Photonic Sensors, 4(1), 21-27.

[82]: Shao, M., Qiao, X., Fu, H., Li, H., Jia, Z., & Zhou, H. (2014). Refractive index sensing of SMS fiber structure based Mach-Zehnder interferometer. *IEEE Photonics Technology Letters*, *26*(5), 437-439.

Appendix

(A)

COVEGA
TQE
10335 Guilford Road, Jessup, MD 20794, USA
Phone: +1 877.226.8342 **Fax**: +1 240.456.7200
Email: sales@covega.com **Web**: http://www.covega.com

BOA 1004: C-band Booster Optical Amplifier

7.1.2.SP.1004 Rev D

Description

The BOA 1004 is a high saturation output power high bandwidth polarization maintaining Booster Optical Amplifier (BOA). It incorporates a highly efficient InP/InGaAsP Quantum Well (QW) layer structure and a reliable ridge waveguide design.

It is housed in a standard 14 pin butterfly package with integrated thermoelectric cooler and thermistor. Packaging options include isolator(s) and choice of single mode fiber and polarization maintaining fiber tails.

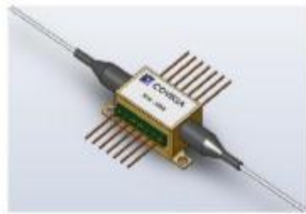

Applications

- ✓ Telecom & Datacom
- ✓ Booster Amplifier of Fixed and Tunable ITU Lasers and Transmitters
- ✓ Research & Non-Linear Applications

Features

- → High Saturation Output Power
- → Broad Spectral Bandwidth
- → High Fiber-to-Fiber Gain
- → High Polarization Extinction Ratio

Specifications

CW; T (Chip) = 25°C, T (Case) = 0 - 70°C

Parameter		Min	Typ	Max	
Operating Current	I_{OP}		600	750	mA
Central Wavelength	λ_C	1530	1550	1570	nm
Optical 3 dB Bandwidth	BW	90	100		nm
Saturation Output Power @ -3 dB	P_{SAT}	13	15		dBm
Small Signal Peak Gain @ Pin = -20 dBm	G	25	28		dB
Gain Ripple (rms) @ I_{OP}	δG		0.1	0.2	dB
Noise Figure	NF		7	9	dB
Forward Voltage	V_F		1.4	1.6	V
TEC Operation (typ / max @ T_{CASE} = 25°C / 70°C)					
- TEC Current	I_{TEC}		0.12	1.5	A
- TEC Voltage	V_{TEC}		0.25	4	V
- Thermistor Resistance	R_{TH}		10K		Ω
SPECIFICATIONS SUBJECTED TO CHANGE WITHOUT NOTICE					

COVEGA

TQE
10335 Guilford Road, Jessup, MD 20794, USA
Phone: +1 877.226.8342 **Fax**: +1 240.456.7200
Email: sales@covega.com **Web**: http://www.covega.com

BOA 1004

Performance

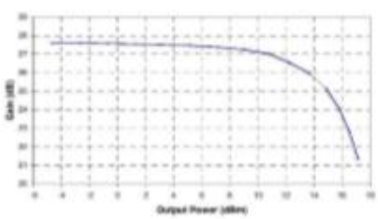

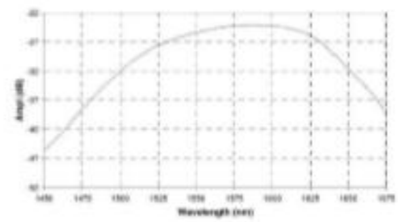

Packaging

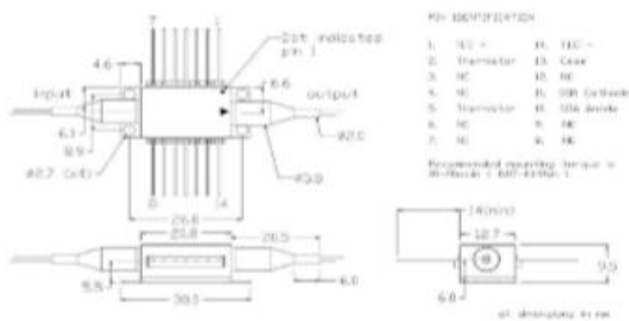

Ordering Information

BOA 1004 - X - 0 - X - X - X - X - X

X	0	X	X	X	X	X	Numeric
Isolator	**Reserved**	**Fiber jacket configuration***	**Input Fiber**	**Output Fiber**	**Input Connecter**	**Output Connector**	**Grade Level**
0 = none		T = SMF-28, tight jacket	S = SMF	S = SMF	A = FC/APC	A = FC/APC	0 / blank = Std.
1 = input only		V = PMF 1550 nm, loose tube	P = PMF	P = PMF			1 = XL
2 = output only							2 = Reserved
3 = input & output							

Custom orders with isolators require a minimum purchase quantity.

* see all of the fibertail options in the Covega catalog

Appendix (B)

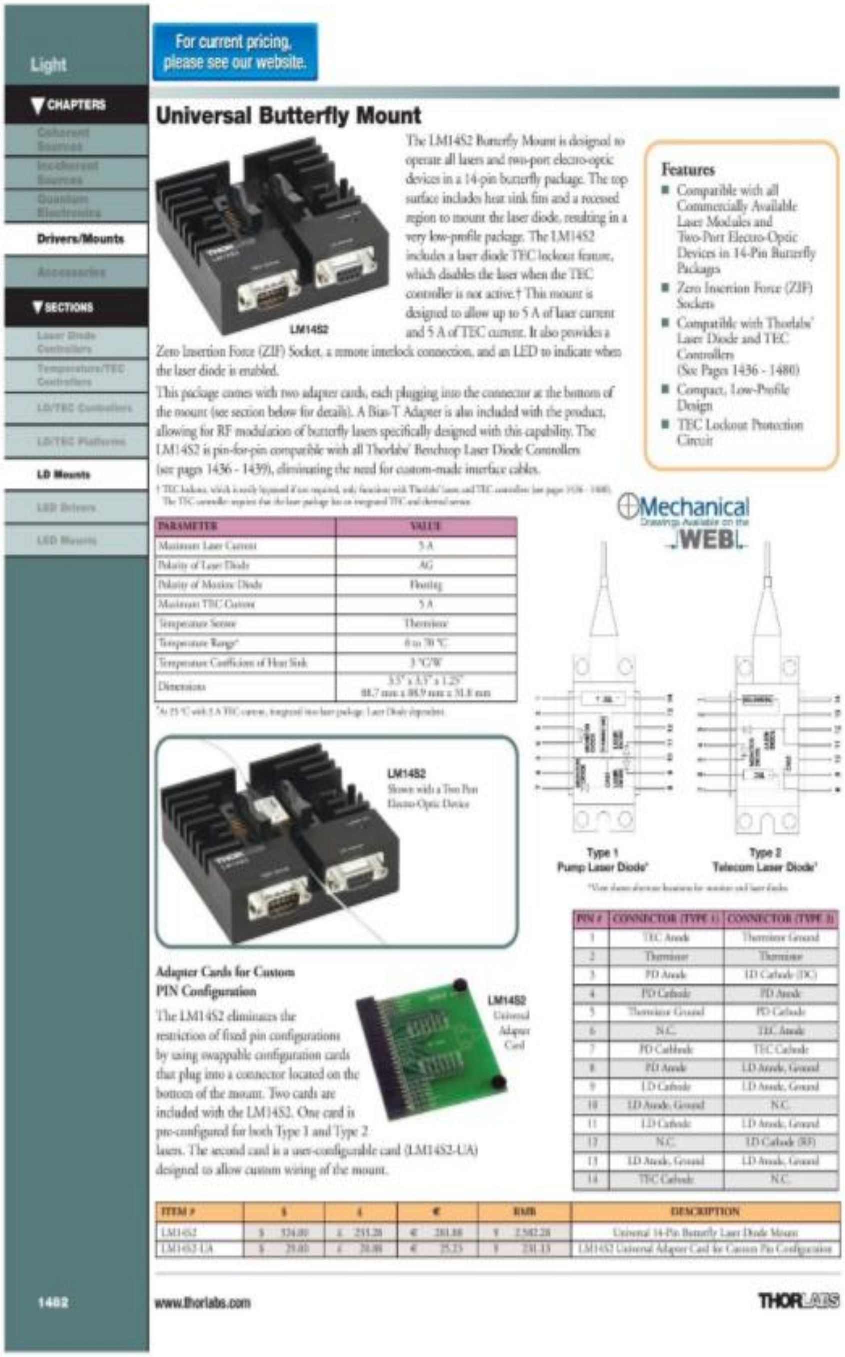

Light

CHAPTERS

Coherent Sources

Incoherent Sources

Quantum Electronics

Drivers/Mounts

Accessories

SECTIONS

Laser Diode Controllers

Temperature/TEC Controllers

LD/TEC Controllers

LD/TEC Platforms

LD Mounts

LED Drivers

LED Mounts

For current pricing, please see our website.

Universal Butterfly Mount

LM14S2

The LM14S2 Butterfly Mount is designed to operate all lasers and two-port electro-optic devices in a 14-pin butterfly package. The top surface includes heat sink fins and a recessed region to mount the laser diode, resulting in a very low-profile package. The LM14S2 includes a laser diode TEC lockout feature, which disables the laser when the TEC controller is not active.† This mount is designed to allow up to 5 A of laser current and 5 A of TEC current. It also provides a Zero Insertion Force (ZIF) Socket, a remote interlock connection, and an LED to indicate when the laser diode is enabled.

This package comes with two adapter cards, each plugging into the connector at the bottom of the mount (see section below for details). A Bias-T Adapter is also included with the product, allowing for RF modulation of butterfly lasers specifically designed with this capability. The LM14S2 is pin-for-pin compatible with all Thorlabs' Benchtop Laser Diode Controllers (see pages 1436 - 1439), eliminating the need for custom-made interface cables.

† TEC lockout, which is easily bypassed if not required, only functions with Thorlabs' lasers and TEC controllers (see page 1436 - 1480). The TEC controller requires that the laser package has an integrated TEC and thermal sensor.

Features

- Compatible with all Commercially Available Laser Modules and Two-Port Electro-Optic Devices in 14-Pin Butterfly Packages
- Zero Insertion Force (ZIF) Sockets
- Compatible with Thorlabs' Laser Diode and TEC Controllers (See Pages 1436 - 1480)
- Compact, Low-Profile Design
- TEC Lockout Protection Circuit

PARAMETER	VALUE
Maximum Laser Current	5 A
Polarity of Laser Diode	AG
Polarity of Monitor Diode	Floating
Maximum TEC Current	5 A
Temperature Sensor	Thermistor
Temperature Range*	0 to 70 °C
Temperature Coefficient of Heat Sink	3 °C/W
Dimensions	3.5" x 3.5" x 1.25" 88.7 mm x 88.9 mm x 31.8 mm

*At 25 °C with 5 A TEC current, integrated into laser package. Laser Diode dependent.

Mechanical Drawings Available on the WEB

Type 1 Pump Laser Diode*

Type 2 Telecom Laser Diode*

*View shows electrical locations for monitor and laser diodes.

LM14S2

Shown with a Two Port Electro-Optic Device

PIN #	CONNECTOR (TYPE 1)	CONNECTOR (TYPE 2)
1	TEC Anode	Thermistor Ground
2	Thermistor	Thermistor
3	PD Anode	LD Cathode (DC)
4	PD Cathode	PD Anode
5	Thermistor Ground	PD Cathode
6	N.C.	TEC Anode
7	PD Cathode	TEC Cathode
8	PD Anode	LD Anode, Ground
9	LD Cathode	LD Anode, Ground
10	LD Anode, Ground	N.C.
11	LD Cathode	LD Anode, Ground
12	N.C.	LD Cathode (RF)
13	LD Anode, Ground	LD Anode, Ground
14	TEC Cathode	N.C.

Adapter Cards for Custom PIN Configuration

LM14S2 Universal Adapter Card

The LM14S2 eliminates the restriction of fixed pin configurations by using swappable configuration cards that plug into a connector located on the bottom of the mount. Two cards are included with the LM14S2. One card is pre-configured for both Type 1 and Type 2 lasers. The second card is a user-configurable card (LM14S2-UA) designed to allow custom wiring of the mount.

ITEM #	\$	£	€	RMB	DESCRIPTION
LM14S2	\$ 324.00	£ 233.28	€ 281.88	¥ 2,582.28	Universal 14-Pin Butterfly Laser Diode Mount
LM14S2-UA	\$ 29.00	£ 20.88	€ 25.23	¥ 231.13	LM14S2 Universal Adapter Card for Custom Pin Configuration

1482

www.thorlabs.com

THORLABS

Appendix (C)

THORLABS

Laser Diode Controller

LDC200C Series Operation Manual

2014

General Information

The Thorlabs LDC200C Series Laser Diode Controllers are high accuracy precise injection current controllers for laser diodes and LEDs. Together with a Thorlabs Temperature Controller a stable operation of the connected laser diode can be achieved. The LDC200C Series includes the following types:

- LDC200CV - designed for safe operation of VCSEL laser diodes.
- LDC201CU - ultra low noise current (<0.2μA RMS).
- LDC202C, LDC205C and LDC210C - enhanced compliance voltage (>10V) for use with blue laser diodes.
- LDC240C - higher current (4A).

The LDC200C Series controllers are easy to operate via the operating elements on the front panel. Operating parameters are shown on a 5-digit LED display. UP-DOWN keys allow to select the parameter to be displayed.

After switching on a LDC200C Series laser diode controller, it remains in LASER OFF mode. The laser current can be switched on/off using the appropriate key at the front panel.

Additionally the laser current can be switched by applying a TTL signal to the LD remote input at the rear of the unit.

The laser and the photodiode are connected via a 9-pin D-SUB jack at the rear of the unit. The output for the laser diode and the input for the photodiode are bipolar, thus all polarities of commercial available laser diodes can be connected.

The injection current or the optical output power of the laser diode can be modulated applying a modulation signal to the input at the rear of the unit.

A voltage proportional to the laser diode current is provided for monitoring purposes at an analog control output at the rear.

If an error occurs or the limit for the laser current is reached, the corresponding LED lights up and a short beep gives a warning.

For a low ripple and noise of the output current a mains filter is installed and the transformer is shielded carefully.

The LDC200C Series controller are cooled by an internal fan, which protects the unit against overheating in case of high environmental temperatures. With free air circulation a safe operation of the unit is guaranteed up to 40 °C ambient temperature.

Warning

Do not obstruct the air ventilation slots in the housing!

Note

In order to prevent damages to the laser diode, it is recommended to mount the laser into a suitable Thorlabs laser diode mount and connect it to the LDC200C Series using the supplied Thorlabs CAB400 cable. This ensures the utmost protection of the laser diode from damage by wrong connection.

Appendix (D)

THORLABS

Thermoelectric Temperature Controller

TED200C
Operation Manual

2011

General Information

The thermoelectric Temperature Controller TED200C by Thorlabs is an extremely precise temperature controller for laser diodes and detectors.

The TED200C is excellently suited for:

- **wavelength stabilization of laser diodes**
- **noise reduction of detectors**
- **wavelength tuning by regulating the temperature**
- **modulation of wavelength by tuning the temperature**

The unit is easy to use due to the clearly arranged operating elements on the front panel. The operating parameters are shown by a 5-digit LED display, the measurement value shown is selected via keys.

The gain (P-share), the integral share and the derivative share of the PID temperature control loop can be set independent of each other.

Different temperature sensors can be used with the temperature controller TED200C, thermistors, or temperature IC sensors: AD590, AD592, LM135, LM 335. With a thermistor the temperature display is shown as resistance value in kΩ, if the TED200C is operated with a temperature sensor IC the temperature is shown in °C.

The output for the TEC current can be switched on or off via key from the front panel.

The temperature sensor and the TEC element are connected by a 15-pin D-sub jack at the rear of the unit.

At the output jack a control signal is available to drive an external LED to indicate TEC ON mode when the TEC current loop is activated.

The set value of the temperature can be changed with a knob at the front panel or via an analog input at the rear of the unit.

An analog voltage proportional to the actual value of the temperature is available at the rear of the unit for monitoring purposes.

The unit has been designed for safe operation with environmental temperatures of more than 40 °C provided that a free air circulation through the ventilation slots at the rear and at both sides of the unit is maintained.

Attention

Do not obstruct the air-ventilation slots in the housing!

In case of overheating caused by too high environmental temperatures or closed ventilation slots the unit automatically switches the output off to avoid damages.

The LED "OTP" (over-temperature-protection) indicates the over-temperature.

After temperature drop of about 10 °C the LED "OTP" extinguishes and the output current can be switched on again by pressing the key "ON".

If an error occurs (OTP or OPEN) the corresponding LED lights up and a beeper gives a short warning signal.

Appendix
(E)

Corning® SMF-28® Ultra Optical Fiber

Product Information

CORNING

Corning® SMF-28® Ultra optical fiber is an ITU-T Recommendation G.652.D compliant optical fiber with Corning's enhanced low-loss and bend fiber technologies. This full-spectrum fiber has bend performance that exceeds the ITU-T Recommendation G.657.A1 standard and still splices the same as the installed base of standard single-mode fibers such as SMF-28e+ fiber. SMF-28 Ultra fiber offers industry-leading specifications for attenuation, macrobend loss, and polarization mode dispersion values, which provide a solid foundation for new network deployments as well as upgrades to existing networks. Since Corning brought the first fiber to market more than 40 years ago, Corning's leadership in single-mode fiber innovation has been unparalleled.

Optical Specifications

Maximum Attenuation

Wavelength (nm)	Maximum Value* (dB/km)
1310	≤ 0.32
1383**	≤ 0.32
1490	≤ 0.21
1550	≤ 0.18
1625	≤ 0.20

* Alternate attenuation offerings available upon request.
** Attenuation values at this wavelength represent post-hydrogen aging performance.

Attenuation vs. Wavelength

Range (nm)	Ref. λ (nm)	Max. α Difference (dB/km)
1285 – 1330	1310	0.03
1525 – 1575	1550	0.02

The attenuation in a given wavelength range does not exceed the attenuation of the reference wavelength (λ) by more than the value α.

Macrobend Loss

Mandrel Radius (mm)	Number of Turns	Wavelength (nm)	Induced Attenuation* (dB)
10	1	1550	≤ 0.50
10	1	1625	≤ 1.5
15	10	1550	≤ 0.05
15	10	1625	≤ 0.30
25	100	1310, 1550, 1625	≤ 0.01

*The induced attenuation due to fiber wrapped around a mandrel of a specified radius.

Point Discontinuity

Wavelength (nm)	Point Discontinuity (dB)
1310	≤ 0.05
1550	≤ 0.05

Cable Cutoff Wavelength (λ_{cc})

$\lambda_{cc} \le 1260$ nm

Mode-Field Diameter

Wavelength (nm)	MFD (μm)
1310	9.2 ± 0.4
1550	10.4 ± 0.5

Dispersion

Wavelength (nm)	Dispersion Value [ps/(nm·km)]
1550	≤ 18.0
1625	≤ 22.0

Zero Dispersion Wavelength (λ_0): 1304 nm $\le \lambda_0 \le$ 1324 nm
Zero Dispersion Slope (S_0): $S_0 \le 0.092$ ps/(nm^2·km)

Polarization Mode Dispersion (PMD)

	Value (ps/√km)
PMD Link Design Value	≤ 0.04*
Maximum Individual Fiber PMD	≤ 0.1

*Complies with IEC 60794-3: 2001, Section 5.5, Method 1, (m = 20, Q = 0.01%), September 2001.

The PMD link design value is a term used to describe the PMD of concatenated lengths of fiber (also known as PMD_Q). This value represents a statistical upper limit for total link PMD. Individual PMD values may change when fiber is cabled.

How to Order

Contact your sales representative, or call the Optical Fiber Customer Service Department:
Ph: 1-607-248-2000 (U.S. and Canada)
+44-1244-525-320 (Europe)
Email: cofic@corning.com
Please specify the fiber type, attenuation, and quantity when ordering.

PI1424 | ISSUED: NOVEMBER 2014 SUPERSEDES: JULY 2014 | TL9000/ISO9001 CERTIFIED

Dimensional Specifications

Glass Geometry	
Fiber Curl	≥ 4.0 m radius of curvature
Cladding Diameter	125.0 ± 0.7 μm
Core-Clad Concentricity	≤ 0.5 μm
Cladding Non-Circularity	≤ 0.7%

Coating Geometry	
Coating Diameter	242 ± 5 μm
Coating-Cladding Concentricity	< 12 μm

Environmental Specifications

Environmental Test	Test Condition	Induced Attenuation 1310 nm, 1550 nm, and 1625 nm (dB/km)
Temperature Dependence	-60°C to +85°C*	≤ 0.05
Temperature Humidity Cycling	-10°C to +85°C up to 98% RH	≤ 0.05
Water Immersion	23°C ± 2°C	≤ 0.05
Heat Aging	85°C ± 2°C	≤ 0.05
Damp Heat	85°C at 85% RH	≤ 0.05

*Reference temperature = +23°C
Operating Temperature Range: -60°C to +85°C

Mechanical Specifications

Proof Test

The entire fiber length is subjected to a tensile stress ≥ 100 kpsi (0.69 GPa).*

*Higher proof test levels available.

Length

Fiber lengths available up to 63.0 km/spool.

Performance Characterizations

Characterized parameters are typical values.

Core Diameter	8.2 μm
Numerical Aperture	0.14 NA is measured at the one percent power level of a one-dimensional far-field scan at 1310 nm.
Effective Group Index of Refraction (N_{eff})	1310 nm: 1.4676 1550 nm: 1.4682
Fatigue Resistance Parameter (N_d)	20
Coating Strip Force	Dry: 0.6 lbs. (3N) Wet, 14-day room temperature: 0.6 lbs. (3N)
Rayleigh Backscatter Coefficient (for 1 ns Pulse Width)	1310 nm: -77 dB 1550 nm: -82 dB

CORNING

Corning Incorporated
One Riverfront Plaza
Corning, NY 14831 U.S.A.
Ph: 607-248-2000 (U.S. and Canada)
+44-1244-525-320 (Europe)
Email: cofic@corning.com
www.corning.com/opticalfiber

Appendix (F)

THORLABS

Coreless Termination Fiber

FG125LA
FG250LA
FG400LA

Description

These coreless silica termination fibers can be spliced to the ends of standard fiber to reduce back reflections or prevent damage to the fiber end face. A return loss of greater than 65 dB is achieved by splicing 0.25 m of coreless fiber to the desired component.

Specifications

Specifications			
Item #	FG125LA	FG250LA	FG400LA
Wavelength Range	400 - 2400 nm		
Return Loss	>65 dB with 0.25 m		
Glass Diameter	125 ± 1 µm	250 ± 10 µm	400 ± 15 µm
Coating Diameter	250 µm ± 5%	400 ± 20 µm	550 ± 20 µm
Coating	Acrylate		
Glass Refractive Index	1.467287 @ 436 nm 1.458965 @ 589.3 nm 1.450703 @1020 nm 1.444 @1550 nm		
Operating Temperature	-40 to 85 °C		
Proof Test Level	>100 kpsi		
Recommended Stripping Tool	T06S13 or FTS4	T12S16	T18S25

Appendix (G)

Specifications to arc fusion splicer (FSM-60S)

Item	Specifications
Applicable fibers	SMF ,MMF ,DSF ,NZDSF etc.
Cladding dia./sheathe dia.	80 to150 µm / 100 to 1000 µm
Splice mode	Total 100 modes
Automatic fiber identification	SMF ,MMF ,NZDSF
Splice loss estimate	Equipped
Attenuation splice	0.1 dB to 15dB by 0.1 dB step
Splice result storage	Last 2000 splices
Viewing methods	2 axis 2CMOS camera with 4.1 LCD
Tension test	1.96 to 2.25 N
Protection sleeve	60mm ,40mm and Fujikura micro sleeves
Diagnostic function	Equipped

الخلاصة

الألياف الضوئية تمتلك خصائص جوهرية عدة متمثلة بالحجم البسيط ومقاومة المجال الكهرومغناطيسي والمقاومة الجيدة للتأكل وكذلك تمتلك متانة ومرونة وما الى ذلك.

أجهزة الاستشعار شديدة الحساسية تعتمد بالكامل على هذه الالياف وتعتمد على ظاهرة التداخل متعدد الاوضاع وتأثير التصوير الذاتي في بنية الليف أحادي النمط _ ليف منزوع القلب _ ليف أحادي النمط وتم فحصها عمليا.

يتم فحص هذا المستشعر من خلال استخدام ليف منزوع القلب والذي يمثل منطقة قياس الحساسية بأقطار مختلفة للحصول على أفضل النتائج وفحص معامل الانكسار للسوائل المختلفة ومحلول الملح.

تمت دراسة مستشعر معامل الانكسار لثلاثة أطوال مختلفة (20, 25 و 30 مم) من الليف عديم القلب والذي يمثل منطقة الاستشعار. نظرا لأن قطر الليف عديم القلب يعد عاملا أساسيا في تكوين بنية الألياف للوصول الى الحساسية الشديدة، تم بحث تأثير قطر الليف عديم القلب لمقدار الحساسية في متحسس معامل الآنكسار. وفقا لذلك، تم تحضير أقطار مختلفة (100, 75 و 50 ميكرون) لكل طول. تم حفر قطر الليف عديم القلب كيميائياَ عن طريق غمره بمحلول حمض الهيدروفلوريك (40%). تبدأ عملية تكوين بنية المتحسس بأزالة طبقة الآكريليت من الليف الأحادي النمط والليف العديم القلب، وبعدها تم لحام قطعتين من الليف الآحادي النمط مع قطعة من الليف عديم القلب. وبعد ذلك تم وضع هذا التركيب في أخدود على شكل حرف V.

تم وضع محلول حمض الهيدروفلوريك في هذا الاخدود لاتمام عملية الحفر الكيميائي في أوقات مختلفة للحصول على أقطار مختلفة لليف عديم القلب وتم رؤية مناطق اللحام بعد عملية الحفر بواسطة جهاز المجهر الآلكتروني عالي الدقة للتأكد أنها لم تتأثر بالمحلول الكيميائي. تم الحصول على النتائج التجريبية لهذا العمل وأفضل النتائج لهذا المتحسس هي عندما كان قطر الليف عديم القلب 50 ميكرون وطوله 25 مم حيث أن أقصى حساسية تم الحصول عليها هي 1012 نانو متر \ وحدة معامل الانكسار بالنسبة لمحلول كلوريد الصوديوم عندما يكون التركيز 25% . بينما لمعامل الانكسار 1.352 للأسيتون تكون حساسية المستشعر 1058 نانو متر \ وحدة قياس معامل الانكسار.

تم حساب معامل التركيب الخطي للمتحسس ووجد أنه يساوي 0.998 لهذه النتائج مما يعرض ميزات تحسس مستشعر معامل الانكسار بهذا التكوين.

وزارة التعليم العالي والبحث العلمي

جامـــعة بغـــداد

معهد اللـــيزر للدراســـــات العليا

متحسس الليف لمعامل الأنكسار المعتمد على تداخل ماخ زندر لبنية الليف أحادي النمط - عديم القلب- أحادي النمط

رسالة مقدمة إلى

معهد الليزر للدراسات العليا /جامعة بغداد /لاستكمال متطلبات نيل شهادة ماجستير علوم في الليزر/ هندسة الكترونيك والاتصالات

من قبل

نور عدنان حمزة

بكالوريوس هندسة ليزر والكترونيات بصرية -2013

بأشراف

الأستاذ المساعد الدكتورة حنان جعفر طاهر

1441 هـ **2020 م**